SOLUTIONS OF NOVEL POTENTIAL-BASED FORMULATIONS USING THE
MULTILEVEL FAST MULTIPOLE ALGORITHM

A THESIS SUBMITTED TO
THE GRADUATE SCHOOL OF NATURAL AND APPLIED SCIENCES
OF
MIDDLE EAST TECHNICAL UNIVERSITY

BY

UĞUR MERİÇ GÜR

IN PARTIAL FULFILLMENT OF THE REQUIREMENTS
FOR
THE DEGREE OF MASTER OF SCIENCE
IN
ELECTRICAL AND ELECTRONICS ENGINEERING

FEBRUARY 2018

Approval of the thesis:

SOLUTIONS OF NOVEL POTENTIAL-BASED FORMULATIONS USING THE MULTILEVEL FAST MULTIPOLE ALGORITHM

submitted by **UĞUR MERİÇ GÜR** in partial fulfillment of the requirements for the degree of **Master of Science in Electrical and Electronics Engineering Department, Middle East Technical University** by,

Prof. Dr. Gülbin Dural Ünver
Dean, Graduate School of **Natural and Applied Sciences**   _____

Prof. Dr. Tolga Çiloğlu
Head of Department, **Electrical and Electronics Engineering**   _____

Assoc. Prof. Dr. Özgür Ergül
Supervisor, **Electrical and Electronics Eng. Dept., METU**   _____

Examining Committee Members:

Prof. Dr. Gülbin Dural Ünver
Electrical and Electronics Engineering Department, METU   _____

Assoc. Prof. Dr. Özgür Ergül
Electrical and Electronics Engineering Department, METU   _____

Prof. Dr. Özlem Aydın Çivi
Electrical and Electronics Engineering Department, METU   _____

Prof. Dr. Mustafa Kuzuoğlu
Electrical and Electronics Engineering Department, METU   _____

Prof. Dr. Vakur Behçet Ertürk
Elec. and Electronics Engineering Dept., Bilkent University   _____

Date: _____

I hereby declare that all information in this document has been obtained and presented in accordance with academic rules and ethical conduct. I also declare that, as required by these rules and conduct, I have fully cited and referenced all material and results that are not original to this work.

Name, Last Name: UĞUR MERİÇ GÜR

Signature   :

ABSTRACT

SOLUTIONS OF NOVEL POTENTIAL-BASED FORMULATIONS USING THE MULTILEVEL FAST MULTIPOLE ALGORITHM

Gür, Uğur Meriç

M.S., Department of Electrical and Electronics Engineering

Supervisor   : Assoc. Prof. Dr. Özgür Ergül

February 2018, 79 pages

In this thesis, recently introduced potential-based formulations that are based on direct usage of magnetic vector and electric scalar potentials, instead of the equivalent field-based formulations, are investigated. These new potential-based formulations can alleviate the well-known low-frequency breakdowns. Therefore, these formulations can be useful in providing the solution of a plethora of problems in future and emerging technologies that are difficult to analyze via standard solvers. The aim of this thesis is to combine potential formulations with special low-frequency implementations of the multilevel fast multiple algorithm (MLFMA) to tackle with finely discretized problems.

Thesis also includes the explanation of low-frequency breakdown mechanisms. In addition to the known breakdown of the electric-field integral equation, a hidden breakdown of the potential integral equations (PIEs) is shown. A remedy with the cost of an additional integral equation is proposed. All explanations for the low-frequency breakdown are supported with numerical results.

Among low-frequency stable implementations of MLFMA, two methods are implemented for PIEs. One of them is MLFMA based on multipoles without diagonalization. In this method, classical aggregation, translation, and disaggregation procedures in MLFMA are realized without plane-wave expansion. The other one is recently pro-

posed MLFMA implementation with approximate diagonalization. In this method, diagonalization is realized approximately with scaled spherical and plane waves. Accuracy and efficiency of the implementations are shown with numerical results.

ÖZ

YENİ POTANSİYEL-BAZLI FORMULASYONLARIN ÇOK SEVİYELİ HIZLI ÇOKKUTUP YÖNTEMİYLE ÇÖZÜMLERİ

Gür, Uğur Meriç

Yüksek Lisans, Elektrik ve Elektronik Mühendisliği Bölümü

Tez Yöneticisi   : Doç. Dr. Özgür Ergül

Şubat 2018, 79 sayfa

Bu tezde standart çözücülerde kullanılan alan-bazlı formülasyonlar yerine manyetik vektör ve elektrik skaler potansiyellerinin doğrudan kullanıldığı potansiyel-bazlı formülasyonlar incelenmiştir. Bu yeni potansiyel-bazlı formülasyonlar çok iyi bilinen düşük frekans bozulmalarını engellemektedir. Dolayısıyla, yeni potansiyel-bazlı formülasyonların, gelecek ve yeni teknolojilerde çözümleri gereken ancak standart çözücülerle ele alınamayan çeşitli problemlerin çözümlerine olanak sağlaması beklenmektedir. Bu tezin amacı da, yeni potansiyel bazlı formülasyonların, detaylı olarak ayrıklaştırılmış cisimlerin hassas çözümleri için çok seviyeli hızlı çokkutup yöntemiyle (MLFMA) birleştirilmesidir.

Tez kapsamında, düşük frekans bozulması mekanizmalarının tam açıklamaları da mevcuttur. Elektrik alan integral denkleminin bilinen düşük frekans bozulmasının yanı sıra, potansiyel integral denklemlerinin gizli kalmış bozulması da gösterilmiştir. Bu bozulmanın önlenmesi için ek bir integral denkleminin kullanıldığı bir çözüm geliştirilmiştir. Düşük frekans bozulmalarıyla ilgili tüm açıklamalar sayısal sonuçlarla desteklenmiştir.

Düşük frekans MLFMA uygulamaları arasından iki tanesi potansiyel integral denklemleri için programlanmıştır. Bunlardan ilki, köşegenleştirme yapmaksızın çokkutupların doğrudan kullanıldığı MLFMA uygulamasıdır. Bu metotta, MLFMA'da ger-

çekleştirilen toplama, öteleme ve dağıtma işlemleri düzlem dalga yaklaşımı olmaksızın gerçekleştirilmektedir. Diğeri ise, yakın zamanda önerilen, yaklaşık köşegenleştirmeli MLFMA uygulamasıdır. Bu yöntemde, köşegenleştirme işlemi ölçeklendirilmiş küresel ve düzlem dalgalarla yaklaşık olarak gerçekleştirilmektedir. Sayısal sonuçlarla, bu uygulamaların doğruluğu ve verimliliği gösterilmiştir.

Anahtar Kelimeler: Yüzey İntegral Denklemleri, Potansiyel Formülasyonları, Düşük-frekans Bozulması, Çok Seviyeli Hızlı Çokkutup Yöntemi

To my mother, my father, my sister and Kaju...

ACKNOWLEDGMENTS

TABLE OF CONTENTS

LIST OF TABLES

LIST OF FIGURES

FIGURES

LIST OF ABBREVIATIONS

AD   Approximate diagonalization

CFIE   Combined-field integral equation

EFIE   Electric-field integral equation

FMM   Fast multipole method

GMRES   Generalized minimal residual (method)

LF   Low frequency

MFIE   Magnetic-field integral equation

MoM   Method of moments

MLFMA   Multilevel fast multipole algorithm

PEC   Perfect electric conductor

PIE   Potential integral equation

RWG   Rao-Wilton-Glisson (function)

CHAPTER 1

INTRODUCTION

To understand the electromagnetic behavior of an object, it is very important to model and solve the corresponding electromagnetic problem [1]. When the problem involves non-canonical objects, one may need to solve the problem numerically. In order to design a system involving electromagnetic interactions, those numerical simulations become fundamental tools to avoid wasting material, time, money, and energy. Using a numerical simulation technique, designing a system becomes more efficient and less expensive.

In order to maximize the advantage of simulations, the proposed and used techniques should be accurate, fast and applicable in wide frequency bands. With standard integral equation techniques, such as the method of moments (MoM) [2], the applicability for large and/or detailed problems can be limited due to excessive time and memory requirements. Therefore, the fast multipole method (FMM) [3] and its multi-level version, namely, the multilevel fast multipole algorithm (MLFMA) [4], are introduced in the literature. With these algorithms, while the accuracy of MoM is preserved, the applicability can be increased enormously.

For the solution of electromagnetic problems in a computer environment, integral equations are transformed into matrix equations with the discretization of objects and numerical operators. To capture the electromagnetic variations accurately, as a rule of thumb, an object should be discretized with at least one-tenth of the wavelength when low-order discretizations are used. Therefore, as an object becomes larger, more discretization elements are needed, and thus, the corresponding matrix to be solved becomes larger. In order to solve a matrix equation, one of the fundamental problem

is to hold numbers, i.e., entries of the matrix, in memory. In MATLAB environment for example, holding a single complex variable requires 16 bytes, which means that an $N \times N$ matrix needs $16N^2$ bytes for storage. Therefore, in a standard computer, when the matrix size becomes a couple of tens of thousands, even storing the matrix itself in memory becomes an issue. This limits the solvable problem size, unless special techniques, such as FMM and MLFMA, are applied. Standard implementations of MLFMA are very efficient for high frequencies, i.e., when the object becomes electrically large.

While each method/equation have some domain, in which it works effective, researchers try to find methods/equations that can operate as general as possible with satisfactory accuracy and efficiency. Even though Maxwell's equations are valid everywhere (except when quantum mechanics or other effects come into play), there exists breakdowns and limitations, when they are discretized. In the context of integral equations, one of the most important limitation is the low-frequency breakdown. Standard formulations derived with field quantities lead to complete or partial failures when the frequency of operation becomes low or the wavelength becomes long. These issues are at the boundary between circuit physics and wave physics. As it is said in [5], "if one can transit smoothly from the world of wave physics to the world of the circuit physics, the richness in the world of circuit physics will be revealed. This is almost like the Alice in Wonderland story!" In order to unite these two different but intertwined physics in the context of surface integral equations, potential-based formulations are proposed, derived, and used.

In addition to stable formulations, fast, accurate, and efficient solution algorithms are also needed for objects involving fine details (low-frequency problems). However, when the size of the object becomes smaller than the wavelength, as the plane wave expansion fails, ordinary MLFMA fails too. In other words, MLFMA (and similar fast solvers) has its own low-frequency breakdown. For these problems, special MLFMA structures can be applied. In this thesis, multipole-based low-frequency MLFMA (LF-MLFMA) and MLFMA with approximate diagonalization (AD-MLFMA) are implemented for solving low frequency problems formulated with potential integral equations (PIEs).

2

In the rest of this chapter, derivations of field integral equations and their MoM solutions, as well as brief descriptions of MLFMA and iterative solvers are given.

1.1 Field Integral Equations

In this section, field integral equations for perfect electric conductors (PEC) are derived. For this purpose, Maxwell's equations can be written as

$$\nabla \times \boldsymbol{E}(\boldsymbol{r}, t) = -\frac{\partial \boldsymbol{B}(\boldsymbol{r}, t)}{\partial t} \tag{1.1}$$

$$\nabla \times \boldsymbol{H}(\boldsymbol{r}, t) = \boldsymbol{J}(\boldsymbol{r}, t) + \frac{\partial \boldsymbol{D}(\boldsymbol{r}, t)}{\partial t} \tag{1.2}$$

$$\nabla \cdot \boldsymbol{D}(\boldsymbol{r}, t) = \rho(\boldsymbol{r}, t) \tag{1.3}$$

$$\nabla \cdot \boldsymbol{B}(\boldsymbol{r}, t) = 0. \tag{1.4}$$

In the above, (1.1) is Faraday's law of induction, (1.2) is Ampere's law with the Maxwell's addition of time derivative of the electric flux density, (1.3) is Gauss' law, and finally, (1.4) represents the non-existence of magnetic charges. Combining (1.2) and (1.3) leads us to the continuity equation as

$$\nabla \cdot \boldsymbol{J}(\boldsymbol{r}, t) = -\frac{\partial \rho(\boldsymbol{r}, t)}{\partial t}. \tag{1.5}$$

Considering $e^{-i\omega t}$ time convention for time-harmonic waves, where ω is the angular frequency, (1.1), (1.2), and (1.5) reduce into

$$\nabla \times \boldsymbol{E}(\boldsymbol{r}) = i\omega \boldsymbol{B}(\boldsymbol{r}) \tag{1.6}$$

$$\nabla \times \boldsymbol{H}(\boldsymbol{r}) = \boldsymbol{J}(\boldsymbol{r}) - i\omega \boldsymbol{D}(\boldsymbol{r}) \tag{1.7}$$

$$\nabla \cdot \boldsymbol{J}(\boldsymbol{r}) = i\omega \rho(\boldsymbol{r}). \tag{1.8}$$

Assuming simple (linear, homogeneous, isotropic) medium, the main equations become

$$\nabla \times \boldsymbol{E}(\boldsymbol{r}) = i\omega \mu \boldsymbol{H}(\boldsymbol{r}) \tag{1.9}$$

$$\nabla \times \boldsymbol{H}(\boldsymbol{r}) = \boldsymbol{J}(\boldsymbol{r}) - i\omega \epsilon \boldsymbol{E}(\boldsymbol{r}) \tag{1.10}$$

$$\nabla \cdot \boldsymbol{E}(\boldsymbol{r}) = \rho(\boldsymbol{r})/\epsilon \tag{1.11}$$

$$\nabla \cdot \boldsymbol{H}(\boldsymbol{r}) = 0. \tag{1.12}$$

According to (1.4), the magnetic flux density $\boldsymbol{B}$ is a solenoidal vector field. Therefore, using the null identity, one can define

$$\nabla \times \boldsymbol{A}(\boldsymbol{r}) = \boldsymbol{B}(\boldsymbol{r}), \tag{1.13}$$

in which $\boldsymbol{A}(\boldsymbol{r})$ is the magnetic vector potential. Inserting (1.13) into (1.6), we obtain

$$\nabla \times (\boldsymbol{E}(\boldsymbol{r}) - i\omega\boldsymbol{A}(\boldsymbol{r})) = 0. \tag{1.14}$$

Therefore, $\boldsymbol{E}(\boldsymbol{r}) - i\omega\boldsymbol{A}(\boldsymbol{r})$ is an irrotational vector field, and it can be defined as the gradient of a scalar field in connected spaces $(-\nabla\phi(\boldsymbol{r}))$. Thus, we have

$$\boldsymbol{E}(\boldsymbol{r}) = i\omega\boldsymbol{A}(\boldsymbol{r}) - \nabla\phi(\boldsymbol{r}), \tag{1.15}$$

in which ϕ is the electric scalar potential.

For the wave equation, taking curl of both sides in (1.13), we obtain

$$\nabla \times \nabla \times \boldsymbol{A}(\boldsymbol{r}) = \mu\nabla \times \boldsymbol{H}(\boldsymbol{r}). \tag{1.16}$$

Then, using (1.10) and the vector identity $(\boldsymbol{A} \times \boldsymbol{B}) \times \boldsymbol{C} = \boldsymbol{B}(\boldsymbol{A} \cdot \boldsymbol{C}) - \boldsymbol{C}(\boldsymbol{A} \cdot \boldsymbol{B})$, we obtain

$$\nabla(\nabla \cdot \boldsymbol{A}(\boldsymbol{r})) - \nabla^2\boldsymbol{A}(\boldsymbol{r}) = \mu\boldsymbol{J}(\boldsymbol{r}) - i\omega\mu\epsilon\boldsymbol{E}(\boldsymbol{r}). \tag{1.17}$$

Using (1.15) and rearranging the terms, we reach

$$\nabla^2\boldsymbol{A}(\boldsymbol{r}) + k^2\boldsymbol{A}(\boldsymbol{r}) = -\mu\boldsymbol{J}(\boldsymbol{r}) + \nabla(\nabla \cdot \boldsymbol{A}(\boldsymbol{r}) - i\omega\mu\epsilon\phi(\boldsymbol{r})), \tag{1.18}$$

where $k = \omega\sqrt{\mu\epsilon}$ is the wavenumber. According to Helmholtz theorem, a vector field can only be specified when both irrotational and solenoidal components are defined. In (1.13), we define the curl of the magnetic vector potential. For its divergence,

$$\nabla \cdot \boldsymbol{A}(\boldsymbol{r}) = i\omega\mu\epsilon\phi(\boldsymbol{r}) \tag{1.19}$$

can be set, which is called Lorentz Gauge. Then, Helmholtz equation for the magnetic vector potential is found as

$$\nabla^2\boldsymbol{A}(\boldsymbol{r}) + k^2\boldsymbol{A}(\boldsymbol{r}) = -\mu\boldsymbol{J}(\boldsymbol{r}). \tag{1.20}$$

For the derivation of field quantities, solution of (1.20) is given further as (when the observation point is not on the source)

$$\boldsymbol{A}(\boldsymbol{r}) = \mu \int d\boldsymbol{r}' \boldsymbol{J}(\boldsymbol{r}') g(\boldsymbol{r}, \boldsymbol{r}'), \tag{1.21}$$

where

$$g(\boldsymbol{r}, \boldsymbol{r}') = \frac{e^{ikR}}{4\pi R} \tag{1.22}$$

is the free-space Green's function with $R = |\boldsymbol{r} - \boldsymbol{r}'|$. In the above, primed coordinate variables represent sources and unprimed coordinate variables represent observation points. Similarly, Helmholtz equation for the electric scalar potential and its solution for the derivation of field quantities (when the observation point is not on the source) can be written as

$$\nabla^2 \phi(\boldsymbol{r}) + k^2 \phi(\boldsymbol{r}) = -\frac{1}{\epsilon} \rho(\boldsymbol{r}) \tag{1.23}$$

$$\phi(\boldsymbol{r}) = \frac{1}{\epsilon} \int d\boldsymbol{r}' \rho(\boldsymbol{r}') g(\boldsymbol{r}, \boldsymbol{r}'). \tag{1.24}$$

Combining (1.15) with (1.21), (1.24), and (1.8) leads to

$$\boldsymbol{E}(\boldsymbol{r}) = i\omega\mu \int d\boldsymbol{r}' \boldsymbol{J}(\boldsymbol{r}') g(\boldsymbol{r}, \boldsymbol{r}') - \frac{1}{i\omega\epsilon} \int d\boldsymbol{r}' \nabla' \cdot \boldsymbol{J}(\boldsymbol{r}') \nabla g(\boldsymbol{r}, \boldsymbol{r}'). \tag{1.25}$$

Similarly, combining (1.13) and (1.21) gives

$$\boldsymbol{H}(\boldsymbol{r}) = \nabla \times \int d\boldsymbol{r}' g(\boldsymbol{r}, \boldsymbol{r}') \boldsymbol{J}(\boldsymbol{r}'). \tag{1.26}$$

Using the vector identity

$$\nabla \times [g(\boldsymbol{r}, \boldsymbol{r}') \boldsymbol{J}(\boldsymbol{r}')] = g(\boldsymbol{r}, \boldsymbol{r}') \nabla \times \boldsymbol{J}(\boldsymbol{r}') + \nabla g(\boldsymbol{r}, \boldsymbol{r}') \times \boldsymbol{J}(\boldsymbol{r}'),$$

and noting that the first term vanishes since surface current density uses primed coordinates, (1.26) can be written as

$$\boldsymbol{H}(\boldsymbol{r}) = \int d\boldsymbol{r}' \boldsymbol{J}(\boldsymbol{r}') \times \nabla' g(\boldsymbol{r}, \boldsymbol{r}'). \tag{1.27}$$

(1.25) and (1.27) can be written in operator notation as

$$\boldsymbol{E}(\boldsymbol{r}) = \eta \mathcal{T}\{\boldsymbol{J}\}(\boldsymbol{r}) \tag{1.28}$$

$$\boldsymbol{H}(\boldsymbol{r}) = \mathcal{K}\{\boldsymbol{J}\}(\boldsymbol{r}), \tag{1.29}$$

where $\eta = \sqrt{\mu/\epsilon}$ is the intrinsic impedance. Finally, using the boundary conditions for the continuity of the tangential component of the electric field intensity and the discontinuity of the tangential component of the magnetic field intensity, i.e.,

$$\hat{\boldsymbol{n}} \times \boldsymbol{E}(\boldsymbol{r}) = \hat{\boldsymbol{n}} \times [\boldsymbol{E}^{sec}(\boldsymbol{r}) + \boldsymbol{E}^{inc}(\boldsymbol{r})] = 0 \tag{1.30}$$

$$\hat{\boldsymbol{n}} \times \boldsymbol{H}(\boldsymbol{r}) = \hat{\boldsymbol{n}} \times [\boldsymbol{H}^{sec}(\boldsymbol{r}) + \boldsymbol{H}^{inc}(\boldsymbol{r})] = \boldsymbol{J}(\boldsymbol{r}), \tag{1.31}$$

we arrive at the electric-field integral equation (EFIE) and the magnetic-field integral equation (MFIE) for PEC objects as

$$-\hat{\boldsymbol{n}} \times \boldsymbol{E}^{inc}(\boldsymbol{r}) = \eta \hat{\boldsymbol{n}} \times \boldsymbol{\mathcal{T}}\{\boldsymbol{J}\}(\boldsymbol{r}) \tag{1.32}$$

$$-\hat{\boldsymbol{n}} \times \boldsymbol{H}^{inc}(\boldsymbol{r}) = -\boldsymbol{\mathcal{I}}\{\boldsymbol{J}\}(\boldsymbol{r}) + \hat{\boldsymbol{n}} \times \boldsymbol{\mathcal{K}}\{\boldsymbol{J}\}(\boldsymbol{r}), \tag{1.33}$$

where $\boldsymbol{\mathcal{I}}\{\boldsymbol{J}\}(\boldsymbol{r}) = \boldsymbol{J}(\boldsymbol{r})$ is the identity operator.

EFIE and MFIE suffer from an issue called internal resonance, which occurs due to non-zero null spaces of the corresponding impedance matrices. While the null-space solutions of MFIE have radiating nature, which can be seen in the far-zone scattered fields, null-space solutions of EFIE do not radiate. On the other hand, they can be visible with abrupt jumps in the conditioning of the impedance matrices. As the null spaces of EFIE and MFIE do not intersect, their linear combination is free of internal resonance and is called the combined-field integral equation (CFIE) [6].

1.2 Method of Moments

For the solution of electromagnetic problems involving arbitrarily shaped geometries, objects and operators can be discretized with the Rao-Wilton-Glisson (RWG) functions [7]. Figure 1.1, shows an RWG function spatially, and its mathematical definition is given as

$$\boldsymbol{b}_n^{\text{RWG}}(\boldsymbol{r}) = \begin{cases} \dfrac{l_n}{2A_{n1}}(\boldsymbol{r} - \boldsymbol{r}_{n1}), & \boldsymbol{r} \in S_{n1} \\ \dfrac{l_n}{2A_{n2}}(\boldsymbol{r}_{n2} - \boldsymbol{r}), & \boldsymbol{r} \in S_{n2} \\ \qquad\qquad 0, & \boldsymbol{r} \notin S_n, \end{cases} \tag{1.34}$$

where l_n represents the length of the main edge, and A_{n1} and A_{n2} are the areas of the first (S_{n1}) and the second (S_{n2}) triangles associated with the edge, respectively. Its
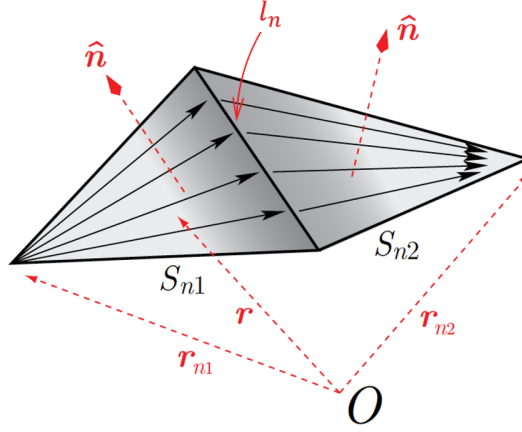
Figure 1.1: RWG functions are defined on pairs of triangles [8].

divergence is finite everywhere, i.e.,

$$
\nabla \cdot \boldsymbol{b}_n^{\text{RWG}}(\boldsymbol{r}) = \begin{cases} \dfrac{l_n}{A_{n1}}, & \boldsymbol{r} \in S_{n1} \\ -\dfrac{l_n}{A_{n2}}, & \boldsymbol{r} \in S_{n2} \\ \quad 0, & \boldsymbol{r} \notin S_n. \end{cases}
\tag{1.35}
$$

Using the RWG functions needs the triangulation of surfaces. A sample triangulation (discretization) of a cubic surface can be seen in Figure 1.2.

Expanding the unknown electric current density in (1.32) using the RWG functions, we obtain

$$
\boldsymbol{J}(\boldsymbol{r}) \approx \sum_{n=1}^{N} a_n \boldsymbol{b}_n^{\text{RWG}}(\boldsymbol{r})
\tag{1.36}
$$

$$
-\boldsymbol{E}^{inc}(\boldsymbol{r}) = \eta \sum_{n=1}^{N} a_n \mathcal{T}\{\boldsymbol{b}_n^{\text{RWG}}\}(\boldsymbol{r}).
\tag{1.37}
$$

In order to get N equations for N unknown coefficients, using a Galerkin approach, (1.37) is tested with the RWG functions as

$$
-\int_{S_m} d\boldsymbol{r}\, \boldsymbol{t}_m^{\text{RWG}}(\boldsymbol{r}) \cdot \boldsymbol{E}^{inc}(\boldsymbol{r}) = \eta \sum_{n=1}^{N} a_n \int_{S_m} d\boldsymbol{r}\, \boldsymbol{t}_m^{\text{RWG}}(\boldsymbol{r}) \cdot \mathcal{T}\{\boldsymbol{b}_n^{\text{RWG}}\}(\boldsymbol{r}).
\tag{1.38}
$$

7
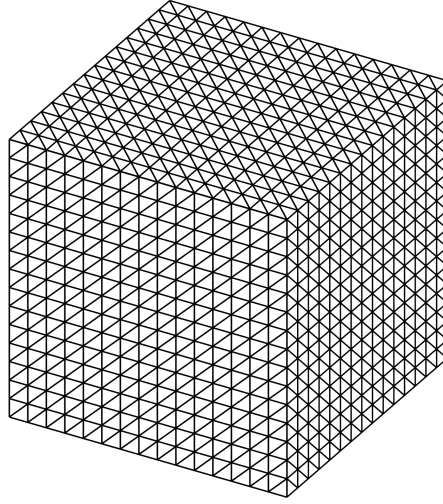
Figure 1.2: A cubic surface discretized with the RWG functions. For the discretization, 3600 RWG functions and 2700 triangles are used.

In this manner, a matrix equation $\bar{\boldsymbol{Z}} \cdot \boldsymbol{x} = \boldsymbol{y}$ is obtained, where

$$Z_{mn}^{\text{EFIE}} = \eta \int_{S_m} d\boldsymbol{r} \, \boldsymbol{t}_m^{\text{RWG}}(\boldsymbol{r}) \cdot \boldsymbol{\mathcal{T}}\{\boldsymbol{b}_n^{\text{RWG}}\}(\boldsymbol{r}) \tag{1.39}$$

$$x_n^{\text{EFIE}} = a_n \tag{1.40}$$

$$y_m^{\text{EFIE}} = -\int_{S_m} d\boldsymbol{r} \, \boldsymbol{t}_m^{\text{RWG}}(\boldsymbol{r}) \cdot \boldsymbol{E}^{inc}(\boldsymbol{r}) \tag{1.41}$$

for EFIE. Similarly, for MFIE, we have

$$Z_{mn}^{\text{MFIE}} = \int_{S_m} d\boldsymbol{r} \, \boldsymbol{t}_m^{\text{RWG}}(\boldsymbol{r}) \cdot [-\boldsymbol{\mathcal{I}}\{\boldsymbol{b}_n^{\text{RWG}}\}(\boldsymbol{r}) + \hat{\boldsymbol{n}} \times \mathcal{K}\{\boldsymbol{b}_n^{\text{RWG}}\}(\boldsymbol{r})] \tag{1.42}$$

$$x_n^{\text{MFIE}} = a_n \tag{1.43}$$

$$y_m^{\text{MFIE}} = -\int_{S_m} d\boldsymbol{r} \, \boldsymbol{t}_m^{\text{RWG}}(\boldsymbol{r}) \cdot \hat{\boldsymbol{n}} \times \boldsymbol{H}^{inc}(\boldsymbol{r}). \tag{1.44}$$

Integrals on the triangular domains can be calculated numerically using Gaussian quadratures [9], except when the observation and source points are close to each other where the singularity of the Green's function dominates. For this reason, singularity extraction methods can be used, where the singular integrals are calculated analytically [10].

8

1.3   Multilevel Fast Multipole Algorithm

In order to capture the electromagnetic behavior of an object using low-order discretizations, the discretization should be at least one-tenth of the wavelength. When the object becomes electrically large or it has small details that require very fine discretization elements, the classical MoM and the related solution of the matrix equation require a lot of computer memory. Although, supercomputers may handle such large problems, time requirements also make direct solutions infeasible. To deal with large problem in terms of the number of unknowns, FMM [3], and its multilevel extension, MLFMA [4], are introduced in the literature.

In MoM, all interactions between discretization functions are calculated and stored in memory. However, in MLFMA, by categorizing interactions according to distances between discretization elements (see (1.45)) as near-field and far-field interactions (e.g., using one-box-buffer scheme [8]), only the near-field interactions are stored while the far-field interactions are generated during matrix-vector multiplications on-the-fly. Those far-interactions are calculated in a group-by-group manner, reducing the complexity to $\mathcal{O}(N\log N)$ [1] from $\mathcal{O}(N^2)$. This categorization can be shown as matrix-vector multiplications as

$$\bar{\boldsymbol{Z}} \cdot \boldsymbol{x} = [\bar{\boldsymbol{Z}}^{\text{far}} + \bar{\boldsymbol{Z}}^{\text{near}}] \cdot \boldsymbol{x} = \boldsymbol{y}, \tag{1.45}$$

where $\bar{\boldsymbol{Z}}^{\text{far}}$ and $\bar{\boldsymbol{Z}}^{\text{near}}$ represent matrices that include far-field and near-field interactions, respectively.

In MLFMA, the geometry is fit in a cubic box, and the box is divided into subboxes, as shown in Figure 1.3 for a spherical body. Using recursive clustering, a tree structure is constructed. The interactions between basis and test functions can be calculated as follows: All radiated fields from basis functions inside each lowest level (smallest) box are shifted to the center of that box and summed. If multilevel, radiated fields are shifted to higher-level box centers and summed. Then, the radiated field at the center of each box is translated into incoming fields at the centers of far-zone boxes at the same level. If multilevel, incoming fields are shifted to box centers at the lower levels, and finally shifted on to testing functions at the lowest level.

In other words, there are three main stages in MLFMA: Shift the radiated fields of
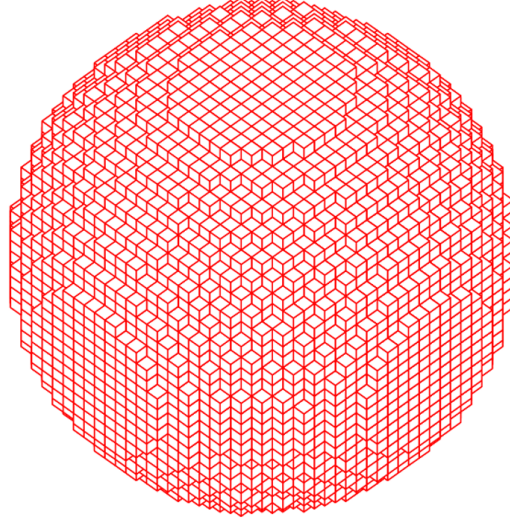
Figure 1.3: A clustering of a spherical body. Empty boxes are directly omitted in MLFMA interactions.

basis functions to box centers, and if multilevel, from lower-level boxes to their parents (aggregation); translate radiated fields to incoming fields (translation); and shift incoming fields (from higher-level boxes to their children, if multilevel) from box centers on to testing functions (disaggregation).

Mathematically, MLFMA is based on a factorization, namely, Gegenbauer's addition theorem, which can be written as

$$g(\boldsymbol{r}_i, \boldsymbol{r}_j) = \frac{ik}{4\pi} \sum_{t''=0}^{\infty} (-1)^{t''} (2t''+1) j_{t''}(kr_{iIJj}) h_{t''}^{(1)}(kr_{IJ}) P_{t''}(\hat{\boldsymbol{r}}_{IJ} \cdot \hat{\boldsymbol{r}}_{iIJj}), \quad (1.46)$$

where $j_{t''}$ is the spherical Bessel function of the first kind, $h_{t''}^{(1)}$ is the spherical Hankel function of the first kind, and $P_{t''}$ is the Legendre polynomial. The coordinate points are defined as follows: $\boldsymbol{r}_j$ is the source point (on basis function), $\boldsymbol{r}_J$ is the point where we aggregate (box center), $\boldsymbol{r}_I$ is the location to translate (box center), and $\boldsymbol{r}_i$ is the observation point (on testing function). Hence, in the above, we have

$$\boldsymbol{r}_{iI} = \boldsymbol{r}_i - \boldsymbol{r}_I$$

$$\boldsymbol{r}_{IJ} = \boldsymbol{r}_I - \boldsymbol{r}_J = r_{IJ}\hat{\boldsymbol{r}}_{IJ}$$

$$\boldsymbol{r}_{Jj} = \boldsymbol{r}_J - \boldsymbol{r}_j$$

10

$$\boldsymbol{r}_{iIJj} = \boldsymbol{r}_{iI} + \boldsymbol{r}_{Jj} = r_{iIJj}\hat{\boldsymbol{r}}_{iIJj}.$$

With plane-wave expansion of spherical functions, i.e.,

$$j_{t''}(k\boldsymbol{r}) = \frac{(-i)^{t''}}{4\pi} \int d^2\hat{\boldsymbol{k}} e^{i\boldsymbol{k}\cdot\boldsymbol{r}} P_{t''}(\hat{\boldsymbol{k}} \cdot \hat{\boldsymbol{r}}), \qquad (1.47)$$

where $\boldsymbol{r} = \hat{\boldsymbol{r}}r$, aggregation/disaggragation/translation stages are diagonalized as

$$g(\boldsymbol{r}_i, \boldsymbol{r}_j) = \frac{ik}{(4\pi)^2} \int d^2\hat{\boldsymbol{k}} \beta(\boldsymbol{k}, \boldsymbol{r}_{iIJj})\alpha(\boldsymbol{k}, \boldsymbol{r}_{IJ}), \qquad (1.48)$$

where

$$\beta(\boldsymbol{k}, \boldsymbol{r}) = \sum_{t=0}^{\infty} i^t(2t + 1)j_t(kr)P_{t''}(\hat{\boldsymbol{k}} \cdot \hat{\boldsymbol{r}}) = e^{i\boldsymbol{k}\cdot\boldsymbol{r}} \qquad (1.49)$$

$$\alpha(\boldsymbol{k}, \boldsymbol{r}) = \sum_{t=0}^{\infty} i^t(2t + 1)h_t^{(1)}(kr)P_{t''}(\hat{\boldsymbol{k}} \cdot \hat{\boldsymbol{r}}). \qquad (1.50)$$

Note that, in (1.49), expression is simplified to complex exponentials using spherical wave expansion. In (1.50), the infinite summation should be truncated for practical applications.

1.4 Iterative Solutions

Discretized integral equations can be solved efficiently via iterative techniques. Non-stationary iterative methods that are based on Cayley-Hamilton theorem and Krylov subspace are more efficient than stationary methods based on matrix splitting. Among non-stationary methods, generalized minimal residual (GMRES) method [11] is mostly used in the electromagnetics community due to its high efficiency and convergence performance. GMRES method is used in the results of this thesis, too.

At each iteration, vector generated by the iterative solver is directly used by MLFMA for a matrix-vector multiplication and the resulting vector is given back to the iterative solver to generate new vectors.

1.5 Post Proccessing

Solution of a linear system (matrix equation) gives coefficients for the unknown function that is the current density in standard formulations. Radiating the current density,

far-zone and near-zone electric and magnetic fields can further be found. As it is used in the derivation of the field formulations, near-zone scattered (secondary) fields can be found as

$$\boldsymbol{E}^{sec}(\boldsymbol{r}) = i\omega\mu \int d\boldsymbol{r}' \boldsymbol{J}(\boldsymbol{r}') g(\boldsymbol{r}, \boldsymbol{r}') - \frac{1}{i\omega\epsilon} \int d\boldsymbol{r}' \nabla' \cdot \boldsymbol{J}(\boldsymbol{r}') \nabla g(\boldsymbol{r}, \boldsymbol{r}') \qquad (1.51)$$

$$\boldsymbol{H}^{sec}(\boldsymbol{r}) = \int d\boldsymbol{r}' \boldsymbol{J}(\boldsymbol{r}') \times \nabla' g(\boldsymbol{r}, \boldsymbol{r}'). \qquad (1.52)$$

In the far-zone, these expressions become

$$\boldsymbol{E}^{sec}(\theta, \phi) \approx ik \frac{e^{ikr}}{4\pi r} \eta (\bar{\boldsymbol{I}}_{3\times 3} - \hat{\boldsymbol{r}}\hat{\boldsymbol{r}}) \cdot \int d\boldsymbol{r}' \boldsymbol{J}(\boldsymbol{r}') e^{-ik\hat{\boldsymbol{r}}\cdot\boldsymbol{r}'} \qquad (1.53)$$

$$\boldsymbol{H}^{sec}(\theta, \phi) \approx ik \frac{e^{ikr}}{4\pi r} \hat{\boldsymbol{r}} \times \int d\boldsymbol{r}' \boldsymbol{J}(\boldsymbol{r}') e^{-ik\hat{\boldsymbol{r}}\cdot\boldsymbol{r}'}, \qquad (1.54)$$

where $\bar{\boldsymbol{I}}_{3\times 3}$ is a unit dyad.

1.6 Motivation

The field integral equations derived in section 1.1 are based on fields. While these formulations are widely used and robust in many problems, they also suffer from numerical issues. For example, EFIE has a low-frequency breakdown, i.e., the formulation cannot capture the correct physical behavior as the frequency becomes low or the discretization becomes dense. In addition, MFIE fails for the solution of open-surface problems, such as waveguides, patch antennas, and microstrip circuits, where zero-thickness models are preferred.

Recently, PIEs are proposed for stable and accurate formulations of electromagnetic problems [12, 13]. These equations overcome the low-frequency breakdown, while they are also applicable to open surfaces. In this thesis, PIEs, which are based on magnetic vector and electric scalar potentials, are investigated. Advantages and drawbacks of PIEs are discussed. An accuracy analysis on PIEs and EFIE is given with a complete explanation of low-frequency breakdown. Accurate charge densities and near-zone electric fields obtained with EFIE at low frequencies are explained and introduced along with a hidden low-frequency breakdown of PIEs and its remedy. In addition, as the main purpose of this thesis, stable and fast solution techniques for PIEs are implemented. This way, PIEs are applied to challenging problems involving both dense discretizations and large numbers of unknowns.

The organization of the rest of the thesis is as follows:

Chapter 2 presents PIEs, including the derivation of the equations, discretization of PIEs, and how to use potentials as excitation. Results obtained with EFIE and PIEs are compared in terms of scattered fields and current densities for different excitations. Frequency-dependent accuracy characteristics are demonstrated.

In Chapter 3, a detailed discussion on how low-frequency breakdown occurs in EFIE and PIEs are given. In addition, a remedy for the hidden low-frequency breakdown of PIEs is proposed and used. As numerical results on canonical objects, surface current densities, far-zone scattered fields, electric charge densities, near-zone electric fields, magnetic fields and power densities are analyzed in detail with the explanations on their accuracy. Also, the accuracy of PIE-GSP (gradient of the scalar potential) is clearly demonstrated.

Chapter 4 presents low-frequency MLFMA methods used for PIEs. Two methods are considered; multipole-based MLFMA and AD-MLFMA. Starting from tests on Green's function, FMM and MLFMA (using multipoles and AD) results are shown. Accuracy and stability analysis are also presented.

Chapter 5 contains conclusions and future works.

CHAPTER 2

POTENTIAL INTEGRAL EQUATIONS

PIEs are new formulations [12, 13] that are based on potentials, as opposed to the conventional integral equations, namely EFIE and MFIE (or CFIE), that use fields. The first advantage of using potentials directly in the formulation is that the derived integral equations are resistant to low-frequency breakdowns. The second advantage is in quantum mechanics, i.e., the interaction created by the quantization of the electromagnetism is directly affected by the potentials, even when field quantities are zero [14]. This phenomenon is called Aharonov-Bohm effect. And the third advantage is, unlike MFIE, there is no assumption that limits the applicability of PIEs to open surfaces. That is, PIEs can be used for arbitrary geometries.

In this chapter, derivation and discretization of PIEs are given along with a scaling-based preconditioning technique. Real-life-applicable excitations created by using magnetic vector and electric scalar potentials are given. Finally, numerical results showing the accuracy of a MoM implementation for PIEs are presented.

2.1 Derivation of Potential Integral Equations

Combination of (1.10) and (1.16) lead to

$$\nabla \times \nabla \times \boldsymbol{A}(\boldsymbol{r}) = \mu \boldsymbol{J}(\boldsymbol{r}) - i\omega\mu\epsilon \boldsymbol{E}(\boldsymbol{r}). \tag{2.1}$$

Then, with (1.15), we obtain

$$\nabla \times \nabla \times \boldsymbol{A}(\boldsymbol{r}) = \mu \boldsymbol{J}(\boldsymbol{r}) + k^2 \boldsymbol{A}(\boldsymbol{r}) - i\omega\mu\epsilon\nabla\phi. \tag{2.2}$$

15

And using (1.19), we get

$$\nabla \times \nabla \times \boldsymbol{A}_1(\boldsymbol{r}) - \nabla(\nabla \cdot \boldsymbol{A}_1(\boldsymbol{r})) - k^2 \boldsymbol{A}_1(\boldsymbol{r}) = \mu \boldsymbol{J}(\boldsymbol{r}). \tag{2.3}$$

PIEs can be obtained by using dyadic Green's theorem for Region 1 in Figure 2.1 with (2.3) [10, 12], i.e.,
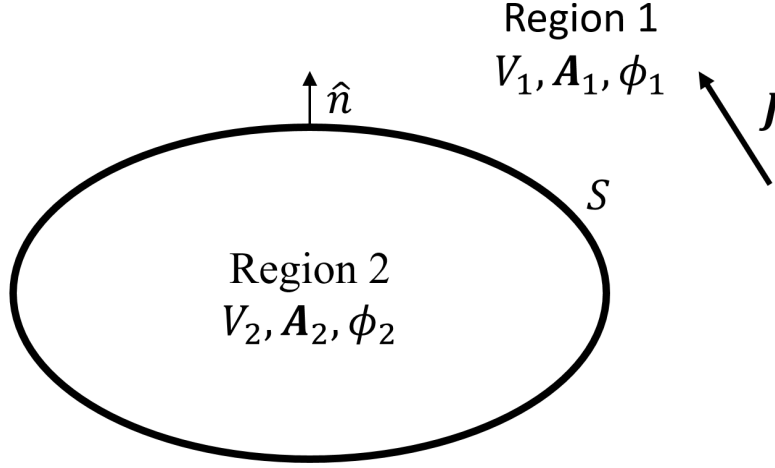
Figure 2.1: Configuration for the derivation of PIEs. Region 1 is bounded between surface S and infinity.

$$\nabla \times \nabla \times \boldsymbol{A}_1(\boldsymbol{r}) - \nabla(\nabla \cdot \boldsymbol{A}_1(\boldsymbol{r})) - k^2 \boldsymbol{A}_1(\boldsymbol{r}) = \mu \boldsymbol{J}(\boldsymbol{r}) \tag{2.4}$$

$$\nabla \times \nabla \times \bar{\boldsymbol{G}}_1(\boldsymbol{r}, \boldsymbol{r}') - \nabla(\nabla \cdot \bar{\boldsymbol{G}}_1(\boldsymbol{r}, \boldsymbol{r}')) - k^2 \bar{\boldsymbol{G}}_1(\boldsymbol{r}, \boldsymbol{r}') = \bar{\boldsymbol{I}}\delta(\boldsymbol{r} - \boldsymbol{r}'). \tag{2.5}$$

In (2.4), $\boldsymbol{A}_1(\boldsymbol{r})$ is the total magnetic vector potential for Region 1. In addition, replacing right-hand side with a Dirac-delta function (point source) leads to (2.5), in which $\bar{\boldsymbol{G}}_1(\boldsymbol{r}, \boldsymbol{r}')$ is the kernel function for Region 1.

Dot-multiplying the first equation with $\bar{\boldsymbol{G}}_1(\boldsymbol{r}, \boldsymbol{r}') \cdot \boldsymbol{a}$ from right and second equation with $\boldsymbol{A}_1(\boldsymbol{r})$ from left and with $\boldsymbol{a}$ from right, where $\boldsymbol{a}$ is an arbitrary vector, we obtain

$$\nabla \times \nabla \times \boldsymbol{A}_1(\boldsymbol{r}) \cdot \bar{\boldsymbol{G}}_1(\boldsymbol{r}, \boldsymbol{r}') \cdot \boldsymbol{a} - \nabla\nabla \cdot \boldsymbol{A}_1(\boldsymbol{r}) \cdot \bar{\boldsymbol{G}}_1(\boldsymbol{r}, \boldsymbol{r}') \cdot \boldsymbol{a}$$
$$- k^2 \boldsymbol{A}_1(\boldsymbol{r}) \cdot \bar{\boldsymbol{G}}_1(\boldsymbol{r}, \boldsymbol{r}') \cdot \boldsymbol{a} = \mu \boldsymbol{J}(\boldsymbol{r}) \cdot \bar{\boldsymbol{G}}_1(\boldsymbol{r}, \boldsymbol{r}') \cdot \boldsymbol{a} \tag{2.6}$$

$$\boldsymbol{A}_1(\boldsymbol{r}) \cdot \nabla \times \nabla \times \bar{\boldsymbol{G}}_1(\boldsymbol{r}, \boldsymbol{r}') \cdot \boldsymbol{a} - \boldsymbol{A}_1(\boldsymbol{r}) \cdot \nabla\nabla \cdot \bar{\boldsymbol{G}}_1(\boldsymbol{r}, \boldsymbol{r}') \cdot \boldsymbol{a}$$
$$- k^2 \boldsymbol{A}_1(\boldsymbol{r}) \cdot \bar{\boldsymbol{G}}_1(\boldsymbol{r}, \boldsymbol{r}') \cdot \boldsymbol{a} = \boldsymbol{A}_1(\boldsymbol{r}) \cdot \bar{\boldsymbol{I}} \cdot \boldsymbol{a}\delta(\boldsymbol{r} - \boldsymbol{r}'). \tag{2.7}$$

Subtracting (2.7) from (2.6) leads to

$$\nabla \times \nabla \times \boldsymbol{A}_1(\boldsymbol{r}) \cdot \bar{\boldsymbol{G}}_1(\boldsymbol{r}, \boldsymbol{r}') \cdot \boldsymbol{a} - \boldsymbol{A}_1(\boldsymbol{r}) \cdot \nabla \times \nabla \times \bar{\boldsymbol{G}}_1(\boldsymbol{r}, \boldsymbol{r}') \cdot \boldsymbol{a}$$
$$+ \boldsymbol{A}_1(\boldsymbol{r}) \cdot \nabla\nabla \cdot \bar{\boldsymbol{G}}_1(\boldsymbol{r}, \boldsymbol{r}') \cdot \boldsymbol{a} - \nabla\nabla \cdot \boldsymbol{A}_1(\boldsymbol{r}) \cdot \bar{\boldsymbol{G}}_1(\boldsymbol{r}, \boldsymbol{r}') \cdot \boldsymbol{a}$$
$$= \mu \boldsymbol{J}(\boldsymbol{r}) \cdot \bar{\boldsymbol{G}}_1(\boldsymbol{r}, \boldsymbol{r}') \cdot \boldsymbol{a} - \boldsymbol{A}_1(\boldsymbol{r}) \cdot \boldsymbol{a}\delta(\boldsymbol{r} - \boldsymbol{r}'). \tag{2.8}$$

To proceed, Green's vector identities are given as

$$\boldsymbol{P} \cdot (\nabla \times \nabla \times \boldsymbol{Q}) - \boldsymbol{Q} \cdot (\nabla \times \nabla \times \boldsymbol{P}) = \nabla \cdot (\boldsymbol{Q} \times \nabla \times \boldsymbol{P} - \boldsymbol{P} \times \nabla \times \boldsymbol{Q}) \tag{2.9}$$
$$\boldsymbol{P} \cdot \nabla(\nabla \cdot \boldsymbol{Q}) - \boldsymbol{Q} \cdot \nabla(\nabla \cdot \boldsymbol{P}) = \nabla \cdot (\boldsymbol{P}\nabla \cdot \boldsymbol{Q} - \boldsymbol{Q}\nabla \cdot \boldsymbol{P}) \tag{2.10}$$

for arbitrary vector fields $\boldsymbol{P}$ and $\boldsymbol{Q}$. Using these identities with $\boldsymbol{P} = \bar{\boldsymbol{G}}_1(\boldsymbol{r}, \boldsymbol{r}') \cdot \boldsymbol{a}$ and $\boldsymbol{Q} = \boldsymbol{A}_1(\boldsymbol{r})$, we reach

$$\nabla \times \nabla \times \boldsymbol{A}_1(\boldsymbol{r}) \cdot \bar{\boldsymbol{G}}_1(\boldsymbol{r}, \boldsymbol{r}') \cdot \boldsymbol{a} - \boldsymbol{A}_1(\boldsymbol{r}) \cdot \nabla \times \nabla \times \bar{\boldsymbol{G}}_1(\boldsymbol{r}, \boldsymbol{r}') \cdot \boldsymbol{a}$$
$$= \nabla \cdot \left[\nabla \times \boldsymbol{A}_1(\boldsymbol{r}) \times \bar{\boldsymbol{G}}_1(\boldsymbol{r}, \boldsymbol{r}') \cdot \boldsymbol{a} \right]$$
$$+ \nabla \cdot \left[(\boldsymbol{A}_1(\boldsymbol{r}) \times \nabla \times (\bar{\boldsymbol{G}}_1(\boldsymbol{r}, \boldsymbol{r}') \cdot \boldsymbol{a}) \right] \tag{2.11}$$
$$\boldsymbol{A}_1(\boldsymbol{r}) \cdot \nabla(\nabla \cdot \bar{\boldsymbol{G}}_1(\boldsymbol{r}, \boldsymbol{r}') \cdot \boldsymbol{a}) - \nabla\nabla \cdot \boldsymbol{A}_1(\boldsymbol{r}) \cdot \bar{\boldsymbol{G}}_1(\boldsymbol{r}, \boldsymbol{r}') \cdot \boldsymbol{a}$$
$$= \nabla \cdot \left[-\nabla \cdot \boldsymbol{A}_1(\boldsymbol{r})\bar{\boldsymbol{G}}_1(\boldsymbol{r}, \boldsymbol{r}') \cdot \boldsymbol{a} \right]$$
$$+ \nabla \cdot \left[\boldsymbol{A}_1(\boldsymbol{r})\nabla \cdot \bar{\boldsymbol{G}}_1(\boldsymbol{r}, \boldsymbol{r}') \cdot \boldsymbol{a} \right]. \tag{2.12}$$

Combination of (2.11) and (2.12) with (2.8), leads to

$$\mu \boldsymbol{J}(\boldsymbol{r}) \cdot \bar{\boldsymbol{G}}_1(\boldsymbol{r}, \boldsymbol{r}') \cdot \boldsymbol{a} - \boldsymbol{A}_1(\boldsymbol{r}) \cdot \boldsymbol{a}\delta(\boldsymbol{r} - \boldsymbol{r}') = \nabla \cdot \left[\nabla \times \boldsymbol{A}_1(\boldsymbol{r}) \times \bar{\boldsymbol{G}}_1(\boldsymbol{r}, \boldsymbol{r}') \cdot \boldsymbol{a} \right]$$
$$+ \nabla \cdot \left[(\boldsymbol{A}_1(\boldsymbol{r}) \times \nabla \times (\bar{\boldsymbol{G}}_1(\boldsymbol{r}, \boldsymbol{r}') \cdot \boldsymbol{a}) \right]$$
$$+ \nabla \cdot \left[-\nabla \cdot \boldsymbol{A}_1(\boldsymbol{r})\bar{\boldsymbol{G}}_1(\boldsymbol{r}, \boldsymbol{r}') \cdot \boldsymbol{a} \right]$$
$$+ \nabla \cdot \left[\boldsymbol{A}_1(\boldsymbol{r})\nabla \cdot \bar{\boldsymbol{G}}_1(\boldsymbol{r}, \boldsymbol{r}') \cdot \boldsymbol{a} \right]. \tag{2.13}$$

Then, taking volume integrals over V_1, using the divergence theorem, and noting the

17

radiation condition and direction of normal vector for Region 1, we have

$$
-\mu \int_{V_1} d\boldsymbol{r} \boldsymbol{J}(\boldsymbol{r}) \cdot \bar{\boldsymbol{G}}_1(\boldsymbol{r}, \boldsymbol{r}') \cdot \boldsymbol{a} + \int_{V_1} d\boldsymbol{r} \boldsymbol{A}_1(\boldsymbol{r}) \cdot \boldsymbol{a} \delta(\boldsymbol{r} - \boldsymbol{r}')
$$

$$
= \int_S d\boldsymbol{r} \hat{\boldsymbol{n}} \cdot \left[\nabla \times \boldsymbol{A}_1(\boldsymbol{r}) \times \bar{\boldsymbol{G}}_1(\boldsymbol{r}, \boldsymbol{r}') \cdot \boldsymbol{a} \right]
$$

$$
+ \int_S d\boldsymbol{r} \hat{\boldsymbol{n}} \cdot \left[\boldsymbol{A}_1(\boldsymbol{r}) \times \nabla \times \bar{\boldsymbol{G}}_1(\boldsymbol{r}, \boldsymbol{r}') \cdot \boldsymbol{a} \right]
$$

$$
+ \int_S d\boldsymbol{r} \hat{\boldsymbol{n}} \cdot \left[- \nabla \cdot \boldsymbol{A}_1(\boldsymbol{r}) \bar{\boldsymbol{G}}_1(\boldsymbol{r}, \boldsymbol{r}') \cdot \boldsymbol{a} \right]
$$

$$
+ \int_S d\boldsymbol{r} \hat{\boldsymbol{n}} \cdot \left[\boldsymbol{A}_1(\boldsymbol{r}) \nabla \cdot \bar{\boldsymbol{G}}_1(\boldsymbol{r}, \boldsymbol{r}') \cdot \boldsymbol{a} \right]. \qquad (2.14)
$$

Manipulating equations by using the identity $\boldsymbol{A} \cdot (\boldsymbol{B} \times \boldsymbol{C}) = (\boldsymbol{A} \times \boldsymbol{B}) \cdot \boldsymbol{C}$ leads to

$$
-\mu \int_{V_1} d\boldsymbol{r} \boldsymbol{J}(\boldsymbol{r}) \cdot \bar{\boldsymbol{G}}_1(\boldsymbol{r}, \boldsymbol{r}') \cdot \boldsymbol{a} + \boldsymbol{A}_1(\boldsymbol{r}') \cdot \boldsymbol{a} = \int_S d\boldsymbol{r} \hat{\boldsymbol{n}} \times (\nabla \times \boldsymbol{A}_1(\boldsymbol{r})) \cdot \bar{\boldsymbol{G}}_1(\boldsymbol{r}, \boldsymbol{r}') \cdot \boldsymbol{a}
$$

$$
+ \int_S d\boldsymbol{r} (\hat{\boldsymbol{n}} \times \boldsymbol{A}_1(\boldsymbol{r})) \cdot \nabla \times \bar{\boldsymbol{G}}_1(\boldsymbol{r}, \boldsymbol{r}') \cdot \boldsymbol{a}
$$

$$
- \int_S d\boldsymbol{r} \hat{\boldsymbol{n}} \cdot \left[\nabla \cdot \boldsymbol{A}_1(\boldsymbol{r}) \bar{\boldsymbol{G}}_1(\boldsymbol{r}, \boldsymbol{r}') \cdot \boldsymbol{a} \right]
$$

$$
+ \int_S d\boldsymbol{r} \hat{\boldsymbol{n}} \cdot \left[\boldsymbol{A}_1(\boldsymbol{r}) \nabla \cdot \bar{\boldsymbol{G}}_1(\boldsymbol{r}, \boldsymbol{r}') \cdot \boldsymbol{a} \right]. \qquad (2.15)
$$

We further note that

$$
\mu \int_{V_1} d\boldsymbol{r} \boldsymbol{J}(\boldsymbol{r}) \cdot \bar{\boldsymbol{G}}_1(\boldsymbol{r}, \boldsymbol{r}') = \mu \int_{V_1} d\boldsymbol{r} \bar{\boldsymbol{G}}_1(\boldsymbol{r}', \boldsymbol{r}) \cdot \boldsymbol{J}(\boldsymbol{r}) = \boldsymbol{A}^{inc}(\boldsymbol{r}') \qquad (2.16)
$$

with reciprocity $\bar{\boldsymbol{G}}_1^t(\boldsymbol{r}, \boldsymbol{r}') = \bar{\boldsymbol{G}}_1(\boldsymbol{r}', \boldsymbol{r})$, where 't' represents transpose operation and $\boldsymbol{A}^{inc}$ is the incident magnetic vector potential. Therefore, we have

$$
-\boldsymbol{A}^{inc}(\boldsymbol{r}') \cdot \boldsymbol{a} + \boldsymbol{A}_1(\boldsymbol{r}') \cdot \boldsymbol{a} = \int_S d\boldsymbol{r} \hat{\boldsymbol{n}} \times (\nabla \times \boldsymbol{A}_1(\boldsymbol{r})) \cdot \bar{\boldsymbol{G}}_1(\boldsymbol{r}, \boldsymbol{r}') \cdot \boldsymbol{a}
$$

$$
+ \int_S d\boldsymbol{r} (\hat{\boldsymbol{n}} \times \boldsymbol{A}_1(\boldsymbol{r})) \cdot \nabla \times \bar{\boldsymbol{G}}_1(\boldsymbol{r}, \boldsymbol{r}') \cdot \boldsymbol{a}
$$

$$
- \int_S d\boldsymbol{r} \hat{\boldsymbol{n}} \cdot \left[\nabla \cdot \boldsymbol{A}_1(\boldsymbol{r}) \bar{\boldsymbol{G}}_1(\boldsymbol{r}, \boldsymbol{r}') \cdot \boldsymbol{a} \right]
$$

$$
+ \int_S d\boldsymbol{r} \hat{\boldsymbol{n}} \cdot \left[\boldsymbol{A}_1(\boldsymbol{r}) \nabla \cdot \bar{\boldsymbol{G}}_1(\boldsymbol{r}, \boldsymbol{r}') \cdot \boldsymbol{a} \right]. \qquad (2.17)
$$

At this stage, we once again use the reciprocity of the Green's dyadic and replace $\boldsymbol{r}'$ with $\boldsymbol{r}$, followed by inserting $\bar{\boldsymbol{G}}_1(\boldsymbol{r}, \boldsymbol{r}') = g(\boldsymbol{r}, \boldsymbol{r}')\bar{\boldsymbol{I}}$ and extracting the $\boldsymbol{a}$ vector from both sides. In addition, we impose the boundary conditions on PEC surfaces as [12] $\hat{\boldsymbol{n}} \times \boldsymbol{A}(\boldsymbol{r}) = 0$, $\phi(\boldsymbol{r}) = 0$, and $\nabla \cdot \boldsymbol{A}(\boldsymbol{r}) = 0$. Consequently, the second and third

terms are eliminated in (2.17). Using $\nabla \times \boldsymbol{A}(\boldsymbol{r}) = \mu \boldsymbol{H}(\boldsymbol{r})$ and $\hat{\boldsymbol{n}} \times \boldsymbol{H}(\boldsymbol{r}) = \boldsymbol{J}(\boldsymbol{r})$, the equation becomes

$$\boldsymbol{A}_1(\boldsymbol{r}) = \boldsymbol{A}^{inc}(\boldsymbol{r}) + \mu \int_S d\boldsymbol{r}' \boldsymbol{J}(\boldsymbol{r}') g(\boldsymbol{r}, \boldsymbol{r}') + \int_S d\boldsymbol{r}' \hat{\boldsymbol{n}}' \cdot \boldsymbol{A}(\boldsymbol{r}') \nabla' g(\boldsymbol{r}, \boldsymbol{r}') \quad (2.18)$$

for Region 1. Note that, in Region 2, the left-hand side of the above equation becomes zero as sources are defined only in Region 1. Therefore, we simply have

$$\boldsymbol{A}^{sec}(\boldsymbol{r}) = \mu \int_S d\boldsymbol{r}' \boldsymbol{J}(\boldsymbol{r}') g(\boldsymbol{r}, \boldsymbol{r}') + \int_S d\boldsymbol{r}' \hat{\boldsymbol{n}}' \cdot \boldsymbol{A}(\boldsymbol{r}') \nabla' g(\boldsymbol{r}, \boldsymbol{r}') \quad (2.19)$$

as a main equation for PIEs. Taking the divergence of both sides in (2.19), we obtain

$$\nabla \cdot \boldsymbol{A}^{sec}(\boldsymbol{r}) = \mu \int_S d\boldsymbol{r}' \nabla \cdot \left[\boldsymbol{J}(\boldsymbol{r}') g(\boldsymbol{r}, \boldsymbol{r}') \right]$$
$$- \int_S d\boldsymbol{r}' \hat{\boldsymbol{n}}' \cdot \boldsymbol{A}(\boldsymbol{r}') \nabla' \cdot (\nabla' g(\boldsymbol{r}, \boldsymbol{r}')). \quad (2.20)$$

We note that

$$\nabla \cdot \left[\boldsymbol{J}(\boldsymbol{r}') g(\boldsymbol{r}, \boldsymbol{r}') \right] = g(\boldsymbol{r}, \boldsymbol{r}') \nabla \cdot \boldsymbol{J}(\boldsymbol{r}') + \nabla g(\boldsymbol{r}, \boldsymbol{r}') \cdot \boldsymbol{J}(\boldsymbol{r}')$$
$$= \nabla g(\boldsymbol{r}, \boldsymbol{r}') \cdot \boldsymbol{J}(\boldsymbol{r}')$$
$$= -\nabla' g(\boldsymbol{r}, \boldsymbol{r}') \cdot \boldsymbol{J}(\boldsymbol{r}')$$
$$= -\nabla' \cdot \left[g(\boldsymbol{r}, \boldsymbol{r}') \boldsymbol{J}(\boldsymbol{r}') \right] + g(\boldsymbol{r}, \boldsymbol{r}') \nabla' \cdot \boldsymbol{J}(\boldsymbol{r}'). \quad (2.21)$$
$$\nabla' \cdot (\nabla' g(\boldsymbol{r}, \boldsymbol{r}')) = -\omega^2 \mu \epsilon g(\boldsymbol{r}, \boldsymbol{r}') \quad (2.22)$$

In addition, when plugged into (2.20), the first term in (2.21) vanishes using the divergence theorem. Therefore, using (1.19), we get

$$\phi^{sec}(\boldsymbol{r}) = \frac{1}{i\omega\epsilon} \int_S d\boldsymbol{r}' \nabla' \cdot \boldsymbol{J}(\boldsymbol{r}') g(\boldsymbol{r}, \boldsymbol{r}') - i\omega \int_S d\boldsymbol{r}' \hat{\boldsymbol{n}}' \cdot \boldsymbol{A}(\boldsymbol{r}') g(\boldsymbol{r}, \boldsymbol{r}'). \quad (2.23)$$

Using the boundary condition (1.30) and (1.15), we note that

$$\hat{\boldsymbol{n}} \times \boldsymbol{E}(\boldsymbol{r}) = i\omega \hat{\boldsymbol{n}} \times \boldsymbol{A}(\boldsymbol{r}) - \hat{\boldsymbol{n}} \times \nabla \phi(\boldsymbol{r}) = 0. \quad (2.24)$$

Setting electric scalar potential on the surface to zero leads to

$$i\omega \hat{\boldsymbol{n}} \times \boldsymbol{A}(\boldsymbol{r}) = \hat{\boldsymbol{n}} \times \nabla \phi(\boldsymbol{r}) = 0 \quad (2.25)$$
$$\hat{\boldsymbol{n}} \times \boldsymbol{A}^{sec}(\boldsymbol{r}) = -\hat{\boldsymbol{n}} \times \boldsymbol{A}^{inc}(\boldsymbol{r}). \quad (2.26)$$

Combining (2.26) and (2.19), the first PIE can be obtained as

$$-\hat{\boldsymbol{n}} \times \boldsymbol{A}^{inc}(\boldsymbol{r}) = \hat{\boldsymbol{n}} \times \mu \int_S d\boldsymbol{r}' \boldsymbol{J}(\boldsymbol{r}') g(\boldsymbol{r}, \boldsymbol{r}')$$
$$+ \hat{\boldsymbol{n}} \times \int_S d\boldsymbol{r}' \hat{\boldsymbol{n}}' \cdot \boldsymbol{A}(\boldsymbol{r}') \nabla' g(\boldsymbol{r}, \boldsymbol{r}'). \quad (2.27)$$

19

Similarly, using (2.23) with $\phi^{inc} = -\phi^{sec}$ on the surface, the second PIE can be obtained as

$$-i\omega\epsilon\phi^{inc}(\boldsymbol{r}) = \int_S d\boldsymbol{r}'\nabla'\cdot\boldsymbol{J}(\boldsymbol{r}')g(\boldsymbol{r},\boldsymbol{r}') + \omega^2\epsilon\int_S d\boldsymbol{r}'\hat{\boldsymbol{n}}'\cdot\boldsymbol{A}(\boldsymbol{r}')g(\boldsymbol{r},\boldsymbol{r}'). \quad (2.28)$$

In the following, we consider the solutions of the coupled equations (2.27) and (2.28), which we simply call PIEs.

2.2 Discretization of Potential Integral Equations

PIEs given in (2.27) and (2.28) can be solved together via MoM. Unknowns are the surface current density $\boldsymbol{J}(\boldsymbol{r}')$ and the normal component of the magnetic vector potential, $\hat{\boldsymbol{n}}'\cdot\boldsymbol{A}(\boldsymbol{r}')$. When expanding the unknowns, the RWG functions are used for the surface current density and pulse functions are used for $\hat{\boldsymbol{n}}'\cdot\boldsymbol{A}(\boldsymbol{r}')$. Pulse functions are defined on triangles as

$$b_p^{\text{PLS}}(\boldsymbol{r}) = \begin{cases} 1, & \boldsymbol{r}\in S_p \\ 0, & \boldsymbol{r}\notin S_p. \end{cases} \quad (2.29)$$

With the RWG and pulse functions, unknowns are expanded as

$$\boldsymbol{J}(\boldsymbol{r}') = \sum_{n=1}^{N} x_n \boldsymbol{b}_n^{\text{RWG}}(\boldsymbol{r}') \quad (2.30)$$

$$\hat{\boldsymbol{n}}'\cdot\boldsymbol{A}(\boldsymbol{r}') = \sum_{p=1}^{P} y_p b_p^{\text{PLS}}(\boldsymbol{r}'), \quad (2.31)$$

where N is the number of the RWG functions (edges) and P is the number of triangles on the discretized surface. Discrete forms can be inserted into (2.27) and (2.28), leading to

$$-\hat{\boldsymbol{n}}\times\boldsymbol{A}^{\text{inc}}(\boldsymbol{r}) = \sum_{n=1}^{N} x_n\mu\int_{S_n} d\boldsymbol{r}'g(\boldsymbol{r},\boldsymbol{r}')\hat{\boldsymbol{n}}\times\boldsymbol{b}_n^{\text{RWG}}(\boldsymbol{r}')$$

$$+\sum_{p=1}^{P} y_p\int_{S_p} d\boldsymbol{r}'\hat{\boldsymbol{n}}\times\nabla'g(\boldsymbol{r},\boldsymbol{r}')b_p^{\text{PLS}}(\boldsymbol{r}') \quad (2.32)$$

$$-i\omega\epsilon\Phi_{\text{inc}}(\boldsymbol{r}) = \sum_{n=1}^{N} x_n\int_{S_n} d\boldsymbol{r}'g(\boldsymbol{r},\boldsymbol{r}')\nabla'\cdot\boldsymbol{b}_n^{\text{RWG}}(\boldsymbol{r}')$$

$$+\sum_{p=1}^{P} y_p\omega^2\epsilon\int_{S_p} d\boldsymbol{r}'g(\boldsymbol{r},\boldsymbol{r}')b_p^{\text{PLS}}(\boldsymbol{r}'). \quad (2.33)$$

20

We test (2.32) with the rotational form of the RWG functions and (2.33) with pulse functions to get

$$-\int_{S_m} dr \boldsymbol{t}_m^{\text{RWG}}(\boldsymbol{r}) \cdot \boldsymbol{A}_{inc}(\boldsymbol{r}) = \sum_{n=1}^{N} x_n \mu \int_{S_m} dr \boldsymbol{t}_m^{\text{RWG}}(\boldsymbol{r}) \cdot \int_{S_n} d\boldsymbol{r}' g(\boldsymbol{r}, \boldsymbol{r}') \boldsymbol{b}_n^{\text{RWG}}(\boldsymbol{r}')$$

$$+ \sum_{p=1}^{P} y_p \int_{S_m} dr \boldsymbol{t}_m^{\text{RWG}}(\boldsymbol{r}) \cdot \int_{S_p} d\boldsymbol{r}' \nabla' g(\boldsymbol{r}, \boldsymbol{r}') b_p^{\text{PLS}}(\boldsymbol{r}') \qquad (2.34)$$

$$-i\omega\epsilon \int_{S_q} dr t_q^{\text{PLS}}(\boldsymbol{r}) \Phi_{inc}(\boldsymbol{r}) = \sum_{n=1}^{N} x_n \int_{S_q} dr t_q^{\text{PLS}}(\boldsymbol{r}) \int_{S_n} d\boldsymbol{r}' g(\boldsymbol{r}, \boldsymbol{r}') \nabla' \cdot \boldsymbol{b}_n^{\text{RWG}}(\boldsymbol{r}')$$

$$+ \sum_{p=1}^{P} y_p \omega^2 \epsilon \int_{S_q} dr t_q^{\text{PLS}}(\boldsymbol{r}) \int_{S_p} d\boldsymbol{r}' g(\boldsymbol{r}, \boldsymbol{r}') b_p^{\text{PLS}}(\boldsymbol{r}'). \qquad (2.35)$$

This way, a matrix equation can be obtained with 2 by 2 blocks as

$$\begin{bmatrix} \bar{\boldsymbol{Z}}^{11} & \bar{\boldsymbol{Z}}^{12} \\ \bar{\boldsymbol{Z}}^{21} & \bar{\boldsymbol{Z}}^{22} \end{bmatrix} \cdot \begin{bmatrix} \boldsymbol{x} \\ \boldsymbol{y} \end{bmatrix} = \begin{bmatrix} \boldsymbol{w}_m^{\text{RHS}} \\ \boldsymbol{w}_q^{\text{RHS}} \end{bmatrix}, \qquad (2.36)$$

where the matrix elements can be found as

$$Z_{mn}^{11} = \mu \int_{S_m} dr \boldsymbol{t}_m^{\text{RWG}}(\boldsymbol{r}) \cdot \int_{S_n} d\boldsymbol{r}' g(\boldsymbol{r}, \boldsymbol{r}') \boldsymbol{b}_n^{\text{RWG}}(\boldsymbol{r}') \qquad (2.37)$$

$$Z_{mp}^{12} = \int_{S_m} dr \boldsymbol{t}_m^{\text{RWG}}(\boldsymbol{r}) \cdot \int_{S_p} d\boldsymbol{r}' \nabla' g(\boldsymbol{r}, \boldsymbol{r}') b_p^{\text{PLS}}(\boldsymbol{r}') \qquad (2.38)$$

$$Z_{qn}^{21} = \int_{S_q} dr t_q^{\text{PLS}}(\boldsymbol{r}) \int_{S_n} d\boldsymbol{r}' g(\boldsymbol{r}, \boldsymbol{r}') \nabla' \cdot \boldsymbol{b}_n^{\text{RWG}}(\boldsymbol{r}') \qquad (2.39)$$

$$Z_{qp}^{22} = \omega^2 \epsilon \int_{S_q} dr t_q^{\text{PLS}}(\boldsymbol{r}) \int_{S_p} d\boldsymbol{r}' g(\boldsymbol{r}, \boldsymbol{r}') b_p^{\text{PLS}}(\boldsymbol{r}'). \qquad (2.40)$$

We further note that

$$Z_{mp}^{12} = -\int_{S_m} dr \boldsymbol{t}_m^{\text{RWG}}(\boldsymbol{r}) \cdot \int_{S_p} d\boldsymbol{r}' \nabla g(\boldsymbol{r}, \boldsymbol{r}') b_p^{\text{PLS}}(\boldsymbol{r}') \qquad (2.41)$$

$$= -\int_{S_m} d\boldsymbol{r} \nabla \cdot \left[\boldsymbol{t}_m^{\text{RWG}}(\boldsymbol{r}) \int_{S_p} d\boldsymbol{r}' g(\boldsymbol{r}, \boldsymbol{r}') b_p^{\text{PLS}}(\boldsymbol{r}') \right]$$

$$+ \int_{S_m} d\boldsymbol{r} \nabla \cdot \boldsymbol{t}_m^{\text{RWG}}(\boldsymbol{r}) \int_{S_p} d\boldsymbol{r}' g(\boldsymbol{r}, \boldsymbol{r}') b_p^{\text{PLS}}(\boldsymbol{r}') \qquad (2.42)$$

$$= \int_{S_m} d\boldsymbol{r} \nabla \cdot \boldsymbol{t}_m^{\text{RWG}}(\boldsymbol{r}) \int_{S_p} d\boldsymbol{r}' g(\boldsymbol{r}, \boldsymbol{r}') b_p^{\text{PLS}}(\boldsymbol{r}'). \qquad (2.43)$$

Therefore, $\bar{\boldsymbol{Z}}^{12}$ and $\bar{\boldsymbol{Z}}^{21}$ are the transpose of each other. Finally, excitation vectors

21

can be written as

$$w_m^{\text{RHS}} = -\int_{S_m} d\boldsymbol{r} \boldsymbol{t}_m^{\text{RWG}}(\boldsymbol{r}) \cdot \boldsymbol{A}_{inc}(\boldsymbol{r}) \tag{2.44}$$

$$w_q^{\text{RHS}} = -i\omega\epsilon \int_{S_q} d\boldsymbol{r} t_q^{\text{PLS}}(\boldsymbol{r}) \phi_{\text{inc}}(\boldsymbol{r}). \tag{2.45}$$

2.3 Excitation

In the field integral equations, the excitation is directly vector fields, such as the electric field intensity for EFIE and the magnetic field intensity for MFIE. However, for PIEs, the excitations must be incident potentials. Therefore, there is a need to define incoming potentials that are equivalent to field excitations.

2.3.1 Plane Wave

Field intensities of an incoming plane wave can be written as

$$\boldsymbol{E}^{inc}(\boldsymbol{r}) = \boldsymbol{E}_p e^{i\boldsymbol{k}\cdot\boldsymbol{r}} \tag{2.46}$$

$$\boldsymbol{H}^{inc}(\boldsymbol{r}) = \frac{\hat{\boldsymbol{k}}}{\eta} \times \boldsymbol{E}^{inc}(\boldsymbol{r}), \tag{2.47}$$

where $\hat{\boldsymbol{k}} = \boldsymbol{k}/k$ is the direction of propagation and $\boldsymbol{E}_p$ is the polarization vector. Using the magnetic vector potential $\boldsymbol{A}(\boldsymbol{r})$, a plane-wave incidence can be written as [13]

$$\boldsymbol{A}^{inc}(\boldsymbol{r}) = -\hat{\boldsymbol{k}}(\boldsymbol{r} \cdot \boldsymbol{E}_p)\sqrt{\mu\epsilon} e^{i\boldsymbol{k}\cdot\boldsymbol{r}}. \tag{2.48}$$

Then, with the help of the Lorentz Gauge in (1.19), the corresponding electric scalar potential can be found as

$$\phi^{inc}(\boldsymbol{r}) = -\boldsymbol{r} \cdot \boldsymbol{E}_p e^{i\boldsymbol{k}\cdot\boldsymbol{r}}. \tag{2.49}$$

It can be shown that $\nabla \times \boldsymbol{A}^{inc}(\boldsymbol{r}) = \mu\boldsymbol{H}^{inc}(\boldsymbol{r})$ is satisfied.

22

2.3.2 Hertzian Dipole

Hertzian dipole excitation can simply be written as

$$\boldsymbol{A}^{\text{inc}}(\boldsymbol{r}) = \mu \boldsymbol{I_D} g(\boldsymbol{r}, \boldsymbol{r}_D) \tag{2.50}$$

$$\phi^{\text{inc}}(\boldsymbol{r}) = 0, \tag{2.51}$$

where $\boldsymbol{I_D}$ is the dipole moment and $\boldsymbol{r}_D$ is the location of the dipole.

2.3.3 Delta-Gap Excitation

Using (1.15) and with the definition of delta-gap function [8], we can use

$$\boldsymbol{A}^{\text{inc}}(\boldsymbol{r}) = \frac{I_n}{i\omega} \lim_{d \to 0} \frac{\hat{\boldsymbol{u}}\delta(\boldsymbol{r}, \boldsymbol{r}_n)}{d}, \tag{2.52}$$

where I_n represents the feed strength, $\hat{\boldsymbol{u}}$ is the unit vector normal to the RWG edge, and $\boldsymbol{r}_n$ represents locations on the edge.

2.4 Preconditioner

In order to obtain better-conditioned matrix equations from PIEs, the block matrices can be scaled as

$$\begin{bmatrix} \kappa^2 \bar{\boldsymbol{Z}}_{11} & \kappa \bar{\boldsymbol{Z}}_{12} \\ \kappa \bar{\boldsymbol{Z}}_{21} & \bar{\boldsymbol{Z}}_{22} \end{bmatrix} \cdot \begin{bmatrix} \boldsymbol{x}/\kappa \\ \boldsymbol{y} \end{bmatrix} = \begin{bmatrix} \kappa \boldsymbol{w}_m^{\text{RHS}} \\ \boldsymbol{w}_q^{\text{RHS}} \end{bmatrix}, \tag{2.53}$$

where κ is a frequency dependent scaling coefficient that can be optimized for a problem. For example, $\kappa = f/10$ can be used for a uniformly discretized sphere of radius 0.3 m. By this scaling, the condition number of the corresponding impedance matrix can be reduced significantly.

Table 2.1 presents condition numbers for impedance matrices obtained from PIEs with and without the scaling. A sphere of radius 0.3 m discretized with 10 cm triangles is considered. The number of unknowns is 850. The values listed in Table 2.1 show that there is a significant decrease in condition numbers at high frequencies. However, it can be seen that, for very low frequencies, condition numbers are

Table2.1: Condition numbers of matrices obtained by the discretization of a PEC sphere at different frequencies. The number of unknowns is 850.

Frequency (Hz)	Original PIEs	Scaled PIEs
1e9	7.7e15	6.3e1
1e8	8.5e13	3.6e1
1e7	9.1e11	8.9e1
1e6	9.1e9	8.2e2
1e5	9.3e7	8.1e3
1e4	7.1e7	8.1e4
1e3	7.1e7	8.1e5
1e2	7.1e7	8.1e6
1e1	8.1e7	8.1e7
1e0	8.1e9	8.1e8

still large. Therefore, one may need more powerful techniques similar to constraint preconditioner proposed in [15] for very low frequencies.

2.5   Numerical Results

In this section, we present some numerical results on the MoM solutions of PIEs. First, we consider a scattering problem involving a PEC sphere with radius 0.3 m. The sphere, which is discretized with 4080 RWG functions and 2720 triangular patches, is illuminated by plane waves at different frequencies, propagating in the z direction with polarization direction of x, as depicted in Figure 2.2. Total magnetic vector and electric scalar potentials are calculated in the vicinity of the sphere. As depicted in Figures 2.3 and 2.4, we obtain zero potentials inside the sphere at 1 MHz [12]. Far-zone scattered electric field results at two different frequencies can be found in Figure 2.5. It is seen that PIE results match with analytical (Mie series) solutions [16] at both 1 GHz and 1 Hz. However, EFIE gives incorrect results for the latter. In Figure 2.6, the surface current density induced on the sphere is shown, again at two different frequencies. The breakdown of EFIE can be seen again in the 1-Hz results. More details on the low-frequency breakdown are given in Chapter 3.
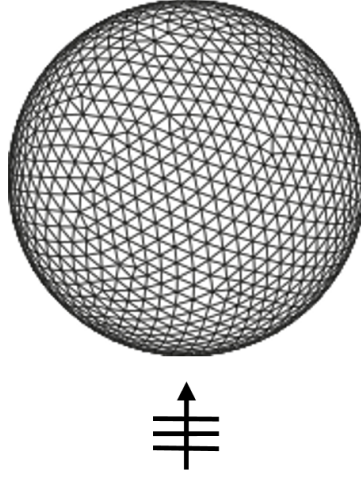
24

Figure 2.2: Excitation configuration for the sphere problems.

Next, a PEC cube having edges of 0.6 m is discretized with 4050 RWG functions and 2700 triangular patches. Similar to the sphere case, z-directed x-polarized plane waves are used for excitations as shown in Figure 2.7. In Figure 2.8 and Figure 2.9, far-zone scattered fields and surface current densities are shown for 100 MHz and 1 Hz. Again, at low frequencies, EFIE results become incorrect, while PIE gives accurate results.

In Figures 2.10 and 2.11, a delta-gap excited cage-dipole antenna [17] is analyzed by using EFIE and PIEs. We note that the operation frequency is far away from the low-frequency breakdown region of EFIE (see Chapter 3); thus both EFIE and PIE work well and provide consistent results at the given frequencies, showing the applicability of delta-gap excitations via potentials.
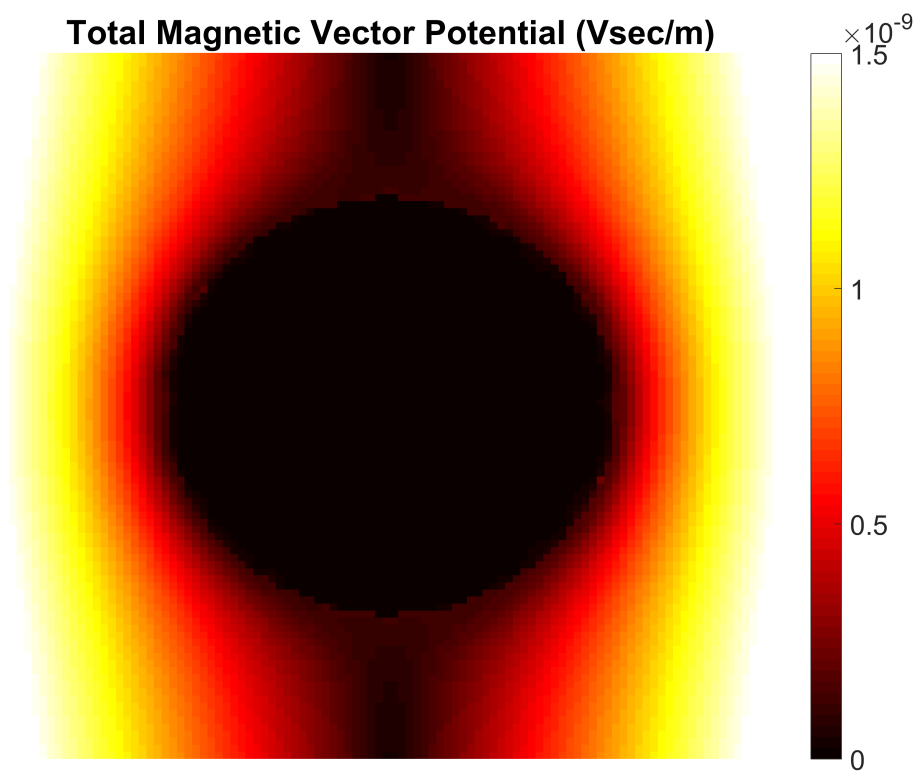
Figure 2.3: Total magnetic vector potential in the vicinity of a PEC sphere. Equation (2.19) is used for the calculation of the scattered magnetic vector potential.
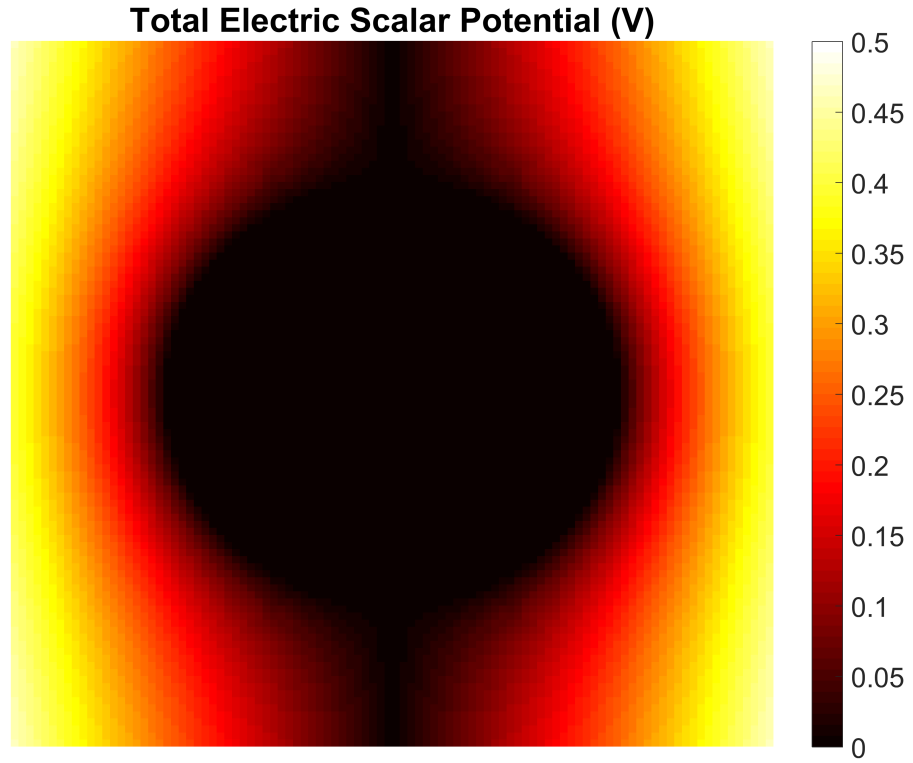
Total Electric Scalar Potential (V)

Figure 2.4: Total electric scalar potential in the vicinity of a PEC sphere. Equation (2.23) is used for the calculation of the scattered electric scalar potential.
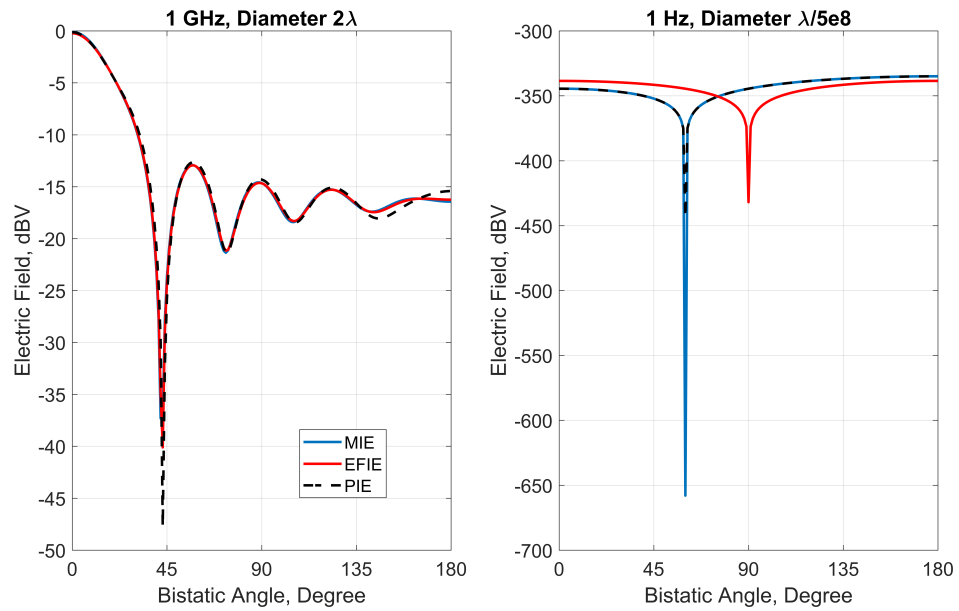

Figure 2.5: Far-zone electric field scattered from a conducting sphere of 0.3 m radius at 1 GHz and 1 Hz.
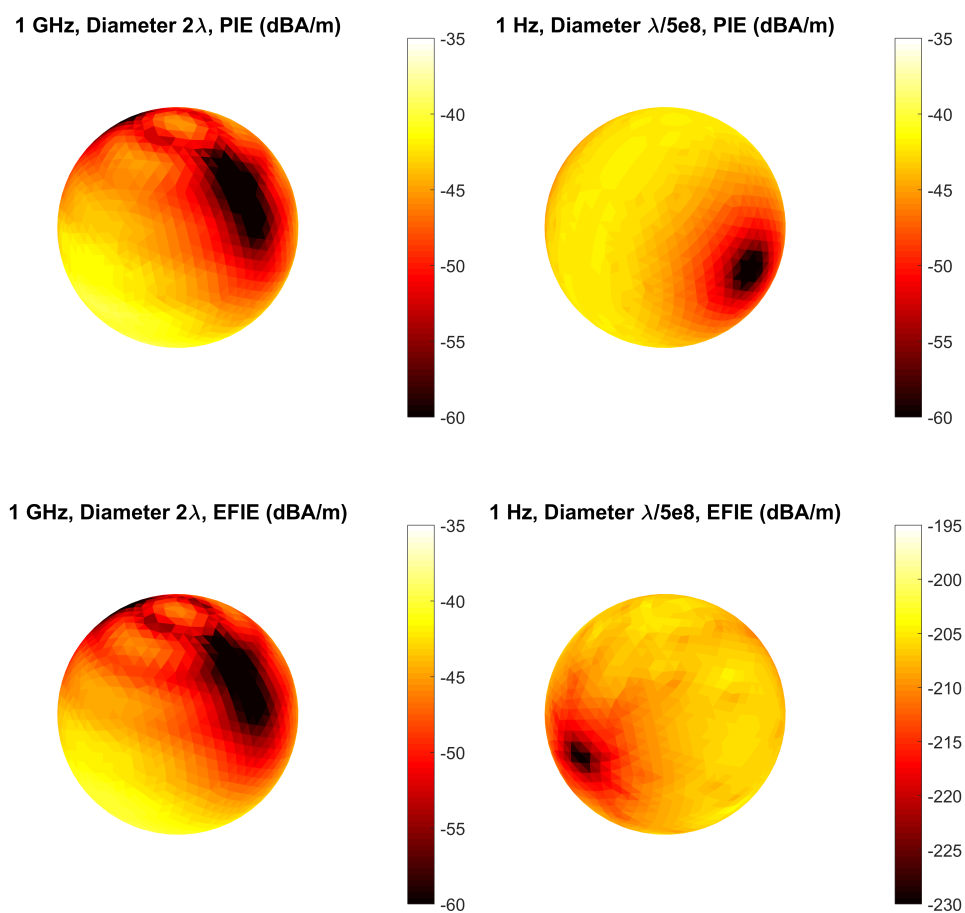
Figure 2.6: Electric current density induced on a conducting sphere at two different frequencies.
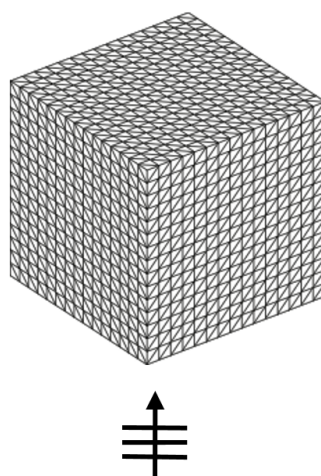

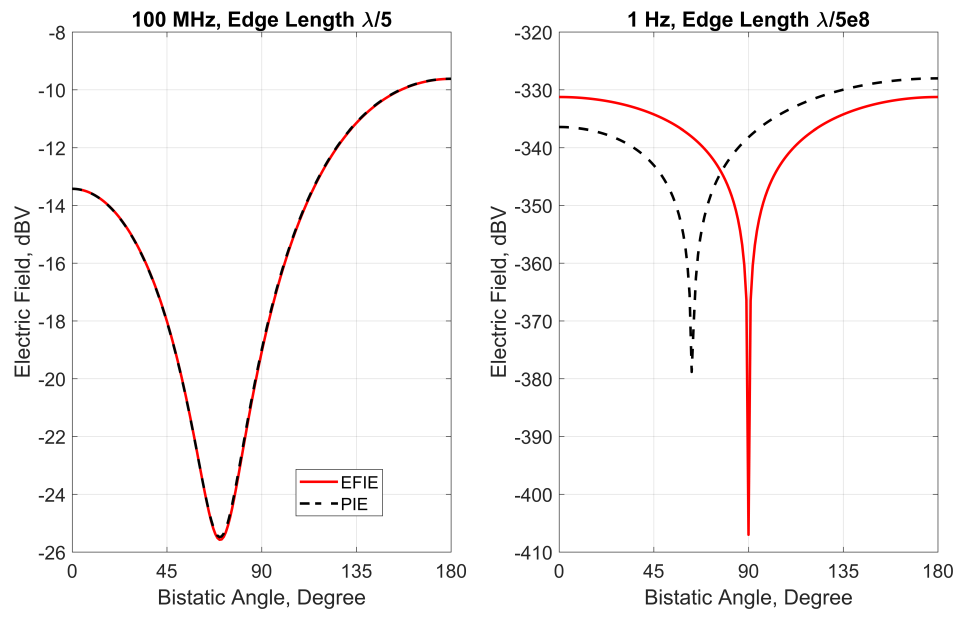Figure 2.7: Excitation configuration for the cube problems.

Figure 2.8: Far-zone electric field scattered from a conducting cube with 0.6 m edges at 100 MHz and 1 Hz.
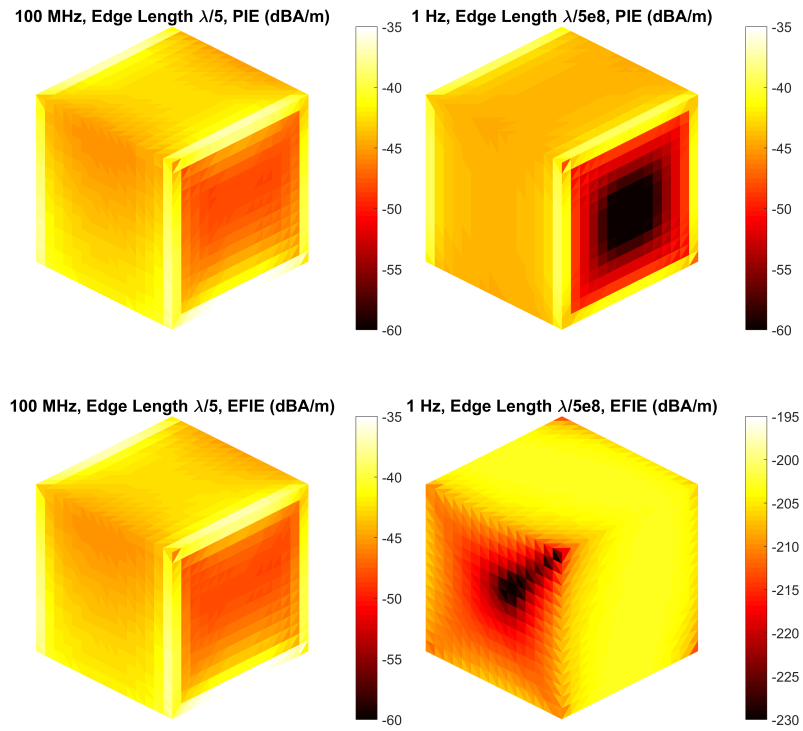

Figure 2.9: Electric current density induced on a conducting cube at two different frequencies.
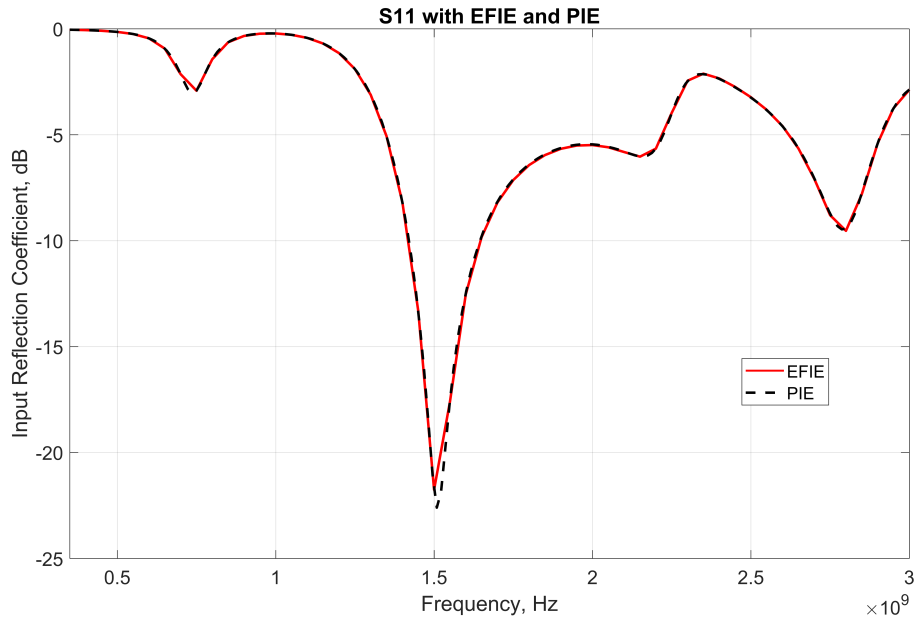
Figure 2.10: Input reflection coefficient values at different frequencies of a cage-dipole antenna excited via delta-gap [17].
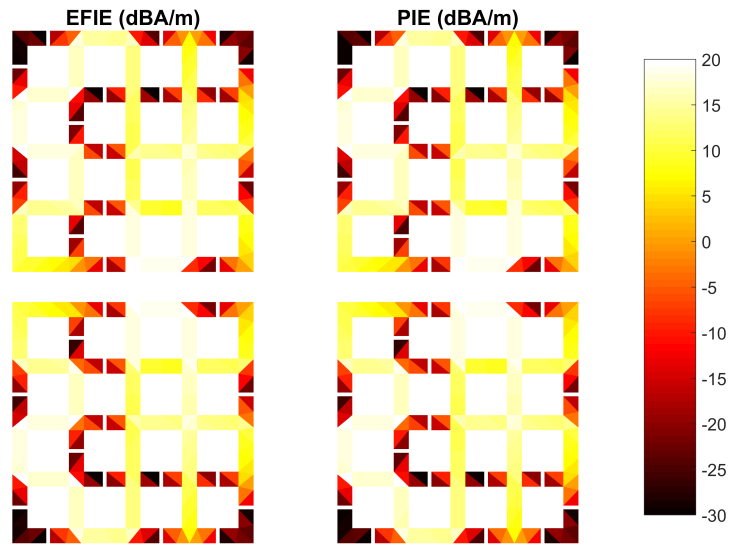

Figure 2.11: Electric current density induced on a cage-dipole antenna [17] at 1.5 GHz.

CHAPTER 3

LOW-FREQUENCY BREAKDOWN

Even though there are a lot of studies on the low-frequency breakdown [18], there is no study that demonstrates a clear picture with a complete description of breakdown mechanisms when standard RWG functions are employed for surface integral equations. In this chapter, a detailed description of the low-frequency breakdown is given with an accuracy analysis of sources and fields for both EFIE and PIEs. In addition, a remedy for the hidden low-frequency breakdown of PIEs is proposed. Explanations on the characteristics of the low-frequency breakdown of EFIE and PIEs are analyzed and supported by numerical results.

As Helmholtz theorem states, a vector field can be decomposed into irrotational and solenoidal parts. For example, for the electric current density, one can write

$$\boldsymbol{J}(\boldsymbol{r}) = \boldsymbol{J}_{irr}(\boldsymbol{r}) + \boldsymbol{J}_{sol}(\boldsymbol{r}). \tag{3.1}$$

In this decomposition, the irrotational part is curl-free and the solenoidal part is divergence-free. Therefore, we have

$$\nabla \cdot \boldsymbol{J}(\boldsymbol{r}) = \nabla \cdot \boldsymbol{J}_{irr}(\boldsymbol{r}) \tag{3.2}$$

$$\nabla \times \boldsymbol{J}(\boldsymbol{r}) = \nabla \times \boldsymbol{J}_{sol}(\boldsymbol{r}). \tag{3.3}$$

At low-frequencies $\boldsymbol{J}_{sol}(\boldsymbol{r})$ dominates $\boldsymbol{J}_{irr}(\boldsymbol{r})$, i.e., $\boldsymbol{J}_{sol}(\boldsymbol{r}) \gg \boldsymbol{J}_{irr}(\boldsymbol{r})$.

Investigating (1.51) at low frequencies, it is seen that near-zone electric field intensity involves $\nabla \cdot \boldsymbol{J}_{irr}(\boldsymbol{r})$, or considering the continuity equation, the electric charge $\rho(\boldsymbol{r})$. Equation (1.52) implies that near-zone magnetic field intensity consists of the overall current density $\boldsymbol{J}(\boldsymbol{r})$, which is dominated naturally by $\boldsymbol{J}_{sol}(\boldsymbol{r})$. Equation (1.53) further points out that the far-zone electric field intensity is, again, created by the overall

current density $\boldsymbol{J}(\boldsymbol{r})$, which is dominated naturally by $\boldsymbol{J}_{sol}(\boldsymbol{r})$. Therefore, in order to get a complete set of accurate solutions by using an integral equation, both $\boldsymbol{J}_{sol}(\boldsymbol{r})$ and $\boldsymbol{J}_{irr}(\boldsymbol{r})$ should be captured well.

In the literature, expanding the current density using special discretization functions, such as dual functions [19], separating the current density into solenoidal and non-solenoidal components using loop-star decomposition [20], and expanding charge density as a separate quantity [21, 22] as done in augmented-EFIE (A-EFIE) are used in order to avoid the low-frequency breakdown. PIEs, on the other hand, do not need special discretizations and an explicit expansion of the charge density.

3.1 Breakdown in EFIE

As derived in Chapter 1, EFIE for a PEC object can be written as

$$-\boldsymbol{E}^{inc}(\boldsymbol{r}) = i\omega\mu \int d\boldsymbol{r}' \boldsymbol{J}(\boldsymbol{r}')g(\boldsymbol{r}, \boldsymbol{r}') - \frac{1}{i\omega\epsilon} \int d\boldsymbol{r}' \nabla' \cdot \boldsymbol{J}(\boldsymbol{r}')\nabla g(\boldsymbol{r}, \boldsymbol{r}') \qquad (3.4)$$

that consists of a vector potential and a scalar potential term as

$$-\boldsymbol{E}^{inc}(\boldsymbol{r}) = \boldsymbol{E}_{VP}(\boldsymbol{r}) + \boldsymbol{E}_{SP}(\boldsymbol{r}),$$

where

$$\boldsymbol{E}_{VP}(\boldsymbol{r}) = i\omega\mu \int d\boldsymbol{r}' \boldsymbol{J}(\boldsymbol{r}')g(\boldsymbol{r}, \boldsymbol{r}') \qquad (3.5)$$

$$\boldsymbol{E}_{SP}(\boldsymbol{r}) = -\frac{1}{i\omega\epsilon} \int d\boldsymbol{r}' \nabla' \cdot \boldsymbol{J}(\boldsymbol{r}')\nabla g(\boldsymbol{r}, \boldsymbol{r}'). \qquad (3.6)$$

As the frequency drops, the scalar potential term that scales with $1/\omega$ dominates the vector potential term that scales with ω. We call this field imbalance that coexists with the ill-conditioning of the impedance matrix. At low-frequencies, EFIE turns into

$$-\boldsymbol{E}^{inc}(\boldsymbol{r}) \approx \boldsymbol{E}_{SP}(\boldsymbol{r}) = -\frac{1}{i\omega\epsilon} \int d\boldsymbol{r}' \nabla' \cdot \boldsymbol{J}(\boldsymbol{r}')\nabla g(\boldsymbol{r}, \boldsymbol{r}'). \qquad (3.7)$$

In (3.7), it can be seen that, the only part of the current represented in EFIE is the irrotational part $\boldsymbol{J}_{irr}(\boldsymbol{r})$, while the solenoidal part $\boldsymbol{J}_{sol}(\boldsymbol{r})$ is completely lost. Considering the continuity equation (1.8), $\nabla \cdot \boldsymbol{J}_{irr}(\boldsymbol{r})$ can be interpreted as the electric

charge $\rho(\boldsymbol{r})$. Therefore at low frequencies, EFIE includes $\boldsymbol{J}_{irr}(\boldsymbol{r})$ and $\rho(\boldsymbol{r})$, while it excludes $\boldsymbol{J}_{sol}(\boldsymbol{r})$.

Unless all the precision is consumed by the ill-conditioning, since (3.7) can capture $\boldsymbol{J}_{irr}(\boldsymbol{r})$, EFIE can provide correct $\boldsymbol{J}_{irr}(\boldsymbol{r})$, $\nabla \cdot \boldsymbol{J}_{irr}(\boldsymbol{r})$ or $\rho(\boldsymbol{r})$, and thus near-zone electric field intensity at low frequencies. However, since the dominant part of the current $\boldsymbol{J}_{sol}(\boldsymbol{r})$ is lost, overall current $\boldsymbol{J}(\boldsymbol{r})$, far-zone electric fields, and near-zone magnetic fields become inaccurate.

3.2   Breakdown in PIEs

Even though, the main point of using PIEs is to get rid of the low-frequency breakdown, a detailed analysis reveals that PIEs have a hidden low-frequency breakdown [23]. As the frequency becomes lower, $\boldsymbol{J}_{sol}(\boldsymbol{r})$ dominates over $\boldsymbol{J}_{irr}(\boldsymbol{r})$. That creates an imbalance in the sources, which we call source imbalance. At extremely low frequencies, due to finite numerical precision, $\boldsymbol{J}_{irr}(\boldsymbol{r})$ is completely lost. Therefore PIEs, as the electric charge (or irrotational current) is not expanded directly unlike A-EFIE, suffer from source imbalance ($\boldsymbol{J}(\boldsymbol{r})$ and $\hat{\boldsymbol{n}} \cdot \boldsymbol{A}(\boldsymbol{r})$ are expanded in PIEs).

The accuracy of PIEs for the far-zone scattered fields is well-known in the literature [24]. That accuracy comes from $\boldsymbol{J}_{sol}(\boldsymbol{r})$. As $\boldsymbol{J}_{sol}(\boldsymbol{r})$ is captured well, and since $\boldsymbol{J}_{sol}(\boldsymbol{r})$ is the dominant contributor in currents at low frequencies, the overall current $\boldsymbol{J}(\boldsymbol{r})$, as well as far-zone electric fields and near-zone magnetic fields obtained by using PIEs are accurate. However, since $\boldsymbol{J}_{irr}(\boldsymbol{r})$ is lost at extremely low-frequencies, $\nabla \cdot \boldsymbol{J}_{irr}(\boldsymbol{r})$ or $\rho(\boldsymbol{r})$ and near-zone electric fields can be inaccurate.

3.2.1   Remedy for the Low-Frequency Breakdown of PIEs

In order to get accurate charges and near-zone electric fields using PIEs, one can solve an additional integral equation. The boundary condition for the electric charge density can be written in terms of the potentials (1.15) as

$$\rho(\boldsymbol{r}') = \epsilon \hat{\boldsymbol{n}}' \cdot \boldsymbol{E}(\boldsymbol{r}') = i\omega\epsilon\hat{\boldsymbol{n}}' \cdot \boldsymbol{A}(\boldsymbol{r}') - \epsilon\hat{\boldsymbol{n}}' \cdot \nabla'\phi(\boldsymbol{r}'), \tag{3.8}$$

Table3.1: Summary for the accuracies obtained with EFIE, PIEs, and PIE-GSP.

	EFIE	**PIEs**	**PIE-GSP**
Breakdown	Field Imbalance	Source Imbalance	-
Conditioning	Bad	Better	-
$\boldsymbol{J}_{irr}$	Accurate	Vanishes Eventually	-
$\boldsymbol{J}_{sol}$	Inaccurate	Accurate	-
Electric Charge	Accurate	Inaccurate	Accurate
Electric Current	Inaccurate	Accurate	-
Near-zone Electric Field	Accurate	Inaccurate	Accurate
Near-zone Magnetic Field	Inaccurate	Accurate	-
Far-zone Field	Inaccurate	Accurate	-

which can be combined with (2.28) to get

$$-\phi^{sec}(\boldsymbol{r}) = \int d\boldsymbol{r}'\hat{\boldsymbol{n}}' \cdot \nabla'\phi(\boldsymbol{r}')g(\boldsymbol{r},\boldsymbol{r}'). \qquad (3.9)$$

Then, using the boundary condition for scalar potentials, i.e., $\phi^{sec}(\boldsymbol{r}) + \phi^{inc}(\boldsymbol{r}) = 0$ on PEC surfaces, we obtain

$$\phi^{inc}(\boldsymbol{r}) = \int d\boldsymbol{r}'\hat{\boldsymbol{n}}' \cdot \nabla'\phi(\boldsymbol{r}')g(\boldsymbol{r},\boldsymbol{r}'). \qquad (3.10)$$

In this equation, $\hat{\boldsymbol{n}}' \cdot \nabla'\phi(\boldsymbol{r}')$ is the unknown function that can be expanded with pulse basis functions. Then, the equation can be tested with pulse functions to get a new linear system of equations. Finally, the solution of the system can be combined with the output of PIEs, namely $\nabla \cdot \boldsymbol{J}_{irr}(\boldsymbol{r})$, to get accurate charges via (3.8). We call this method PIE with gradient of the scalar potential (PIE-GSP).

A summary for the accuracies for EFIE, PIEs, and PIE-GSP is given in Table 3.1.

3.3 Numerical Results

In Figures 3.1, 3.2, 3.3, 3.4, and 3.5, we consider scattering problems involving a sphere with radius 0.3 m illuminated by a plane wave with x polarization propagating in the z direction. First, in Figure 3.1, it can be seen that, when the diameter becomes smaller than $\lambda/500$, the electric current density induced on the surface of the sphere

starts to deviate for EFIE and PIE solutions. Inaccurate $\boldsymbol{J}_{sol}(\boldsymbol{r})$ is the reason for the breakdown of EFIE. The PIE implementation gives accurate results for all sizes of the sphere, from 2λ to $\lambda/500000000$ since the dominant current $\boldsymbol{J}_{sol}(\boldsymbol{r})$ is represented well in PIEs. Similarly, as depicted in Figure 3.2, we obtain a perfect match between analytical solutions and PIEs, while there is an obvious breakdown for EFIE due to inaccurate $\boldsymbol{J}_{sol}(\boldsymbol{r})$.

As shown in Figure 3.3, since $\boldsymbol{J}_{irr}(\boldsymbol{r})$ is well represented in EFIE, charge density distributions are accurately found by using this formulation. However, using PIEs, at extremely low frequencies, inaccuracy can be seen as noisy data. With the method PIE-GSP, electric charges are captured accurately, similar to EFIE.

Figure 3.4 shows near-zone electric and magnetic fields in the vicinity of the PEC sphere, again at different frequencies. For near-zone electric fields, similar to electric charges, EFIE is accurate, the PIE implementation is inaccurate, and PIE-GSP is accurate. For near-zone magnetic fields, as the dominating term is $\boldsymbol{J}_{sol}(\boldsymbol{r})$, EFIE is inaccurate, while the PIE implementation is accurate. We note that near-zone magnetic fields converge into the excitation term as the frequency goes down for EFIE.

Figure 3.5 presents an interesting set of results, where the power density in the vicinity of the PEC sphere is shown. At low frequencies, EFIE fails because of inaccurate near-zone magnetic fields. The PIE implementation also fails due to inaccuracy in the near-zone electric fields. However, using PIE-GSP, the results are accurate in the entire spectrum.

Similar to the results for a PEC sphere, we present results for a PEC cube with edges of 0.6 m. We have electric current density distributions in Figure 3.6, far-zone scattered electric fields in Figure 3.7, electric charge density distributions in Figure 3.8, near-zone electric and magnetic fields in Figure 3.9, and power density distributions in Figure 3.10.

Furthermore, as shown in Figure 3.11, in order to obtain quantitative results, we take samples near the boundary of the PEC sphere as $R \in [0.28, 0.295]$, $\theta \in [0, \pi]$, and $\phi \in [0, 2\pi)$. Then, we calculate the near-zone electric field intensity at the sampling points. Root-mean-square values, which correspond to relative errors, are plotted

35

from 1 MHz to 1 Hz in Figure 3.12. As can be seen in the figure, the relative error of the PIE implementation increases below 100 kHz, while PIE-GSP and EFIE results remain at the same error levels.
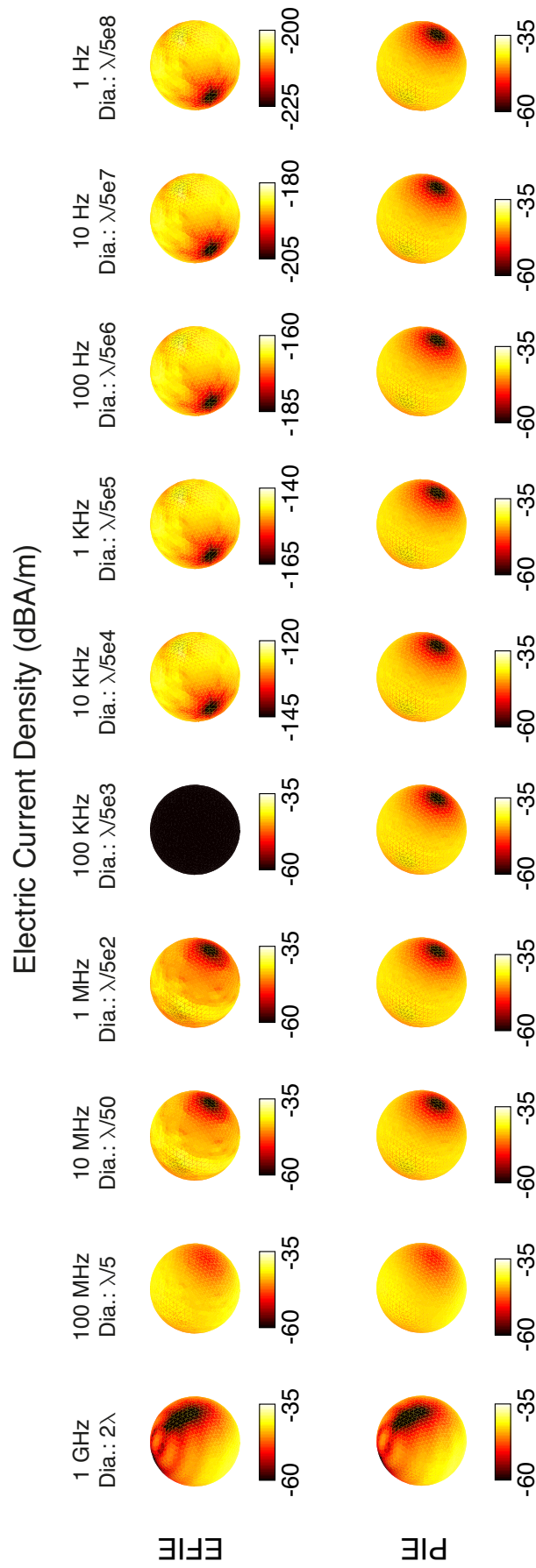
Electric Current Density (dBA/m)

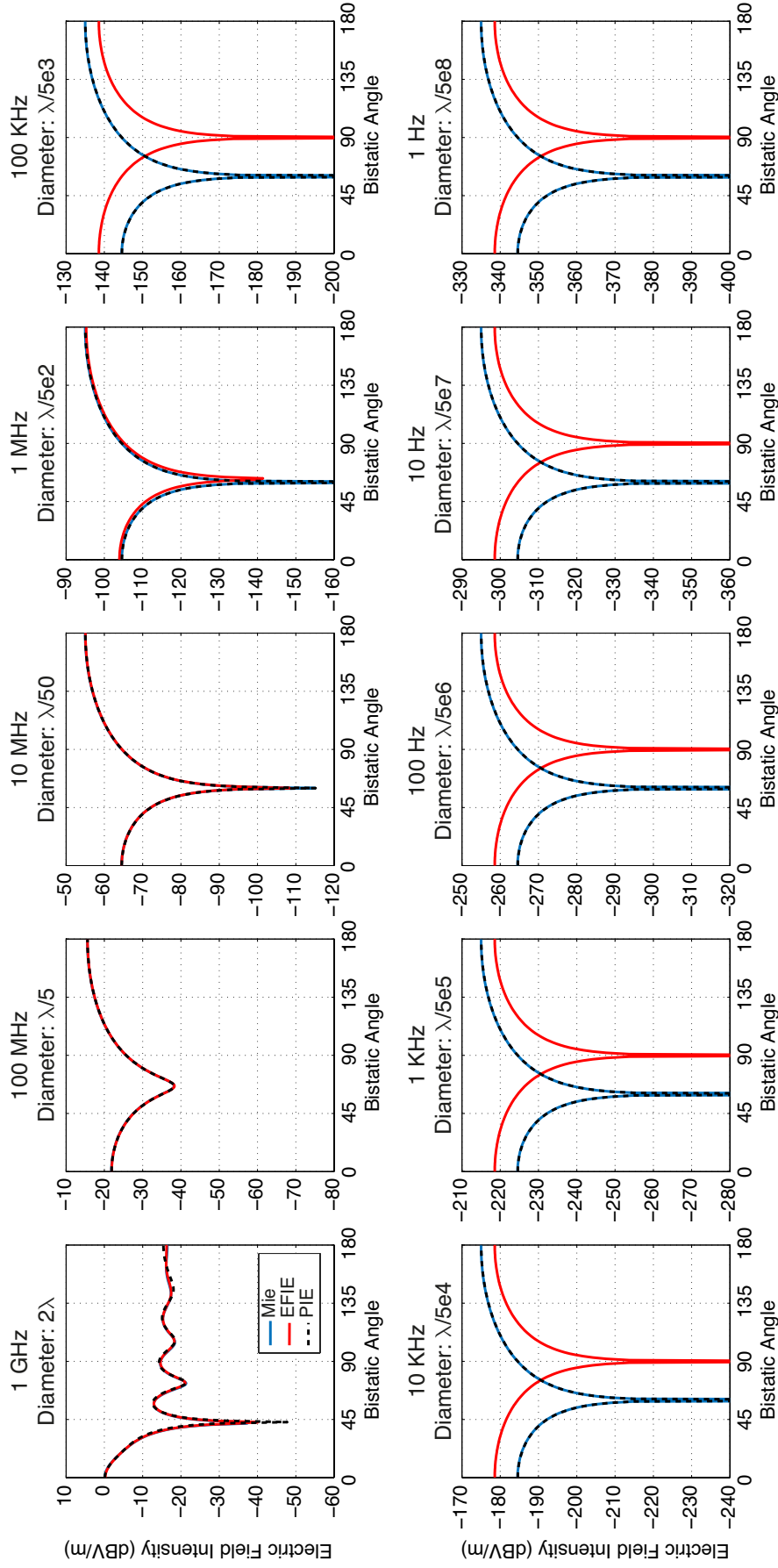Figure 3.1: Surface current density distributions on a PEC sphere of radius 0.3 m at different frequencies.

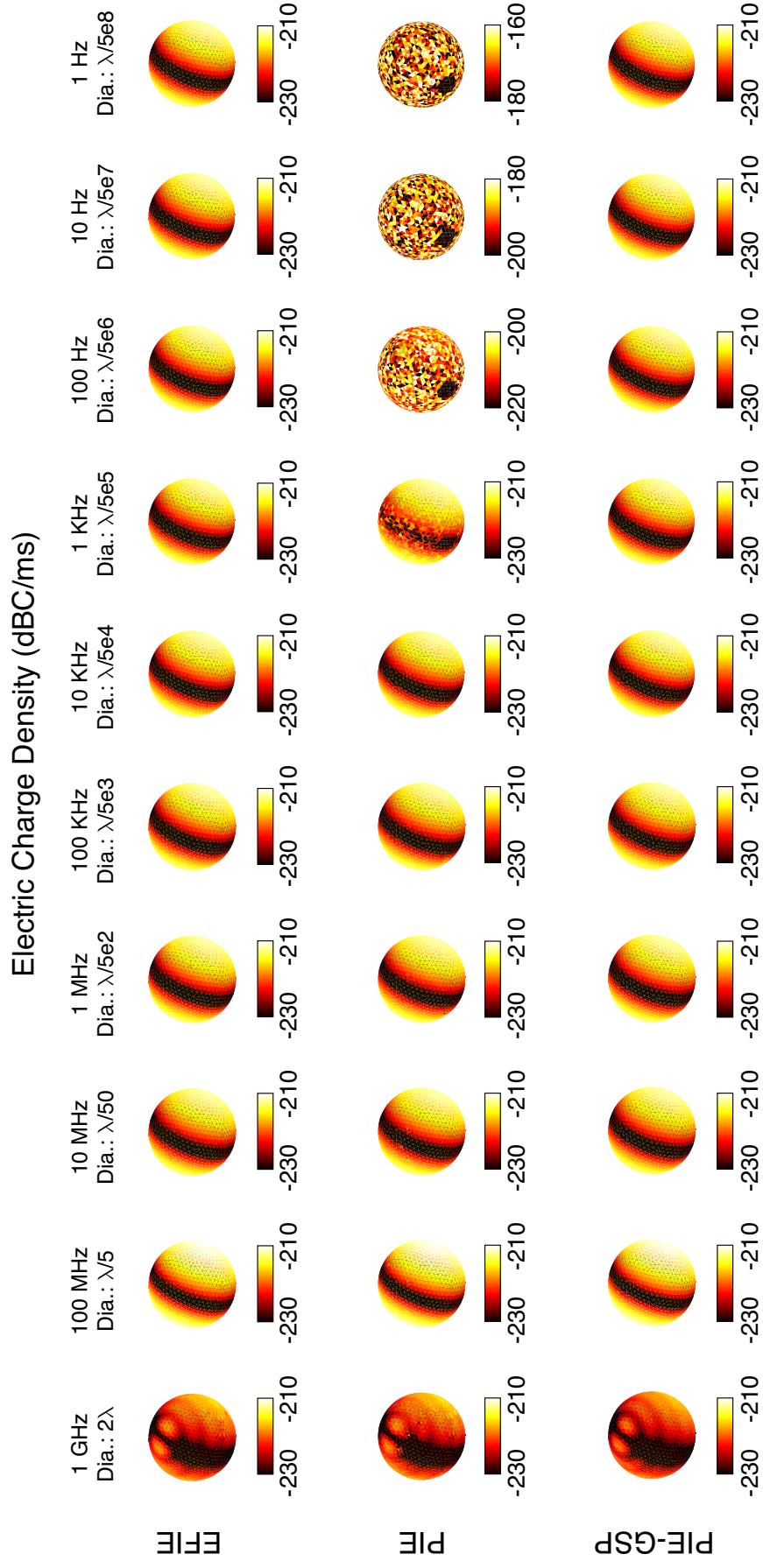Figure 3.2: Far-zone electric field intensity scattered from a PEC sphere of radius 0.3 m at different frequencies.

Electric Charge Density (dBC/ms)

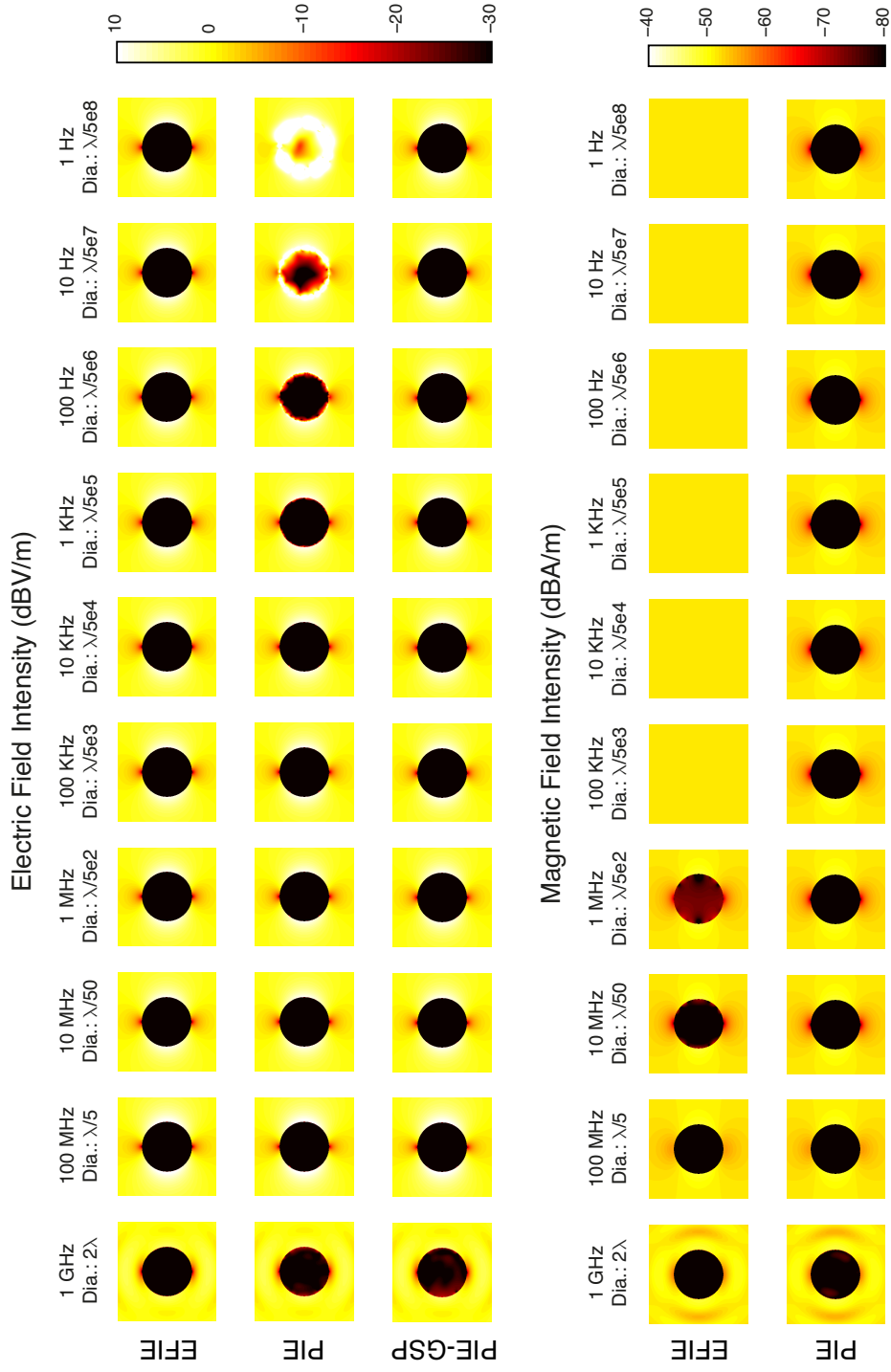Figure 3.3: Surface charge density distributions on a PEC sphere of radius 0.3 m at different frequencies.

Figure 3.4: Near-zone electric and magnetic fields in the vicinity of a PEC sphere of radius 0.3 m at different frequencies.
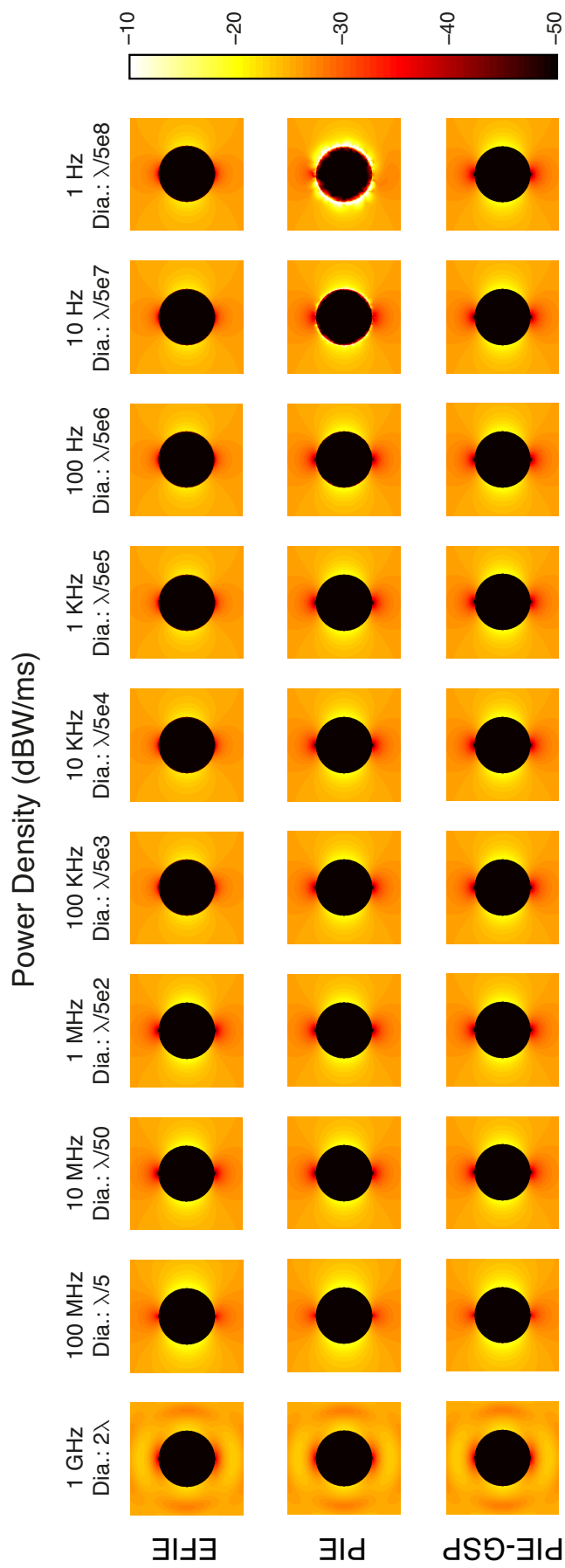
Power Density (dBW/ms)

Figure 3.5: Near-zone power density distributions in the vicinity of a PEC sphere of radius 0.3 m at different frequencies.
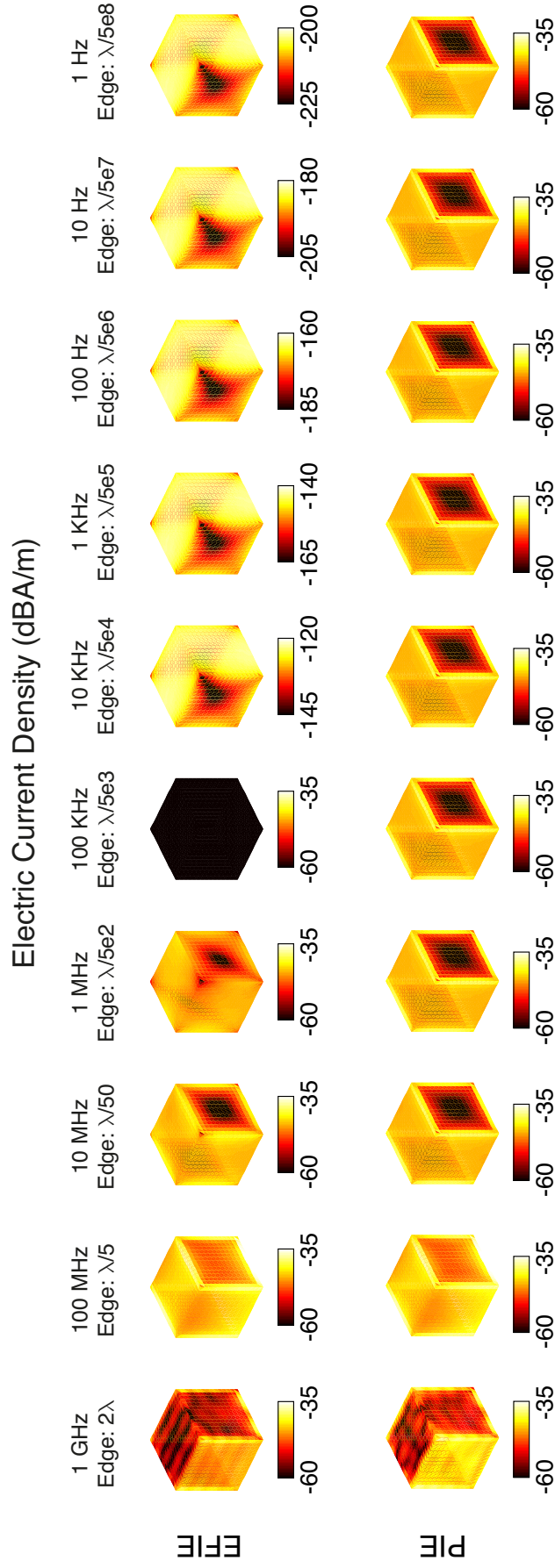
41

Figure 3.6: Surface current density distributions on a PEC cube with 0.6 m edges at different frequencies.
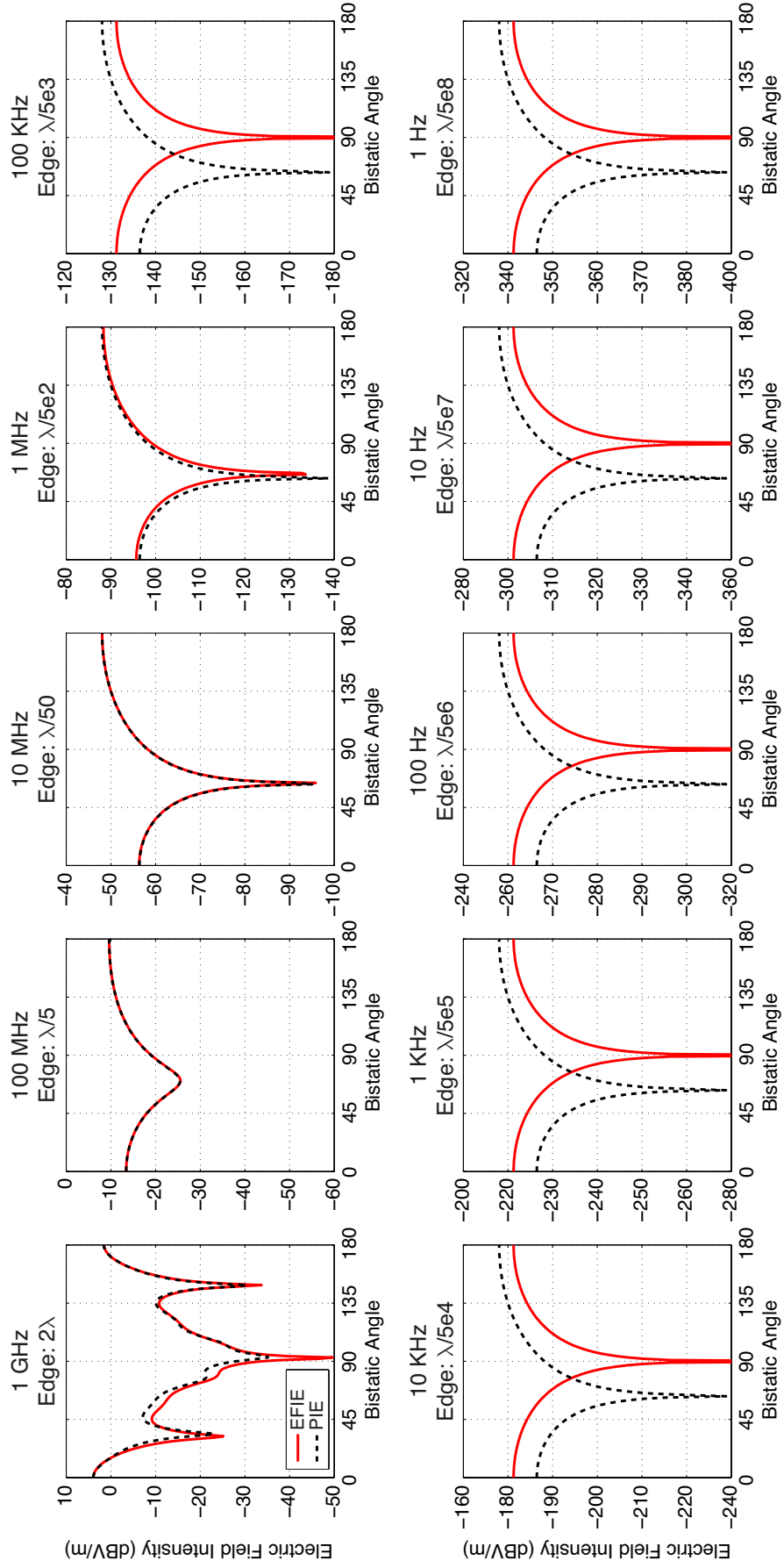
Figure 3.7: Far-zone electric field intensity scattered from a PEC cube with 0.6 m edges at different frequencies.
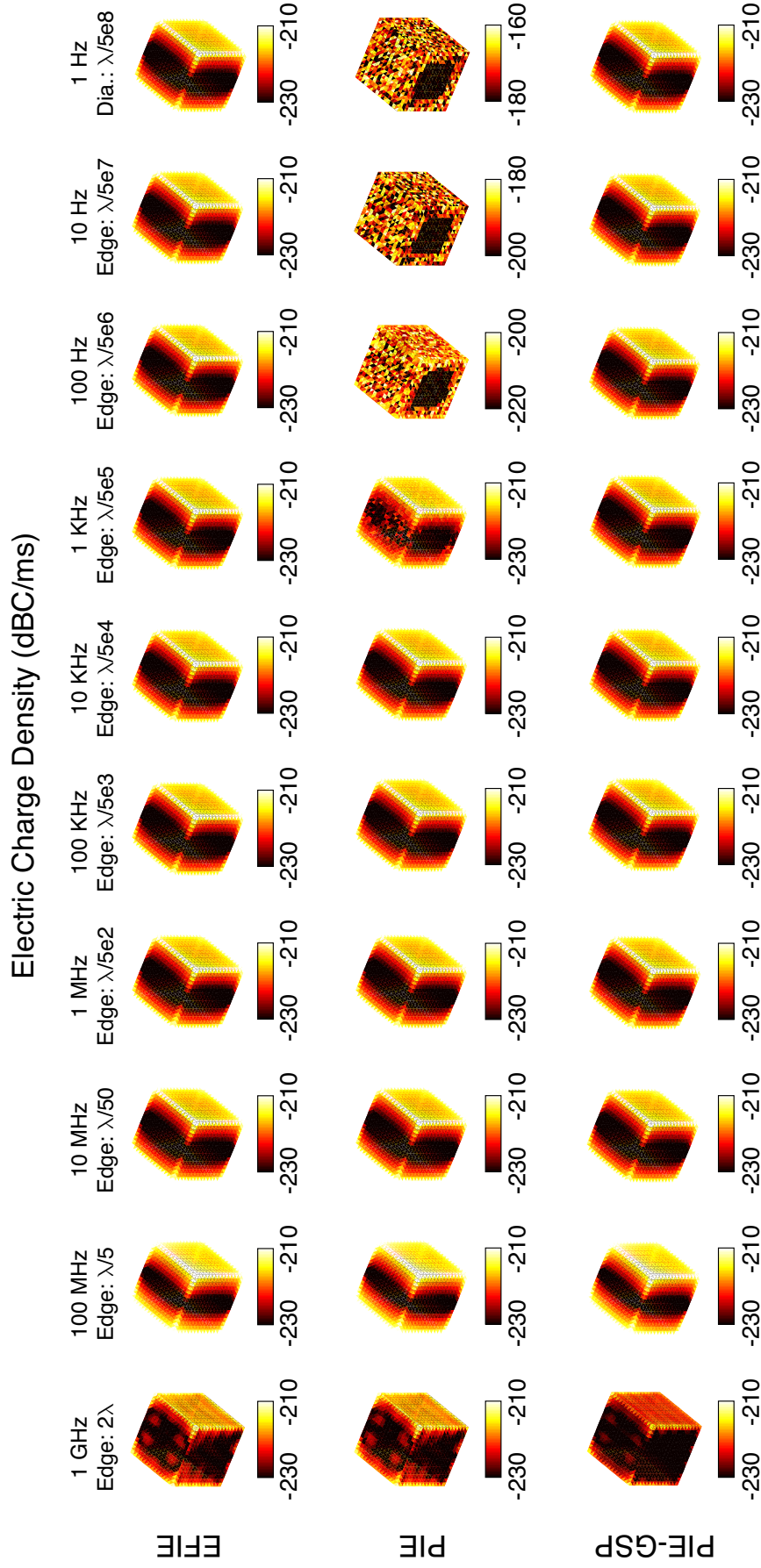
Electric Charge Density (dBC/ms)

Figure 3.8: Surface charge density distributions on a PEC cube with 0.6 m edges at different frequencies.
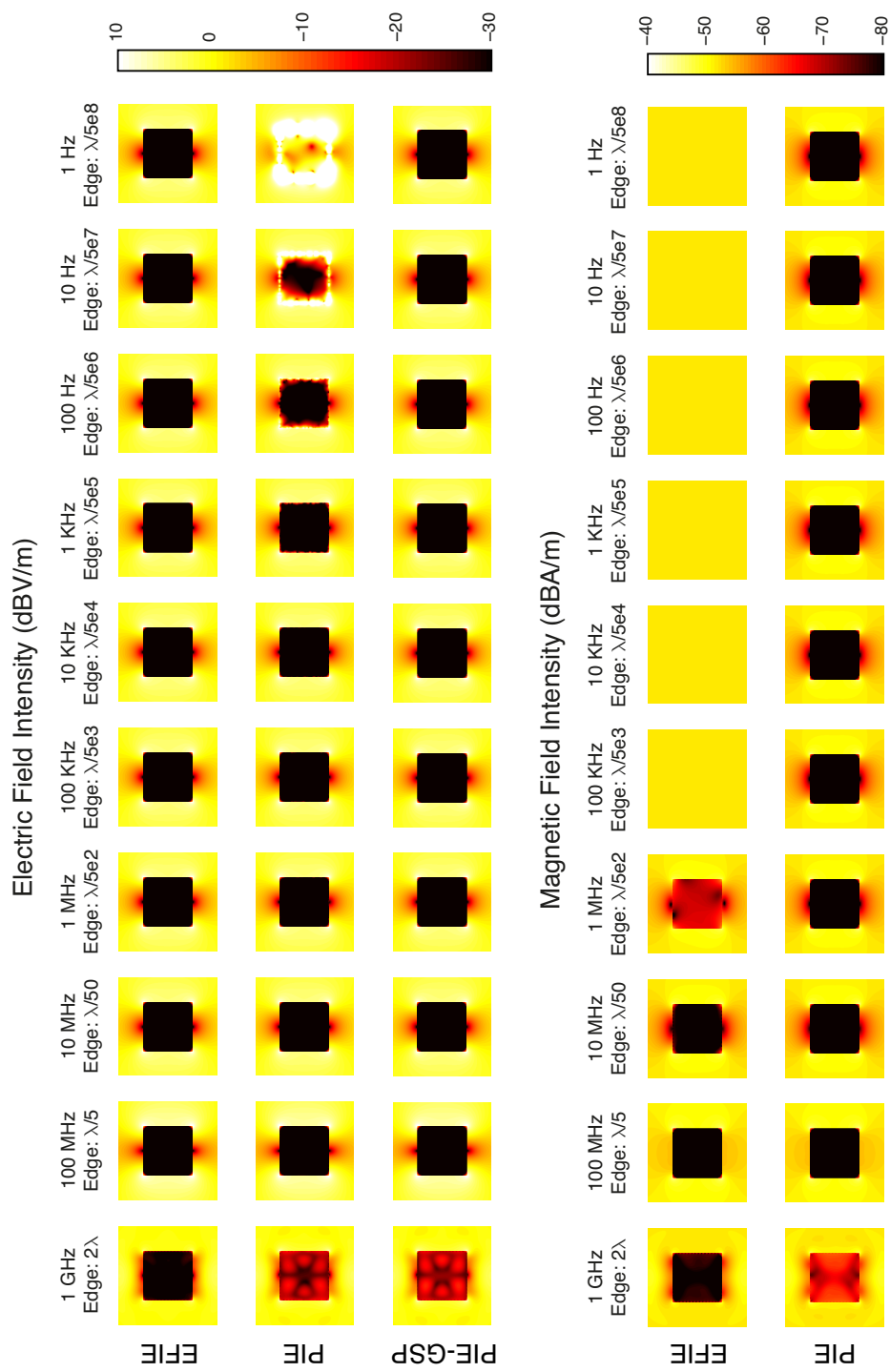
44

Figure 3.9: Near-zone electric and magnetic fields in the vicinity of a PEC cube with 0.6 m edges at different frequencies.
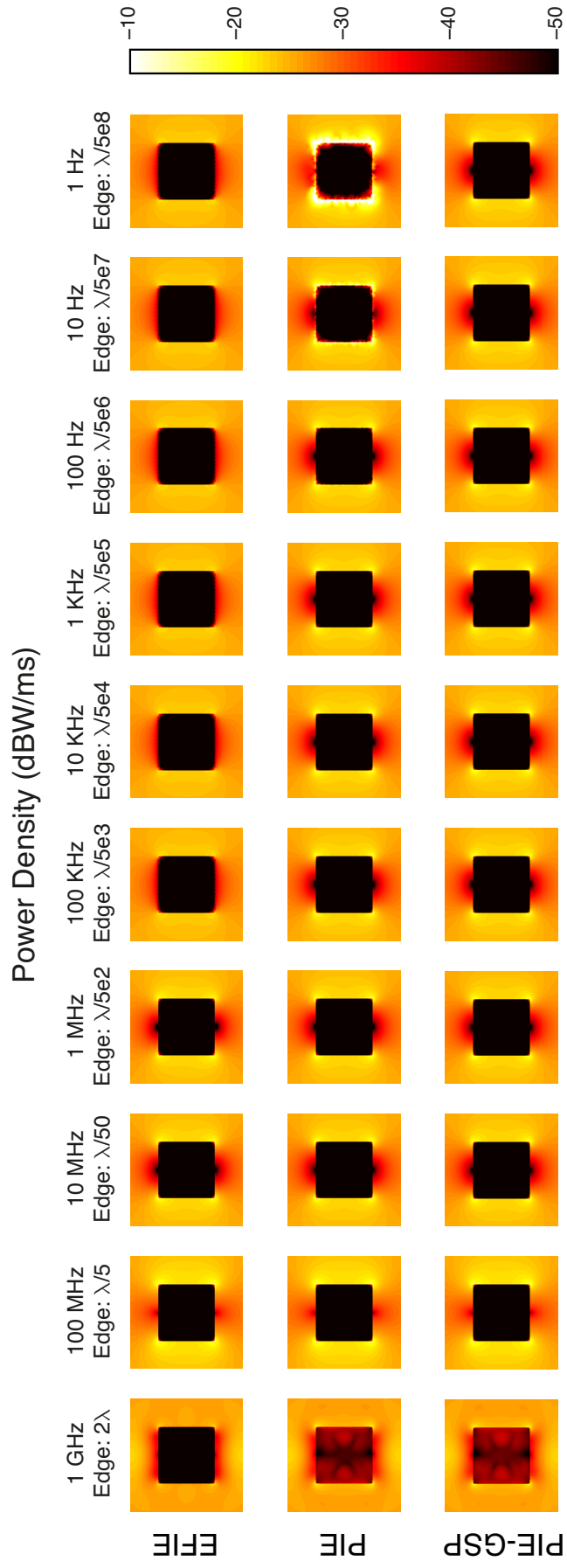
Figure 3.10: Near-zone power density distributions in the vicinity of a PEC cube with 0.6 m edges at different frequencies.
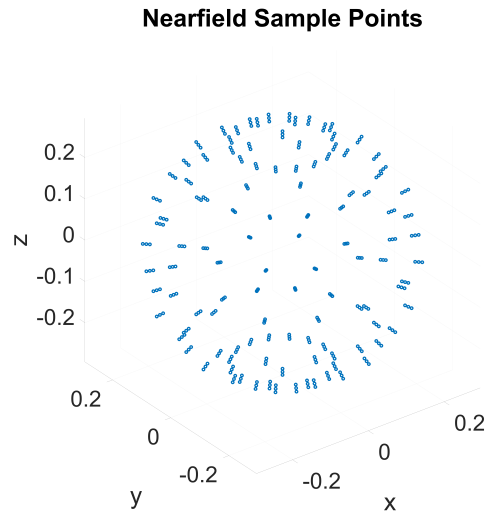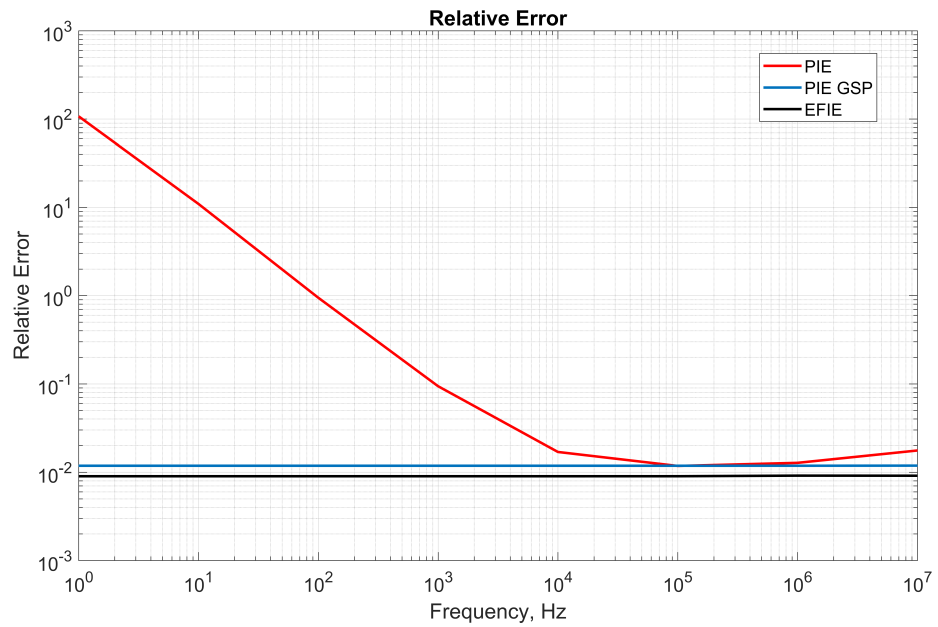
Figure 3.11: Near-field samples for Figure 3.12.

Figure 3.12: Relative error for the near-zone electric field intensity in the vicinity of the surface of a PEC sphere [23].

47

CHAPTER 4

LOW-FREQUENCY MLFMA

Ordinary MLFMA has its own low-frequency breakdown. Plane-wave expansion used in the diagonalization of the Green's function fails when the box sizes become small compared to wavelength. In order to use MLFMA for low-frequency problems, there are several solutions in the literature, such as using multipoles directly without diagonalization [25], approximate diagonalization [26, 27], deforming angular integration by introducing evanescent waves into plane-wave expansion [28, 29], and increasing the precision to 'postpone' the breakdown [30].

In this chapter, two different low-frequency MLFMA strategies are analyzed and implemented for PIEs [31, 32]. One of them is based on multipoles and the other is based on approximate diagonalization. Numerical results show the accuracy, stability, and efficiency of the implementations.

4.1   MLFMA Using Multipoles Directly

MLFMA using multipoles is based on the factorization of the Green's function without diagonalization. Green's function can be factorized as [8]

$$
g(\boldsymbol{r}, \boldsymbol{r}') = \frac{ik}{4\pi} \sum_{t_1=0}^{\infty} \sum_{u_1=-t_1}^{t_1} \sum_{t_2=0}^{\infty} \sum_{u_2=-t_2}^{t_2} \beta_{0,0,t_1,u_1}(k, \boldsymbol{r} - \boldsymbol{r}_C) \alpha_{t_1,u_1,t_2,u_2}(k, \boldsymbol{r}_{CC'})
$$
$$
\beta_{t_2,u_2,0,0}(k, \boldsymbol{r}_{C'} - \boldsymbol{r}'), \tag{4.1}
$$

where $\beta_{0,0,t_1,u_1}(k, \boldsymbol{r} - \boldsymbol{r}_C)$ is the multipole-to-monopole shift function, α_{t_1,u_1,t_2,u_2} $(k, \boldsymbol{r}_{CC'})$ is the multipole-to-multipole translation function, and $\beta_{t_2,u_2,0,0}(k, \boldsymbol{r}_{C'} - \boldsymbol{r}')$

is the monopole-to-multipole shift function. The coordinate variables $\boldsymbol{r}', \boldsymbol{r}_{C'}, \boldsymbol{r}_C, \boldsymbol{r}$ represent source location, aggregation location, translation location, and observation location, respectively. Basically, the factorization states that an interaction between a source and an observation point can be modeled as a series of operations involving monopole-to-multipole shift (aggregation) from $\boldsymbol{r}'$ to $\boldsymbol{r}_{C'}$, multipole-to-multipole translation from $\boldsymbol{r}_{C'}$ to $\boldsymbol{r}_C$, and multipole-to-monopole shift (disaggregation) from $\boldsymbol{r}_C$ to $\boldsymbol{r}$.

While (4.1) can be directly used in an FMM implementation, MLFMA implementations require additional multipole-to-multipole shift functions, i.e.,

$$\alpha_{t_1,u_1,t_2,u_2}(k, \boldsymbol{r}_{CC'}) = \sum_{t_3=0}^{\infty} \sum_{u_3=-t_3}^{t_3} \sum_{t_4=0}^{\infty} \sum_{u_4=-t_4}^{t_4} \beta_{t_1,u_1,t_3,u_3}(k, \boldsymbol{r}_{CD})\alpha_{t_3,u_3,t_4,u_4}(k, \boldsymbol{r}_{DD'})$$
$$\beta_{t_4,u_4,t_2,u_2}(k, \boldsymbol{r}_{D'C'}). \tag{4.2}$$

In other words, multipole-to-multipole translation between $\boldsymbol{r}_{C'}$ and $\boldsymbol{r}_C$ is equivalent to multipole-to-multipole shift (aggregation) from $\boldsymbol{r}_{C'}$ to $\boldsymbol{r}_{D'}$, multipole-to-multipole translation from $\boldsymbol{r}_{D'}$ to $\boldsymbol{r}_D$, and multipole-to-multipole shift (disaggregation) from $\boldsymbol{r}_D$ to $\boldsymbol{r}_C$, combined.

Without diagonalization, these multipole-to-multipole shift and translation functions are dense matrices. Therefore, factorization of the Green's function involves dense matrix multiplications in the implementation. Multipole-to-multipole translation function is defined as

$$\alpha_{t_1,u_1,t_2,u_2}(k, \boldsymbol{r}_{DD'}) = 4\pi \sum_{t_3=0}^{\infty} \sum_{u_3=-t_3}^{t_3} i^{t_1+t_3-t_2} \boldsymbol{\Psi}_{t_3,u_3}(k, \boldsymbol{r}_{DD'})G_{t_2,u_2,t_1,u_1,t_3,u_3}, \tag{4.3}$$

where

$$\boldsymbol{\Psi}_{t_3,u_3}(k, \boldsymbol{r}_{DD'}) = h_{t_3}^{(1)}(kr_{DD'})Y_{t_3,u_3}(\theta_{DD'}, \phi_{DD'}) \tag{4.4}$$

are wave functions, in which

$$Y_{t_3,u_3}(\theta_{DD'}, \phi_{DD'}) = \sqrt{\frac{(2t_3+1)(t_3-u_3)!}{4\pi(t_3+u_3)!}} P_{t_3}^{u_3}(\cos\theta_{DD'})e^{iu_3\phi_{DD'}} \tag{4.5}$$

are spherical harmonics and $P_{t_3}^{u_3}(\cos\theta_{DD'})$ is the associated Legendre function, and

$$G_{t_2,u_2,t_1,u_1,t_3,u_3} = \int d^2\hat{\boldsymbol{k}} Y_{t_2,u_2}(\theta_{DD'}, \phi_{DD'})Y_{t_1,u_1}^*(\theta_{DD'}, \phi_{DD'})$$
$$Y_{t_3,u_3}^*(\theta_{DD'}, \phi_{DD'}) \tag{4.6}$$

are the Gaunt coefficients. As most of the coefficients are zero, recursive relations to efficiently obtain these coefficients can be found in [8]. Multipole-to-multipole shift function is defined as

$$
\beta_{t_1,u_1,t_3,u_3}(k,\boldsymbol{r}_{CD}) = 4\pi \sum_{t_4=0}^{\infty} \sum_{u_4=-t_4}^{t_4} i^{t_1+t_4-t_3} \Re\{\boldsymbol{\Psi}_{t_4,u_4}(k,\boldsymbol{r}_{CD})\}
$$
$$
G_{t_3,u_3,t_1,u_1,t_4,u_4} \tag{4.7}
$$

in which

$$
\Re\{\boldsymbol{\Psi}_{t_4,u_4}(k,\boldsymbol{r}_{CD})\} = j_{t_4}(kr_{CD})Y_{t_4,u_4}(\theta_{CD},\phi_{CD}). \tag{4.8}
$$

Finally, multipole-to-monopole and monopole-to-multipole shift functions are

$$
\beta_{0,0,t_1,u_1}(k,\boldsymbol{r}) = \sqrt{4\pi}\, j_{t_1}(kr)Y_{t_1,u_1}(\theta,\phi) \tag{4.9}
$$
$$
\beta_{t_2,u_2,0,0}(k,\boldsymbol{r}) = \sqrt{4\pi}(-1)^{t_2+u_2} j_{t_2}(kr)Y_{t_2,u_2}(\theta,\phi). \tag{4.10}
$$

The factorization obtained in the above equations are exact, however, they include infinite summations. Summations should be truncated for practical usage, while the truncation numbers specify the accuracy of the implementation (controllable accuracy).

As derived in (2.37), (2.43), (2.39), and (2.40), matrix elements derived in PIEs can be written as

$$
\bar{\boldsymbol{Z}}_{11}[m,n] = \mu \int_{S_m} d\boldsymbol{r}\, \boldsymbol{t}_m^{\mathrm{RWG}}(\boldsymbol{r}) \cdot \int_{S_n} d\boldsymbol{r}'\, g(\boldsymbol{r},\boldsymbol{r}') \boldsymbol{b}_n^{\mathrm{RWG}}(\boldsymbol{r}')
$$
$$
\bar{\boldsymbol{Z}}_{12}[m,p] = \int_{S_m} d\boldsymbol{r}\, \nabla \cdot \boldsymbol{t}_m^{\mathrm{RWG}}(\boldsymbol{r}) \int_{S_p} d\boldsymbol{r}'\, g(\boldsymbol{r},\boldsymbol{r}') b_p^{\mathrm{PLS}}(\boldsymbol{r}')
$$
$$
\bar{\boldsymbol{Z}}_{21}[q,n] = \int_{S_q} d\boldsymbol{r}\, t_q^{\mathrm{PLS}}(\boldsymbol{r}) \int_{S_n} d\boldsymbol{r}'\, g(\boldsymbol{r},\boldsymbol{r}') \nabla' \cdot \boldsymbol{b}_n^{\mathrm{RWG}}(\boldsymbol{r}')
$$
$$
\bar{\boldsymbol{Z}}_{22}[q,p] = \omega^2 \epsilon \int_{S_q} d\boldsymbol{r}\, t_q^{\mathrm{PLS}}(\boldsymbol{r}) \int_{S_p} d\boldsymbol{r}'\, g(\boldsymbol{r},\boldsymbol{r}') b_p^{\mathrm{PLS}}(\boldsymbol{r}').
$$

Using (4.1), matrix elements can be re-written (if they are far-zone interactions) as

$$\bar{\boldsymbol{Z}}_{11}^{\text{far}}[m,n] = \frac{ik\mu}{4\pi} \sum_{t_1=0}^{\infty} \sum_{u_1=-t_1}^{t_1} \sum_{t_2=0}^{\infty} \sum_{u_2=-t_2}^{t_2} \boldsymbol{F}_{m,t_1,u_1}^{11}(\boldsymbol{r}_C,k)\alpha_{t_1,u_1,t_2,u_2}(k,\boldsymbol{r}_{CC'})$$

$$\cdot \boldsymbol{S}_{n,t_2,u_2}^{11}(\boldsymbol{r}_{C'},k) \tag{4.11}$$

$$\bar{\boldsymbol{Z}}_{12}^{\text{far}}[m,p] = \frac{ik}{4\pi} \sum_{t_1=0}^{\infty} \sum_{u_1=-t_1}^{t_1} \sum_{t_2=0}^{\infty} \sum_{u_2=-t_2}^{t_2} F_{m,t_1,u_1}^{12}(\boldsymbol{r}_C,k)\alpha_{t_1,u_1,t_2,u_2}(k,\boldsymbol{r}_{CC'})$$

$$S_{p,t_2,u_2}^{12}(\boldsymbol{r}_{C'},k) \tag{4.12}$$

$$\bar{\boldsymbol{Z}}_{21}^{\text{far}}[q,n] = \frac{ik}{4\pi} \sum_{t_1=0}^{\infty} \sum_{u_1=-t_1}^{t_1} \sum_{t_2=0}^{\infty} \sum_{u_2=-t_2}^{t_2} F_{q,t_1,u_1}^{21}(\boldsymbol{r}_C,k)\alpha_{t_1,u_1,t_2,u_2}(k,\boldsymbol{r}_{CC'})$$

$$S_{n,t_2,u_2}^{21}(\boldsymbol{r}_{C'},k) \tag{4.13}$$

$$\bar{\boldsymbol{Z}}_{22}^{\text{far}}[q,p] = \frac{ik}{4\pi} \sum_{t_1=0}^{\infty} \sum_{u_1=-t_1}^{t_1} \sum_{t_2=0}^{\infty} \sum_{u_2=-t_2}^{t_2} F_{q,t_1,u_1}^{22}(\boldsymbol{r}_C,k)\alpha_{t_1,u_1,t_2,u_2}(k,\boldsymbol{r}_{CC'})$$

$$S_{p,t_2,u_2}^{22}(\boldsymbol{r}_{C'},k), \tag{4.14}$$

where S and F (both vector and scalar) represent radiation and receiving patterns, respectively, and they can be obtained as

$$\boldsymbol{S}_{n,t_2,u_2}^{11}(\boldsymbol{r}_{C'},k) = \int_{S_n} d\boldsymbol{r}' \boldsymbol{b}_n^{\text{RWG}}(\boldsymbol{r}')\beta_{t_2,u_2,0,0}(k,\boldsymbol{r}_{C'}-\boldsymbol{r}') \tag{4.15}$$

$$\boldsymbol{F}_{m,t_1,u_1}^{11}(\boldsymbol{r}_C,k) = \int_{S_m} d\boldsymbol{r} \boldsymbol{t}_m^{\text{RWG}}(\boldsymbol{r})\beta_{0,0,t_1,u_1}(k,\boldsymbol{r}-\boldsymbol{r}_C) \tag{4.16}$$

$$S_{p,t_2,u_2}^{12}(\boldsymbol{r}_{C'},k) = \int_{S_n} d\boldsymbol{r}' b_p^{\text{PLS}}(\boldsymbol{r}')\beta_{t_2,u_2,0,0}(k,\boldsymbol{r}_{C'}-\boldsymbol{r}') \tag{4.17}$$

$$F_{m,t_1,u_1}^{12}(\boldsymbol{r}_C,k) = \int_{S_m} d\boldsymbol{r} \nabla \cdot \boldsymbol{t}_m^{\text{RWG}}(\boldsymbol{r})\beta_{0,0,t_1,u_1}(k,\boldsymbol{r}-\boldsymbol{r}_C) \tag{4.18}$$

$$S_{n,t_2,u_2}^{21}(\boldsymbol{r}_{C'},k) = \int_{S_n} d\boldsymbol{r}' \nabla' \cdot \boldsymbol{b}_n^{\text{RWG}}(\boldsymbol{r}')\beta_{t_2,u_2,0,0}(k,\boldsymbol{r}_{C'}-\boldsymbol{r}') \tag{4.19}$$

$$F_{q,t_1,u_1}^{21}(\boldsymbol{r}_C,k) = \int_{S_m} d\boldsymbol{r} t_q^{\text{PLS}}(\boldsymbol{r})\beta_{0,0,t_1,u_1}(k,\boldsymbol{r}-\boldsymbol{r}_C) \tag{4.20}$$

$$S_{p,t_2,u_2}^{22}(\boldsymbol{r}_{C'},k) = \int_{S_n} d\boldsymbol{r}' b_p^{\text{PLS}}(\boldsymbol{r}')\beta_{t_2,u_2,0,0}(k,\boldsymbol{r}_{C'}-\boldsymbol{r}') \tag{4.21}$$

$$F_{q,t_1,u_1}^{22}(\boldsymbol{r}_C,k) = \int_{S_m} d\boldsymbol{r} t_q^{\text{PLS}}(\boldsymbol{r})\beta_{0,0,t_1,u_1}(k,\boldsymbol{r}-\boldsymbol{r}_C). \tag{4.22}$$

In order to calculate far-field interactions in a group-by-group manner, as described in Chapter 1, aggregation-translation-disaggregation procedures should be implemented. For that purpose, we first need to aggregate all radiated fields inside the lowest level

boxes to the box centers as

$$[\boldsymbol{s}_C^{11,x}\boldsymbol{s}_C^{11,y}\boldsymbol{s}_C^{11,z}]_{M_1\times 3} = \sum_{n\in C}\boldsymbol{x}[n][\boldsymbol{s}_n^{11,x}\boldsymbol{s}_n^{11,y}\boldsymbol{s}_n^{11,z}]_{M_1\times 3} \tag{4.23}$$

$$[\boldsymbol{s}_C^{12}]_{M_1\times 1} = \sum_{p\in C}\boldsymbol{x}[N+p][\boldsymbol{s}_p^{12}]_{M_1\times 1} \tag{4.24}$$

$$[\boldsymbol{s}_C^{21}]_{M_1\times 1} = \sum_{n\in C}\boldsymbol{x}[n][\boldsymbol{s}_n^{21}]_{M_1\times 1} \tag{4.25}$$

$$[\boldsymbol{s}_C^{22}]_{M_1\times 1} = \sum_{p\in C}\boldsymbol{x}[N+p][\boldsymbol{s}_p^{22}]_{M_1\times 1}, \tag{4.26}$$

where $\boldsymbol{x}$ is a coefficient vector containing $N+P$ elements provided by the iterative solver, $\boldsymbol{s}_n^{11}$ and $\boldsymbol{s}_n^{21}$ are vectors containing the radiation patterns of the nth RWG function, and $\boldsymbol{s}_p^{12}$ and $\boldsymbol{s}_p^{22}$ are vectors containing the radiation patterns of the pth pulse function. In the above, C represents a lowest level box and M_1 represents the number of multipoles at the lowest level.

For a multilevel implementation, we have

$$[\boldsymbol{s}_C^{11,x}\boldsymbol{s}_C^{11,y}\boldsymbol{s}_C^{11,z}]_{M_l\times 3} = \sum_{C'\in C}[\bar{\boldsymbol{\beta}}_{C'C}]_{M_l\times M_{l-1}}\cdot[\boldsymbol{s}_{C'}^{11,x}\boldsymbol{s}_{C'}^{11,y}\boldsymbol{s}_{C'}^{11,z}]_{M_{l-1}\times 3} \tag{4.27}$$

$$[\boldsymbol{s}_C^{12}]_{M_l\times 1} = \sum_{C'\in C}[\bar{\boldsymbol{\beta}}_{C'C}]_{M_l\times M_{l-1}}\cdot[\boldsymbol{s}_{C'}^{12}]_{M_{l-1}\times 1} \tag{4.28}$$

$$[\boldsymbol{s}_C^{21}]_{M_l\times 1} = \sum_{C'\in C}[\bar{\boldsymbol{\beta}}_{C'C}]_{M_l\times M_{l-1}}\cdot[\boldsymbol{s}_{C'}^{21}]_{M_{l-1}\times 1} \tag{4.29}$$

$$[\boldsymbol{s}_C^{22}]_{M_l\times 1} = \sum_{C'\in C}[\bar{\boldsymbol{\beta}}_{C'C}]_{M_l\times M_{l-1}}\cdot[\boldsymbol{s}_{C'}^{22}]_{M_{l-1}\times 1}, \tag{4.30}$$

where $[\bar{\boldsymbol{\beta}}_{C'C}]_{M_l\times M_{l-1}}$ is a dense multipole-to-multipole shift matrix from the center of box C' to the center of box C and a truncation converter (up) from M_{l-1} to M_l. In this case, C is a parent box of C'.

We translate the aggregated radiation patterns into incoming patterns as

$$[\boldsymbol{g}_C^{11,x}\boldsymbol{g}_C^{11,y}\boldsymbol{g}_C^{11,z}]_{M_l\times 3} = \sum_{C'\in\mathcal{F}\{C\}}[\bar{\boldsymbol{\alpha}}_{C'C}]_{M_l\times M_l}\cdot[\boldsymbol{s}_{C'}^{11,x}\boldsymbol{s}_{C'}^{11,y}\boldsymbol{s}_{C'}^{11,z}]_{M_l\times 3} \tag{4.31}$$

$$[\boldsymbol{g}_C^{12}]_{M_l\times 1} = \sum_{C'\in\mathcal{F}\{C\}}[\bar{\boldsymbol{\alpha}}_{C'C}]_{M_l\times M_l}\cdot[\boldsymbol{s}_{C'}^{12}]_{M_l\times 1} \tag{4.32}$$

$$[\boldsymbol{g}_C^{21}]_{M_l\times 1} = \sum_{C'\in\mathcal{F}\{C\}}[\bar{\boldsymbol{\alpha}}_{C'C}]_{M_l\times M_l}\cdot[\boldsymbol{s}_{C'}^{21}]_{M_l\times 1} \tag{4.33}$$

$$[\boldsymbol{g}_C^{22}]_{M_l\times 1} = \sum_{C'\in\mathcal{F}\{C\}}[\bar{\boldsymbol{\alpha}}_{C'C}]_{M_l\times M_l}\cdot[\boldsymbol{s}_{C'}^{22}]_{M_l\times 1}, \tag{4.34}$$

where $[\bar{\boldsymbol{\alpha}}_{C'C}]_{M_l \times M_l}$ is a square matrix containing the multipole-to-multipole translations from the center of box C' to the center of box C, and $\mathcal{F}\{C\}$ represents far-zone boxes for box C.

After the translation process, we disaggregate the incoming fields to the lower level boxes. If the implementation is multilevel, we have

$$
\begin{aligned}
[\boldsymbol{g}_C^{+11,x} \boldsymbol{g}_C^{+11,y} \boldsymbol{g}_C^{+11,z}]_{M_l \times 3} =& [\boldsymbol{g}_C^{11,x} \boldsymbol{g}_C^{11,y} \boldsymbol{g}_C^{11,z}]_{M_l \times 3} \\
&+ [\bar{\boldsymbol{\beta}}_{C'C}]_{M_l \times M_{l+1}} \cdot [\boldsymbol{g}_{C'}^{11,x} \boldsymbol{g}_{C'}^{11,y} \boldsymbol{g}_{C'}^{11,z}]_{M_{l+1} \times 3}
\end{aligned}
\tag{4.35}
$$

$$
[\boldsymbol{g}_C^{+12}]_{M_l \times 1} = [\boldsymbol{g}_C^{12}]_{M_l \times 1} + [\bar{\boldsymbol{\beta}}_{C'C}]_{M_l \times M_{l+1}} \cdot [\boldsymbol{g}_{C'}^{12}]_{M_{l+1} \times 1}
\tag{4.36}
$$

$$
[\boldsymbol{g}_C^{+21}]_{M_l \times 1} = [\boldsymbol{g}_C^{21}]_{M_l \times 1} + [\bar{\boldsymbol{\beta}}_{C'C}]_{M_l \times M_{l+1}} \cdot [\boldsymbol{g}_{C'}^{21}]_{M_{l+1} \times 1}
\tag{4.37}
$$

$$
[\boldsymbol{g}_C^{+22}]_{M_l \times 1} = [\boldsymbol{g}_C^{22}]_{M_l \times 1} + [\bar{\boldsymbol{\beta}}_{C'C}]_{M_l \times M_{l+1}} \cdot [\boldsymbol{g}_{C'}^{22}]_{M_{l+1} \times 1},
\tag{4.38}
$$

where $[\bar{\boldsymbol{\beta}}_{C'C}]_{M_l \times M_{l+1}}$ is a dense multipole-to-multipole shift matrix from the center of box C' to the center of box C and a truncation (down) converter from M_{l+1} to M_l.

Finally, at the lowest level, we complete the matrix-vector multiplication cycle as

$$
\begin{aligned}
\sum_{n=1}^{N} \bar{\boldsymbol{Z}}_{11}^{\text{far}}[m,n]\boldsymbol{x}[n] \approx& \frac{ik\mu}{4\pi} \big\{ [\boldsymbol{f}_m^{11,x}]_{1 \times M_1} \cdot [\boldsymbol{g}_C^{+11,x}]_{M_1 \times 1} \\
&+ [\boldsymbol{f}_m^{11,y}]_{1 \times M_1} \cdot [\boldsymbol{g}_C^{+11,y}]_{M_1 \times 1} \\
&+ [\boldsymbol{f}_m^{11,z}]_{1 \times M_1} \cdot [\boldsymbol{g}_C^{+11,z}]_{M_1 \times 1} \big\}
\end{aligned}
\tag{4.39}
$$

$$
\sum_{p=1}^{P} \bar{\boldsymbol{Z}}_{12}^{\text{far}}[m,p]\boldsymbol{x}[N+p] \approx \big\{ [\boldsymbol{f}_m^{12}]_{1 \times M_1} \cdot [\boldsymbol{g}_C^{+12}]_{M_1 \times 1} \big\}
\tag{4.40}
$$

$$
\sum_{n=1}^{N} \bar{\boldsymbol{Z}}_{21}^{\text{far}}[q,n]\boldsymbol{x}[n] \approx \big\{ [\boldsymbol{f}_q^{21}]_{1 \times M_1} \cdot [\boldsymbol{g}_C^{+21}]_{M_1 \times 1} \big\}
\tag{4.41}
$$

$$
\sum_{p=1}^{P} \bar{\boldsymbol{Z}}_{22}^{\text{far}}[q,p]\boldsymbol{x}[N+p] \approx \big\{ [\boldsymbol{f}_q^{22}]_{1 \times M_1} \cdot [\boldsymbol{g}_C^{+22}]_{M_1 \times 1} \big\},
\tag{4.42}
$$

where $\boldsymbol{f}_m^{11}$ and $\boldsymbol{f}_m^{12}$ are vectors containing the receiving patterns of the mth RWG function, while $\boldsymbol{f}_q^{21}$ and $\boldsymbol{f}_q^{22}$ are vectors containing the receiving patterns of the qth pulse function. In the above, we note that $m \in C$ and $q \in C$.

4.2 Approximate Diagonalization MLFMA

One of the main reasons that we cannot use the standard diagonalization in MLFMA at low frequencies is that the plane-wave expansion that is the core of the diagonalization is not valid when the box size becomes small compared to the wavelength. In AD-MLFMA, scaled spherical and plane waves are used for stable diagonalization of the Green's function. In low-frequency regime, shift operators are converted into scaled complex exponentials, reducing the computational cost just as in the high frequency regime (ordinary MLFMA). However, in this method, there are contradictory requirements that makes the accuracy limited. In this context, (1.49) and (1.50) can be written as

$$\beta^s(\boldsymbol{k}, \boldsymbol{r}) = \sum_{t=0}^{\infty} i^t (2t+1) j_t(kr) s^{-t} P_{t''}(\hat{\boldsymbol{k}} \cdot \hat{\boldsymbol{r}}) \tag{4.43}$$

$$\alpha^s(\boldsymbol{k}, \boldsymbol{r}) = \sum_{t=0}^{\infty} (is)^t (2t+1) h_t^{(1)}(kr) P_{t''}(\hat{\boldsymbol{k}} \cdot \hat{\boldsymbol{r}}), \tag{4.44}$$

where $P_{t''}$ represents Legendre polynomials and s represents the scaling factor. When $kr \ll s$ and $kr \ll 1$, (4.43) can be written as

$$\beta^s(\boldsymbol{k}, \boldsymbol{r}) \approx \sum_{t=0}^{\infty} i^t (2t+1) j_t(kr/s) P_{t''}(\hat{\boldsymbol{k}} \cdot \hat{\boldsymbol{r}}) = e^{i\boldsymbol{k} \cdot \boldsymbol{r}/s}. \tag{4.45}$$

Therefore, (1.48) becomes

$$g(\boldsymbol{r}_i, \boldsymbol{r}_j) = \frac{ik}{(4\pi)^2} \int d^2\hat{\boldsymbol{k}} e^{i\boldsymbol{k} \cdot \boldsymbol{r}_{iIJj}/s} \alpha^s(\boldsymbol{k}, \boldsymbol{r}_{IJ}). \tag{4.46}$$

For an accurate factorization, translation vector should be much larger than the shift vector, i.e. $kr_{\text{shift}} \ll s \approx kr_{\text{trans}}$, which limits the accuracy of the approximate diagonalization. However, approximate diagonalization is a stable method and it can be applied to arbitrarily low-frequency problems, while it is easy to implement using existing MLFMA solvers.

4.3 Numerical Results

First, in order to show the effect of truncation number on the accuracy of the multipole-based factorization of the Green's function, possible shift and translation scenarios

for different-sized objects are considered. In Figure 4.1, one-level interactions that involve monopole-to-multipole aggregation, multipole-to-multipole translation, and multipole-to-monopole disaggregation, are compared with the Green's function itself. For each translation size, different shift sizes are considered in order to simulate possible interactions in a real problem. In the figures, the diagonal line represents the limit case, i.e., results above this line are disregarded because they never occur. The relative error is calculated as

$$\text{RE} = \frac{\left| g_{\text{factorized}} - g_{\text{analytical}} \right|}{\left| g_{\text{analytical}} \right|},$$

where $g_{\text{factorized}}$ is obtained by using (4.1) for different truncation numbers, i.e., 3, 5, and 7. As the truncation number increases, the accuracy improves, showing the controllable-accuracy of the method. Note that, as the translation vector size and the shift vector size become close to each other, the relative error increases, as expected.

Similarly, in Figure 4.2, two-level interactions are analyzed. These interactions involve, monopole-to-multipole aggregation, multipole-to-multipole aggregation, multipole-to-multipole translation, multipole-to-multipole disaggregation, and multipole-to-monopole disaggregation. Again, it can be seen that the accuracy is controllable by using the truncation number, and the overall accuracy is high, even for the cases where the truncation number is only three.

In Figure 4.3, we present solutions of a scattering problem involving a PEC sphere discretized by using different mesh sizes. The problem is solved via MLFMA using multipoles with six levels, and the results are compared with analytical solutions. As the zoomed figure shows, the accuracy is very good. The relative errors in the far-zone scattered field values while analytical solution taken as a reference, are 1.54%, 1.27%, and 1.14% for 20 mm, 15 mm, and 10 mm mesh sizes, respectively.

Figure 4.4 shows surface current densities induced on a PEC sphere discretized with 4080 RWG functions and 2720 triangle patches. Solutions are obtained by using MoM, AD-FMM, and LF-FMM (multipole based) at different frequencies. All solutions use PIEs for formulation. Taking MoM as a reference, FMM results are accurate and consistent with each other. Figure 4.5 shows far-zone scattered electric fields, including Mie series solutions, obtained for different discretization sizes. In order to see the differences clearly, Figure 4.6 presents the same results with a smaller dynamic

range. In the plots, mesh convergence can be seen clearly.

Figures 4.7, 4.8, and 4.9 show results for a cube with 0.6 m edges. In Figure 4.7, 4050 RWG functions and 2700 triangular patches are used for the discretization. Solutions are obtained by using MoM, AD-FMM, and LF-FMM formulated with PIEs at different frequencies. Consistency among different methods is clearly seen in surface current densities. Figure 4.8 shows far-zone scattered electric fields for different mesh sizes. In addition, Figure 4.9 presents the mesh convergence to demonstrate the stability.

As mentioned in Chapter 1, MFIE fails when the problem involves open surfaces, while one of the main advantages of PIEs is their applicability to open-surface problems. For that purpose, Figures 4.10, 4.11, and 4.12 present a scattering problem involving a square patch with 0.6 m edges. Figure 4.10 presents surface current densities induced on the patch obtained by using MoM, AD-FMM, and LF-FMM formulated with PIEs. Patch is discretized by using triangles with 5 cm edges. At different frequencies, all methods provide consistent results. Figure 4.11 shows the far-zone electric field intensity scattered from the patch, while Figure 4.12 shows zoomed plots to demonstrate mesh convergence.

Figure 4.13 includes far-zone scattered electric field results for a PEC patch excited with plane waves at two different frequencies. The scattering problems are solved with AD-MLFMA using different number of levels in order to show the capability of the implementation. It can be seen that increasing the number of levels, hence the efficiency, does not deteriorate the accuracy significantly.

In Figure 4.14, sphere problems involving different mesh sizes are solved by using PIEs and six-level AD-MLFMA. The radius of the sphere is again 0.3 m, while the frequency is fixed to 100 MHz. Mesh sizes vary from 20 mm to 6 mm ($\lambda/150$ to $\lambda/500$) and the number of unknowns changes from 6276+9414 to 71264+106896 (triangles+RWGs). At this fixed frequency, the diameter of the sphere is $\lambda/5$. All results are consistent with the Mie series solution.

Figure 4.15 shows scattering results for the PEC sphere of radius 0.3 m using AD-MLFMA with different numbers of levels. The frequency is now 1 MHz. While the

57

accuracy is preserved, the efficiency of the solver can be improved by increasing the number of levels.

For the same sphere problem, Figure 4.16 presents results obtained with MoM and four-level AD-MLFMA using different formulations. Relative errors with respect to the Mie series solutions show that the accuracy of the combination of PIEs and AD-MLFMA is the best. The errors can be listed as follows:

- EFIE MoM 4.71%

- CFIE MoM 1.03%

- MFIE AD-MLFMA 2.13%

- PIE AD-MLFMA 0.46%

Finally, Figures 4.17 and 4.18 show the processing times and the numbers of GMRES iterations (tolerance of 10^{-3}) for the same sphere at 100 MHz discretized with different numbers of unknowns. When the number of levels is fixed in AD-MLFMA, it can be seen that the processing time fits into an $\mathcal{O}(N)$ curve. In addition, although the number of unknowns is nearly 12 times increased, the required number of iterations remains almost constant. This clearly shows the effectiveness and the stability of the implementation based on PIEs and AD-MLFMA.
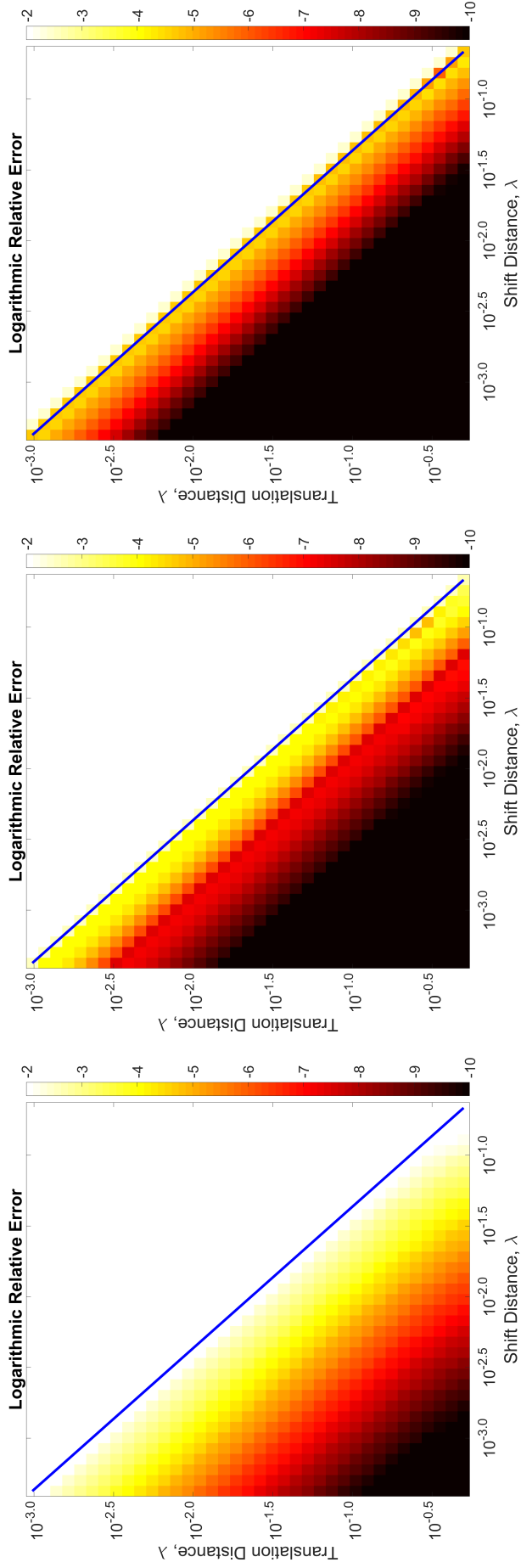
Figure 4.1: Relative errors in one-level factorization of the Green's function using multipoles with truncation numbers 3, 5, and 7, respectively (from left to right). The diagonal line is the limit case; above this line is never seen in the MLFMA implementation.
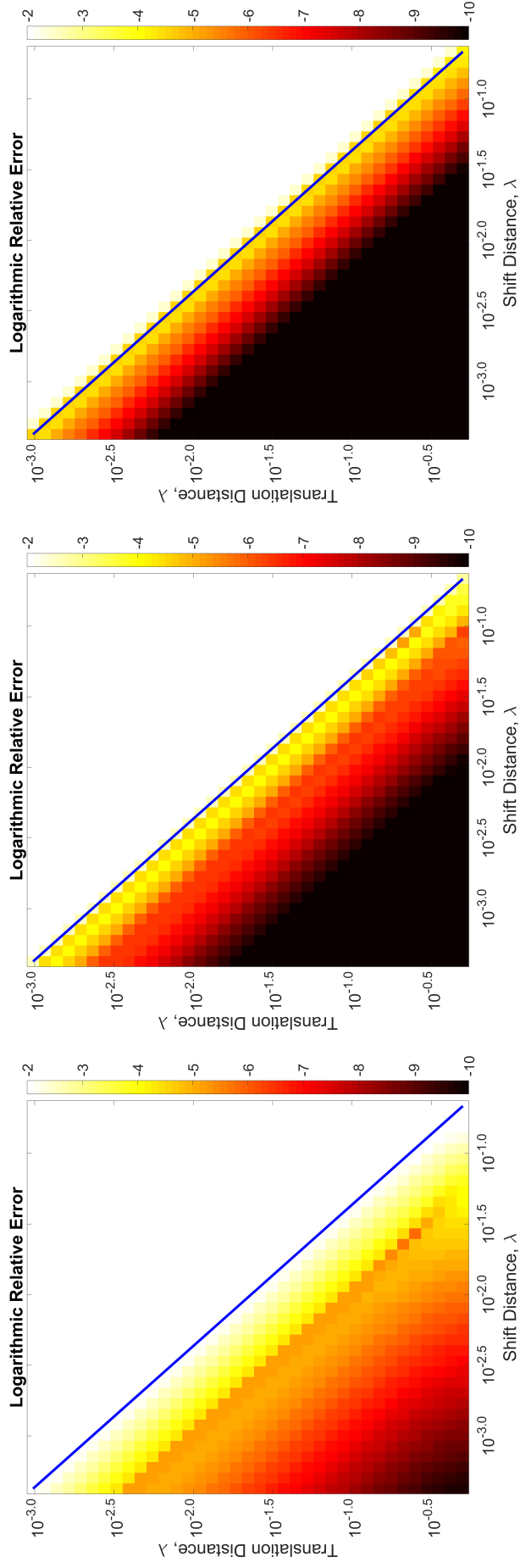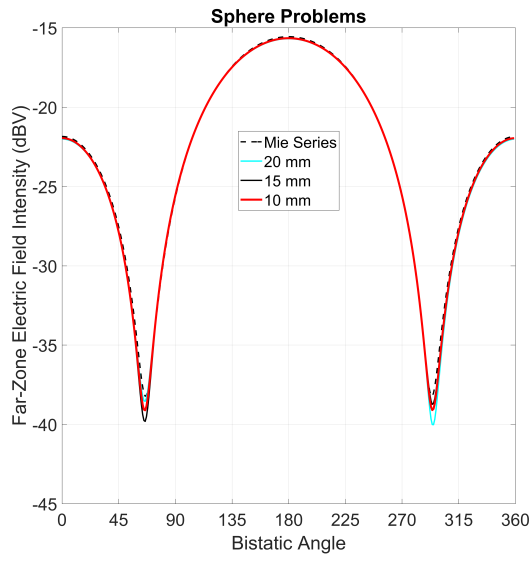
Figure 4.2: Relative errors in two-level factorization of the Green's function using multipoles with truncation numbers 3, 5, and 7, respectively (from left to right). The diagonal line is the limit case; above this line is never seen in the MLFMA implementation.
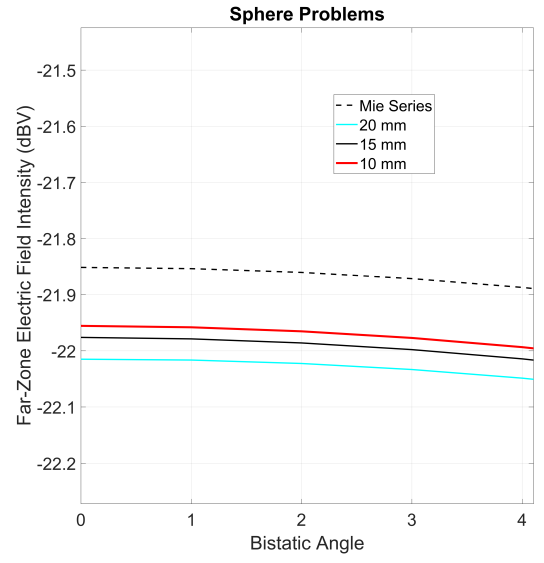
Figure 4.3: Far-zone electric field intensity scattered from a PEC sphere. Solutions via six-level MLFMA by using multipoles for different mesh sizes are shown. PIEs are used for the formulation.
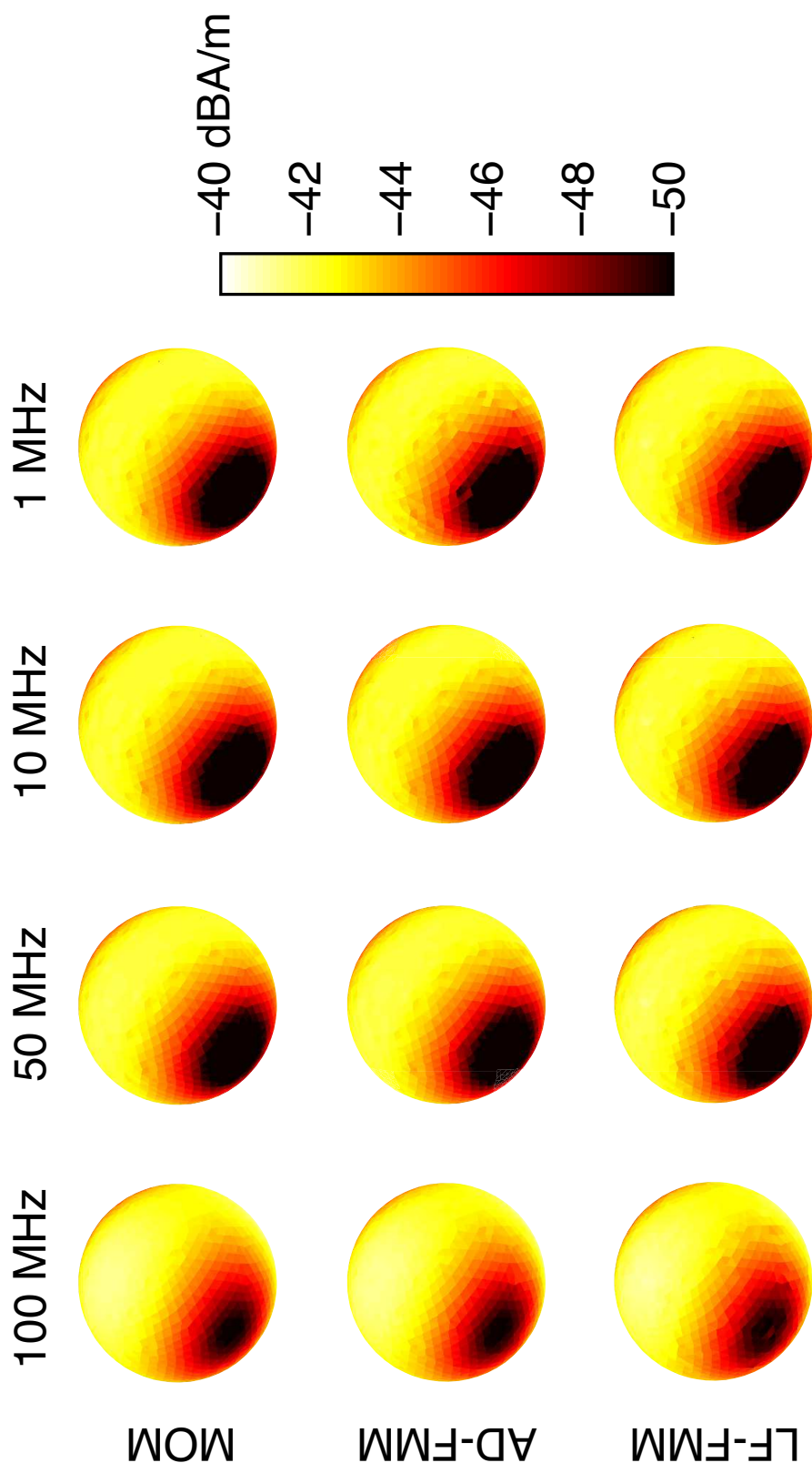
Figure 4.4: Surface current density induced on a PEC sphere of radius 0.3 m at different frequencies. The solutions are performed by using MoM, AD-FMM, and LF-FMM, all employing PIEs [32].
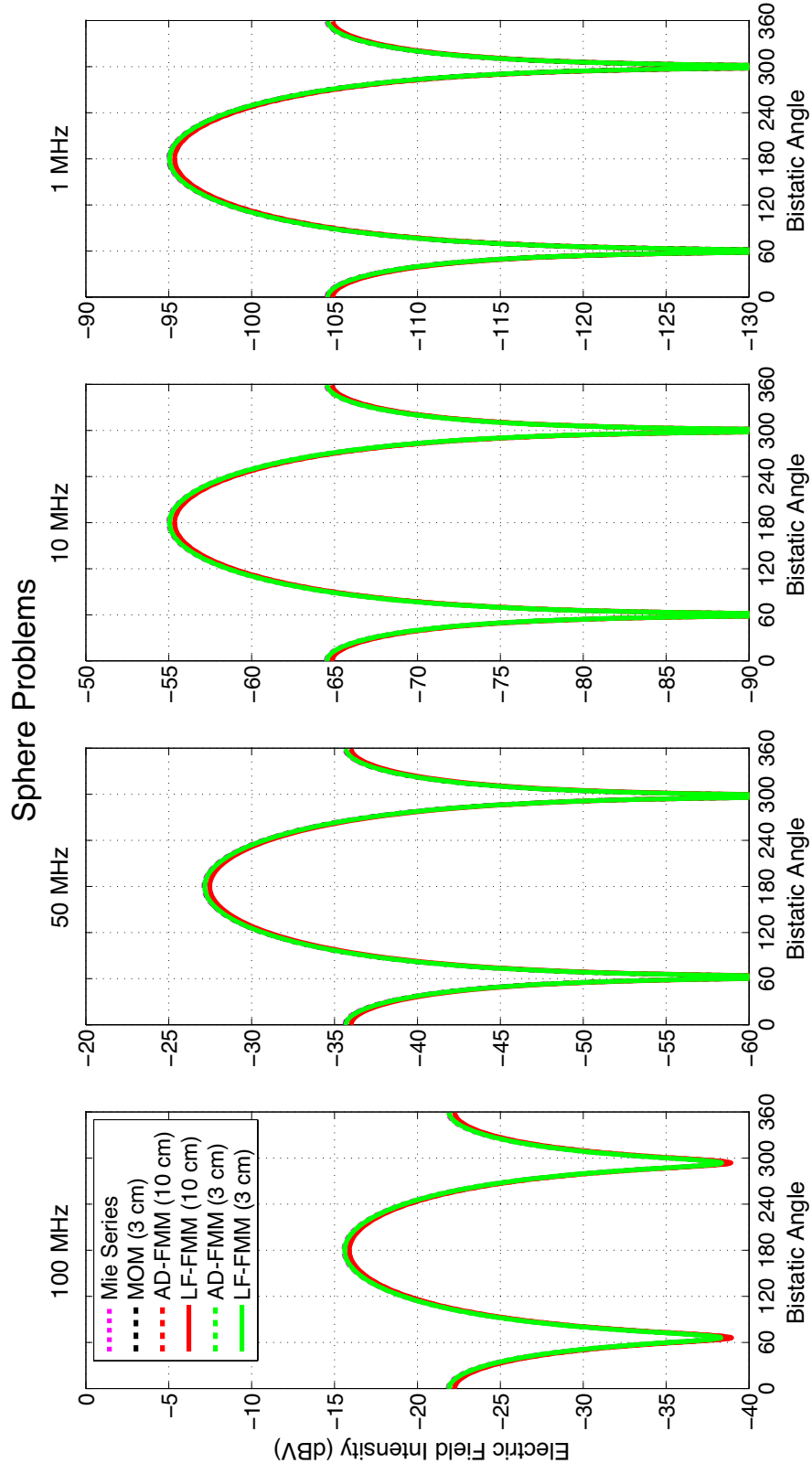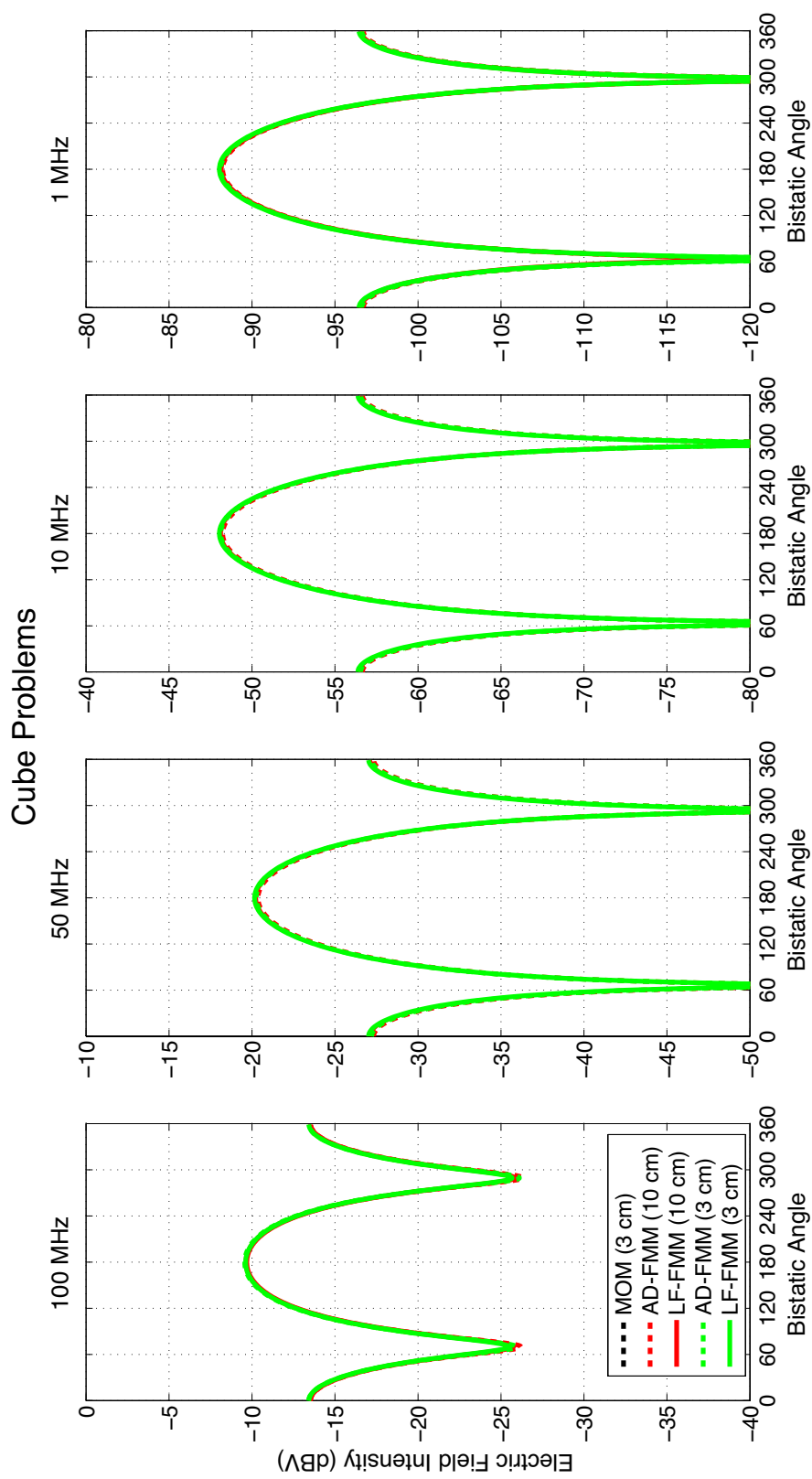
Figure 4.5: Far-zone electric field intensity scattered from a PEC sphere of 0.3 m at different frequencies. The solutions are performed by using MoM, AD-FMM, and LF-FMM, all employing PIEs, and via Mie series [32].

63
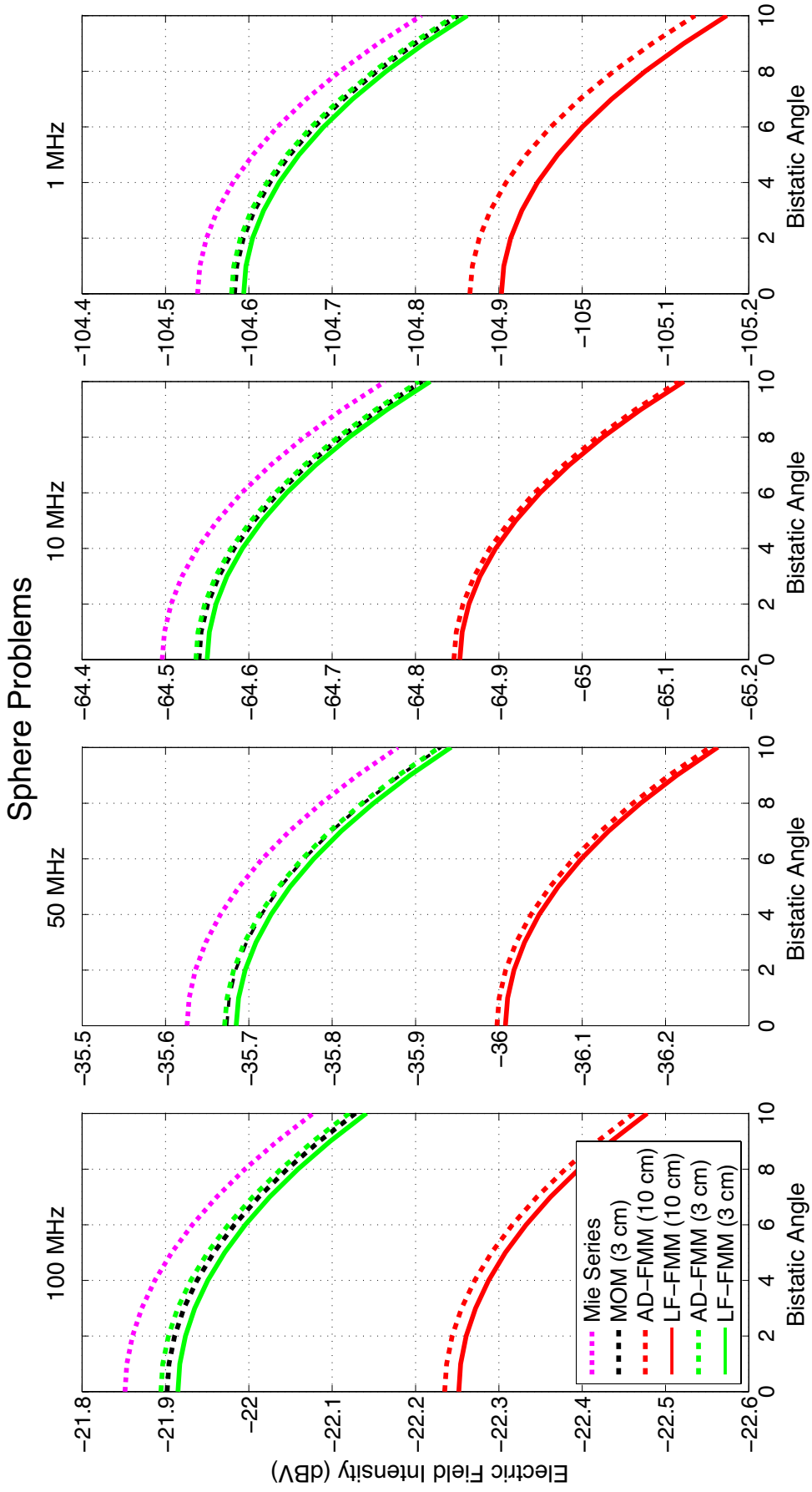
Figure 4.6: Zoomed versions of the plots in Figure 4.5.
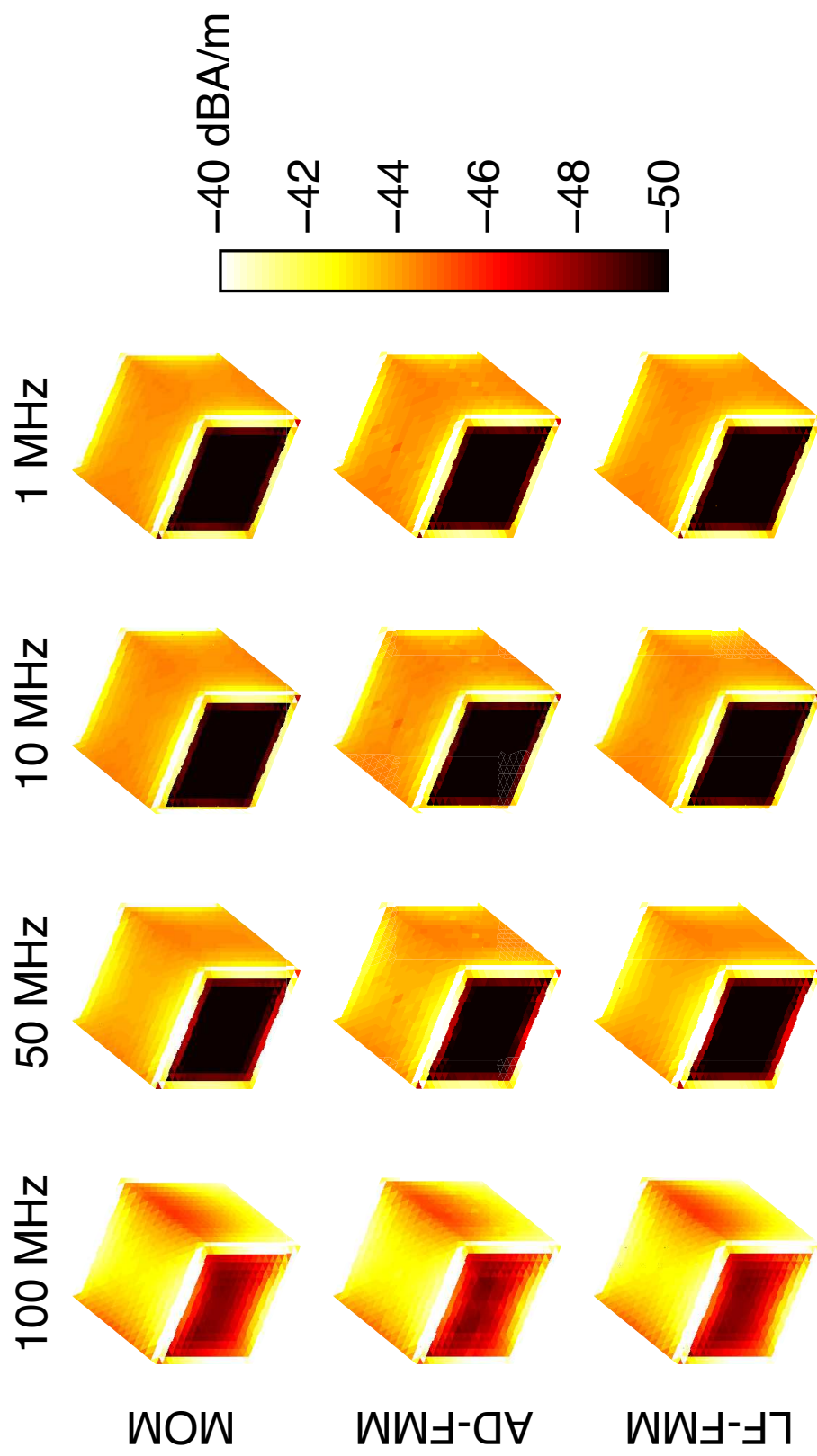
Figure 4.7: Surface current density induced on a PEC cube with 0.6 m edges at different frequencies. The solutions are performed by using MoM, AD-FMM, and LF-FMM, all employing PIEs [32].
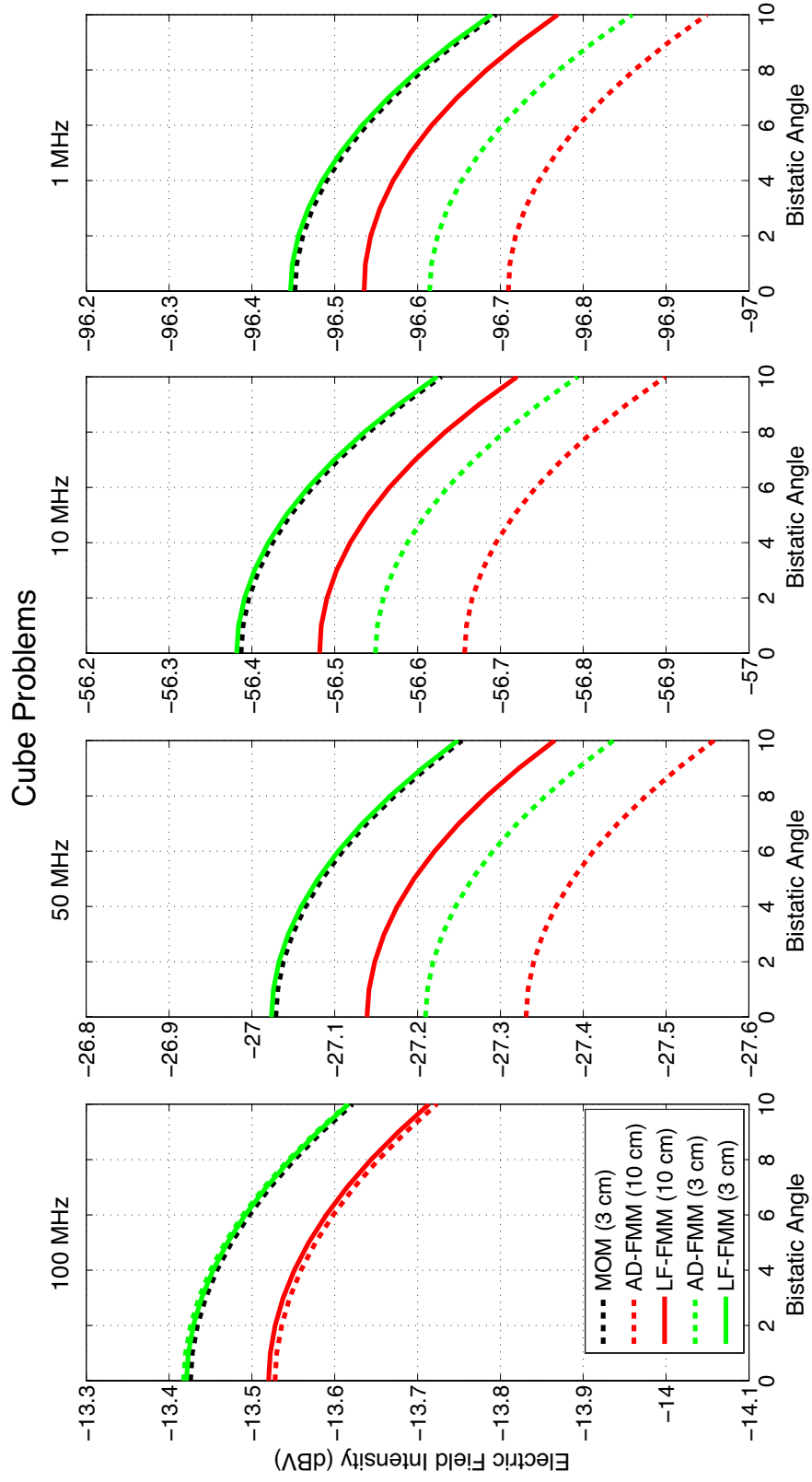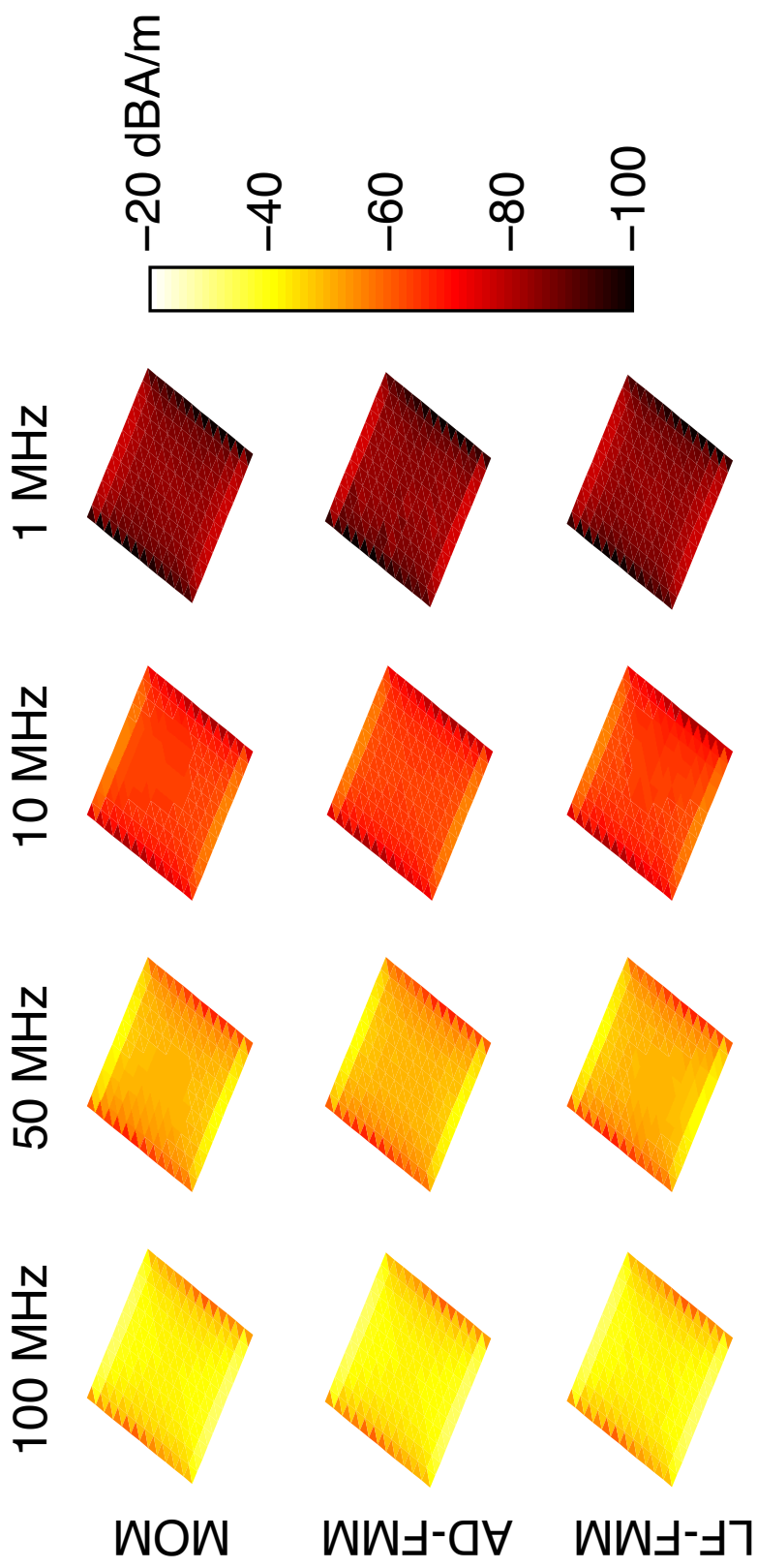
Cube Problems

Figure 4.8: Far-zone electric field intensity scattered from a PEC cube with 0.6 m edges at different frequencies. The solutions are performed by using MoM, AD-FMM, and LF-FMM, all employing PIEs [32].

66

Figure 4.9: Zoomed versions of the plots in Figure 4.8 [32].

Figure 4.10: Surface current density induced on a PEC patch with 0.6 m edges at different frequencies. The solutions are performed by using MoM, AD-FMM, and LF-FMM, all employing PIEs [32].
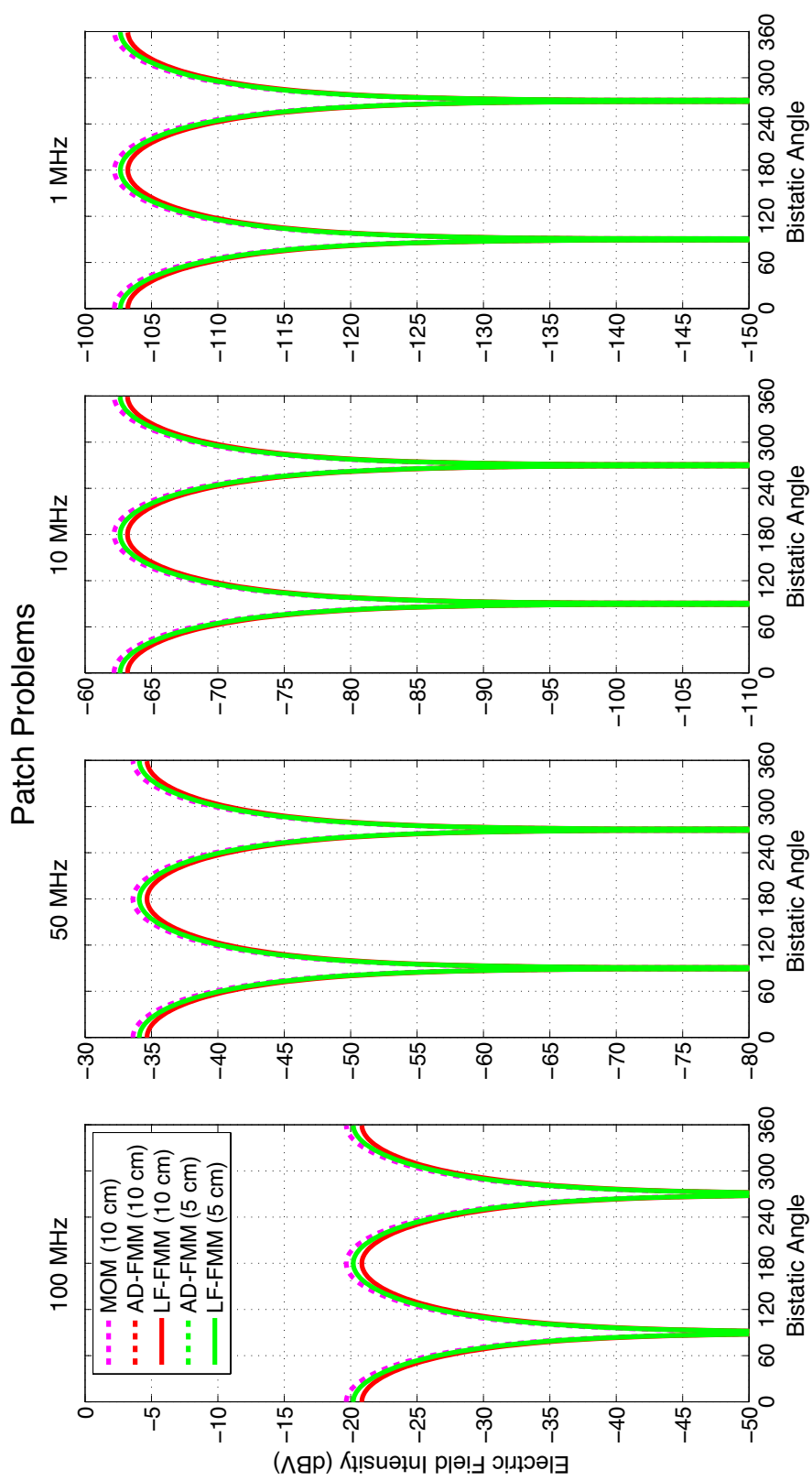
Figure 4.11: Far-zone electric field intensity scattered from a PEC patch with 0.6 m edges at different frequencies. The solutions are performed by using MoM, AD-FMM, and LF-FMM, all employing PIEs [32].
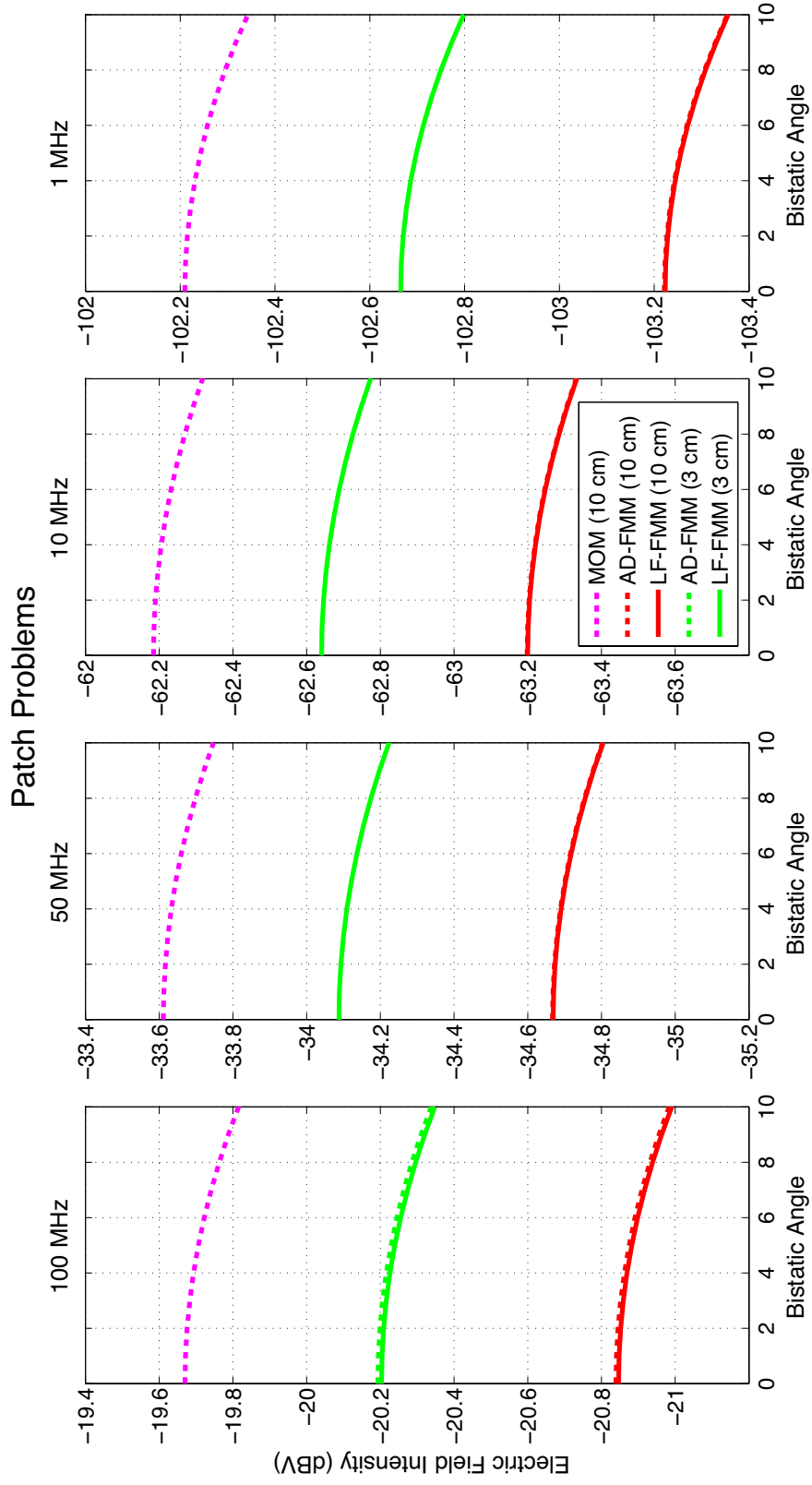
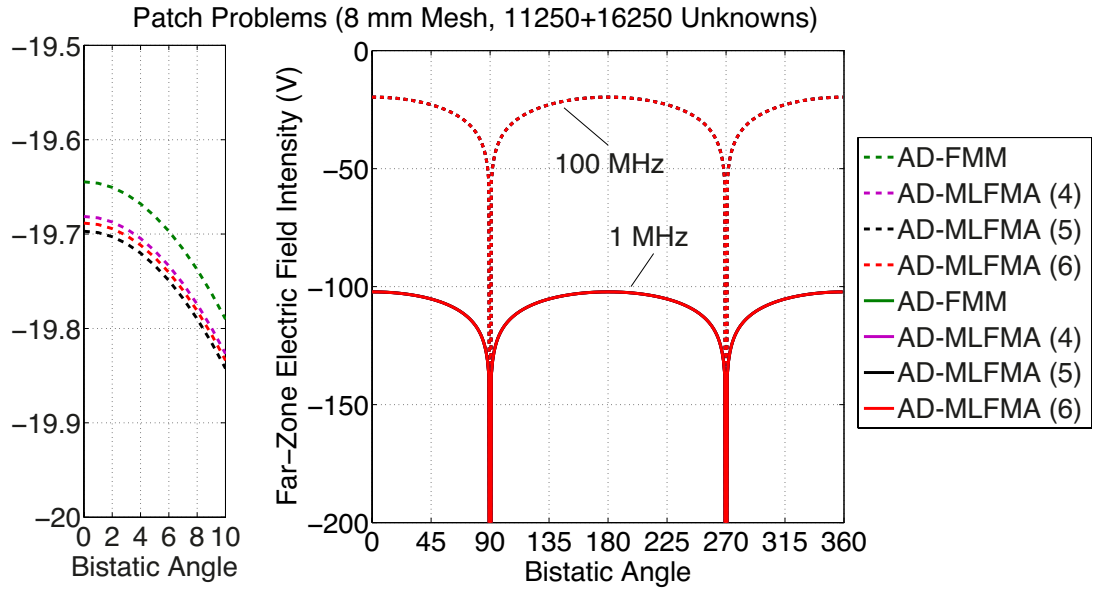Figure 4.12: Zoomed versions of the plots in Figure 4.11.

Figure 4.13: Far-zone electric field intensity scattered from a PEC patch with 0.6 m edges at 1 MHz and 100 MHz. The solutions are performed with AD-MLFMA using different numbers of levels.
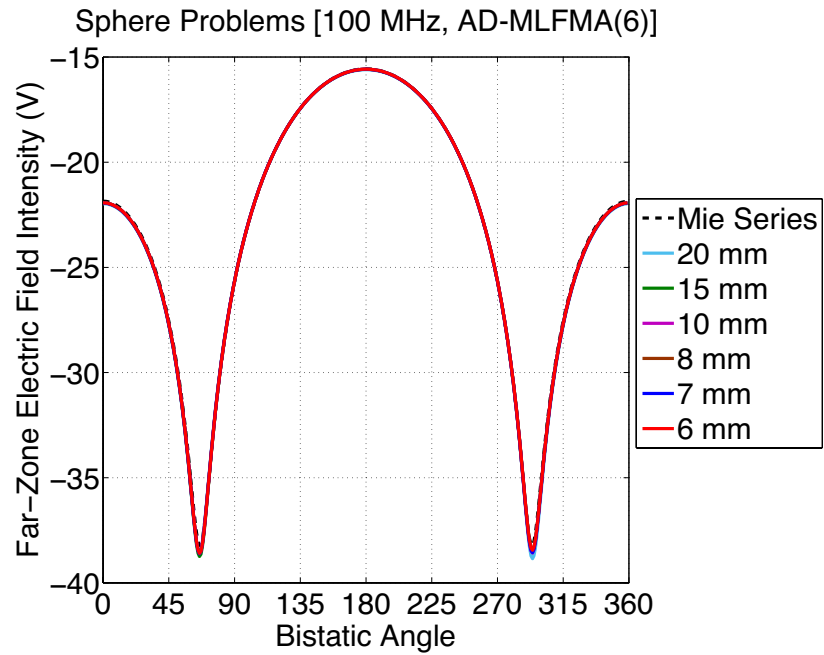

Figure 4.14: Far-zone electric field intensity scattered from a sphere of radius 0.3 m at 100 MHz. The solutions are performed with six-level AD-MLFMA for different mesh sizes, in comparison to Mie series.
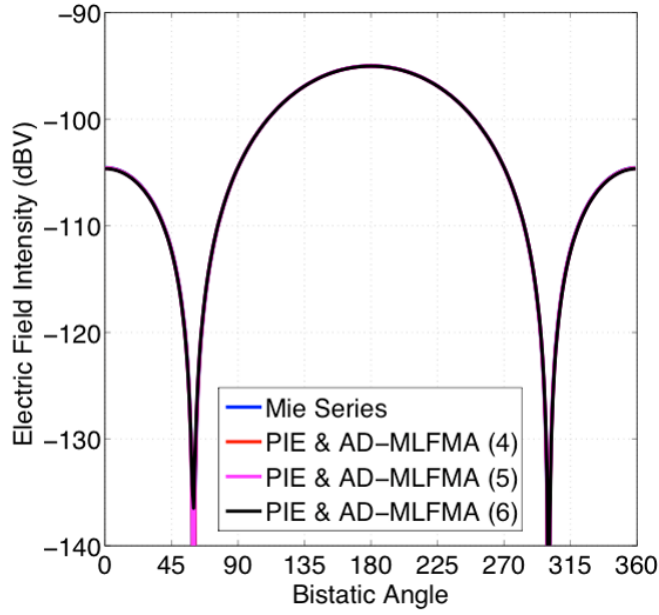
71

Figure 4.15: Far-zone electric field intensity scattered from a PEC sphere of radius 0.3 m involving 25,058 triangle patches and 37,587 RWG functions at 1 MHz. The solutions are performed with AD-MLFMA using different numbers of levels, and via Mie series [31].
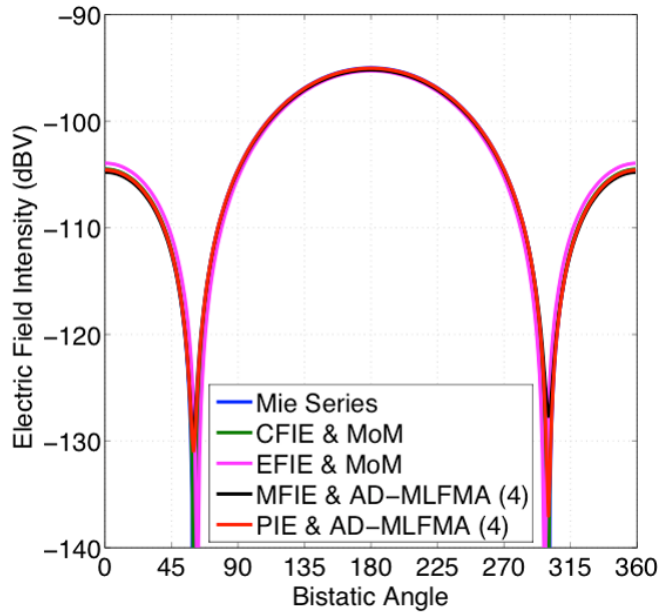

Figure 4.16: Far-zone electric field intensity scattered from a PEC sphere of radius 0.3 m involving 25,058 triangle patches and 37,587 RWG functions at 1 MHz. The solutions are performed with MoM and four-level AD-MLFMA using different formulations, and by using Mie series [31].
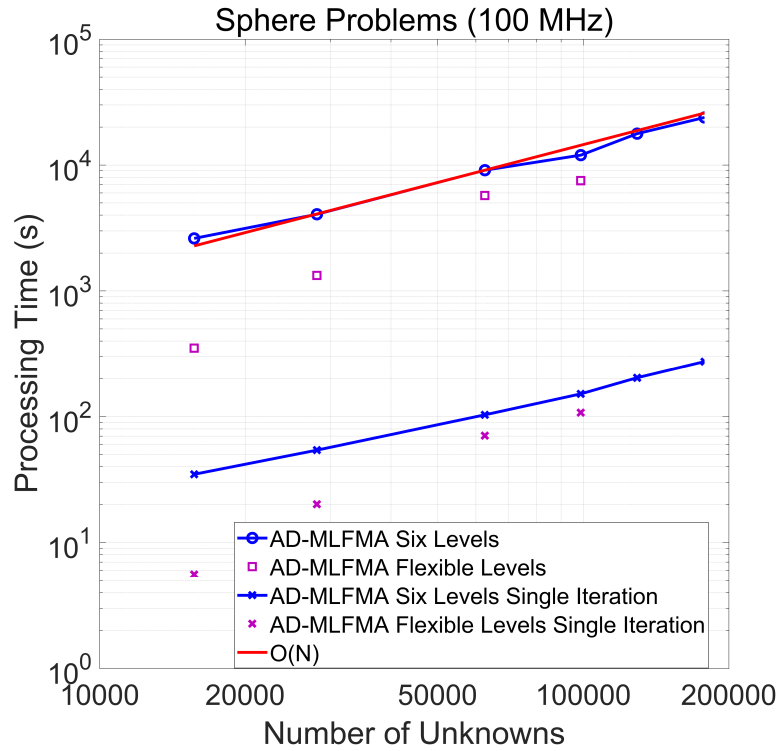
Figure 4.17: Solution times for a scattering problem involving a sphere of radius 0.3m at 100 MHz. AD-MLFMA implementations with a fixed number of levels and with changing numbers of levels are used with different discretizations.
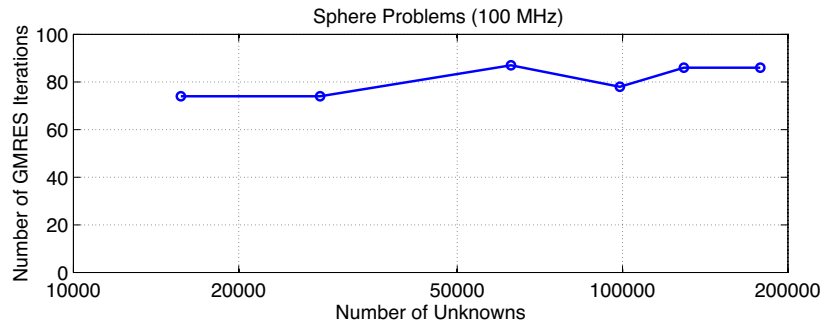

Figure 4.18: Number of iterations required for the solutions shown in Figure 4.17. Six-level AD-MLFMA is used with different discretizations.

CHAPTER 5

CONCLUSIONS

In this thesis, novel PIEs for accurate and stable solutions of low-frequency problems involving arbitrary shaped objects are studied. Low-frequency breakdown is investigated for both conventional integral equations and PIEs. As a major contribution, PIEs are solved by using low-frequency implementations of MLFMA for dense discretizations with respect to wavelength.

Starting from Maxwell's equations, both field integral equations and PIEs are derived. While field integral equations use potentials as auxiliary components to reach the field quantities, PIEs directly use magnetic vector and electric scalar potentials. Derived equations are discretized and solved with MoM. Comparisons with analytical solutions show that EFIE has accuracy issues for low-frequency problems when far-zone scattered electric fields are investigated, while PIEs provide accurate results.

Low-frequency breakdown is explained with two main mechanisms. First, field imbalance is described as an imbalance in the terms of the integral equation. This kind of an imbalance can be seen in EFIE. When the frequency drops down, that imbalance causes a term to disappear from the equation. We show that, even though the overall current density seems inaccurate, it also carries some accurate information such as irrotational current density. Therefore, 'broken' EFIE may give accurate electric charge and near-zone electric field results. Second, as the solenoidal current naturally dominates over the irrotational current at low frequencies, the irrotational part may disappear due to finite precision, which we define as source imbalance. This kind of an imbalance is the major problem in PIEs at low frequencies. In the context of PIEs, this issue can be solved with an additional integral equation. By solving the equation

as a post processing, accurate electric charge densities and near-zone electric fields can be obtained.

Ordinary MLFMA cannot be used for low-frequency problems as it is based on the diagonalization with plane waves that is not valid for short distances. Therefore, low-frequency compatible versions of MLFMA are implemented for stable solutions of PIEs. First, recently introduced AD-MLFMA based on approximate diagonalization of the Green's function is implemented. In this method aggregation and disaggregations are approximated as scaled complex exponentials. Although AD-MLFMA has limited accuracy, the method provides stability at arbitrarily low frequencies. Second, multipole-based MLFMA (LF-MLFMA) which does not use diagonalization is applied. This method provides controllable accuracy and high stability; but it involves dense matrix multiplications for aggregation, translation, and disaggregation phases, leading to less efficient solutions. Accuracy, stability, and efficiency of the two implementations (AD-MLFMA and LF-MLFMA) are shown on canonical problems.

This thesis is a starting point towards stable and accurate solutions of low-frequency problems involving large numbers of unknowns. Future works may include hybrid integral equations involving PIEs and mixed-form MLFMA to obtain efficient solutions of multiscale problems, such as complex circuits on large platforms, in broadband applications.

REFERENCES

[1] W. C. Chew, E. Michielssen, J. Song, and J.-M. Jin, *Fast and efficient algorithms in computational electromagnetics*. Artech House Inc., 2001.

[2] R. F. Harrington, *Field computation by moment methods*. Oxford University Press, 1993.

[3] R. Coifman, V. Rokhlin, and S. Wandzura, "The fast multipole method for the wave equation: A pedestrian prescription," *IEEE Antennas and Propagation Magazine*, vol. 35, no. 3, pp. 7–12, 1993.

[4] J. Song, C.-C. Lu, and W. C. Chew, "Multilevel fast multipole algorithm for electromagnetic scattering by large complex objects," *IEEE Transactions on Antennas and Propagation*, vol. 45, no. 10, pp. 1488–1493, 1997.

[5] W. C. Chew, M. S. Tong, and B. Hu, "Integral equation methods for electromagnetic and elastic waves," *Synthesis Lectures on Computational Electromagnetics*, vol. 3, no. 1, 2008.

[6] J. R. Mautz and R. F. Harrington, "H-field, E-field, and combined field solutions for bodies of revolution," AEÜ, vol. 32, no. 4, 1978.

[7] S. Rao, D. R. Wilton, and A. Glisson, "Electromagnetic scattering by surfaces of arbitrary shape," *IEEE Transactions on Antennas and Propagation*, vol. 30, no. 3, pp. 409–418, 1982.

[8] Ö. Ergül and L. Gürel, *The multilevel fast multipole algorithm (MLFMA) for solving large-scale computational electromagnetics problems*. John Wiley & Sons, 2014.

[9] D. Dunavant, "High degree efficient symmetrical gaussian quadrature rules for the triangle," *International Journal for Numerical Methods in Engineering*, vol. 21, no. 6, pp. 1129–1148, 1985.

[10] W. C. Chew, *Waves and fields in inhomogeneous media*, New York: IEEE Press, 1995.

[11] Y. Saad and M. H. Schultz, "Gmres: A generalized minimal residual algorithm for solving nonsymmetric linear systems," *SIAM Journal on Scientific and Statistical Computing*, vol. 7, no. 3, pp. 856–869, 1986.

[12] W. C. Chew, "Vector potential electromagnetics with generalized gauge for inhomogeneous media: formulation," *Progress In Electromagnetics Research*, vol. 149, pp. 69–84, 2014.

[13] F. Vico, M. Ferrando, L. Greengard, and Z. Gimbutas, "The decoupled potential integral equation for time-harmonic electromagnetic scattering," *Communications on Pure and Applied Mathematics*, vol. 69, no. 4, pp. 771–812, 2016.

[14] Y. Aharonov and D. Bohm, "Significance of electromagnetic potentials in the quantum theory," *Physical Review*, vol. 115, no. 3, p. 485, 1959.

[15] Z. G. Qian and W. C. Chew, "Fast Full-Wave Surface Integral Equation Solver for Multiscale Structure Modeling," *IEEE Transactions on Antennas and Propagation*, vol. 57, no. 11, pp. 3594-3601, Nov. 2009.

[16] G. Mie, "Contributions to the optics of turbid media, particularly of colloidal metal solutions," Transl. into English from Ann. Phys.(Leipzig), vol. 25, no. 3, 1908, pp. 377-445, 1976.

[17] F. Mutlu, C. Önol, B. Karaosmanoğlu, and Ö. Ergül, "Inkjet-printed cage-dipole antennas for radio-frequency applications," *IET Microwaves, Antennas & Propagation*, pp. 2016–2020, 2017.

[18] Z. G. Qian and W. C. Chew, "A quantitative study on the low frequency breakdown of EFIE," *Microwave and Optical Technology Letters*, vol. 50, no. 5, pp. 1159–1162, 2008.

[19] F. P. Andriulli, K. Cools, H. Bağcı, F. Olyslager, A. Buffa, S. Christiansen, and E. Michielssen, "A multiplicative Calderon preconditioner for the electric field integral equation," *IEEE Transactions on Antennas and Propagation*, vol. 56, no. 8, pp. 2398–2412, 2008.

[20] G. Vecchi, "Loop-star decomposition of basis functions in the discretization of the EFIE," *IEEE Transactions on Antennas and Propagation*, vol. 47, no. 2, pp. 339–346, 1999.

[21] M. Taskinen and P. Yla-Oijala, "Current and charge integral equation formulation," *IEEE Transactions on Antennas and Propagation*, vol. 54, no. 1, pp. 58–67, 2006.

[22] Z. G. Qian and W. C. Chew, "An augmented electric field integral equation for high-speed interconnect analysis," *Microwave and Optical Technology Letters*, vol. 50, no. 10, pp. 2658–2662, 2008.

[23] U. M. Gür and Ö. Ergül, "Accuracy of sources and near-zone fields when using potential integral equations at low frequencies," *IEEE Antennas and Wireless Propagation Letters*, vol. 16, pp. 2783–2786, 2017.

[24] Q. S. Liu, S. Sun, and W. C. Chew, "An integral equation method based on vector and scalar potential formulations," in Proc. *IEEE International Symposium on Antennas and Propagation & USNC/URSI National Radio Science Meeting*, pp. 744–745, 2015.

[25] J.-S. Zhao and W. C. Chew, "Three-dimensional multilevel fast multipole algorithm from static to electrodynamic," *Microwave and Optical Technology Letters*, vol. 26, no. 1, pp. 43–48, 2000.

[26] Ö. Ergül and B. Karaosmanoğlu, "Approximate stable diagonalization of the green's function for low frequencies," *IEEE Antennas and Wireless Propagation Letters*, vol. 13, pp. 1054–1056, 2014.

[27] Ö. Ergül and B. Karaosmanoğlu, "Broadband multilevel fast multipole algorithm based on an approximate diagonalization of the green's function," *IEEE Transactions on Antennas and Propagation*, vol. 63, no. 7, pp. 3035–3041, 2015.

[28] L. Jiang and W. C. Chew, "Low-frequency fast inhomogeneous plane-wave algorithm (LF-FIPWA)," *Microwave and Optical Technology Letters*, vol. 40, no. 2, pp. 117–122, 2004.

[29] I. Bogaert, J. Peeters, and F. Olyslager, "A nondirective plane wave mlfma stable at low frequencies," *IEEE Transactions on Antennas and Propagation*, vol. 56, no. 12, pp. 3752–3767, 2008.

[30] Ö. Ergül and B. Karaosmanoğlu, "Low-frequency fast multipole method based on multiple-precision arithmetic," *IEEE Antennas and Wireless Propagation Letters*, vol. 13, pp. 975–978, 2014.

[31] U. M. Gür, B. Karaosmanoğlu, and Ö. Ergül, "Solutions of new potential integral equations using approximate stable diagonalization of the green's function," in Proc. *International Conference on Electromagnetics in Advanced Applications (ICEAA)*, pp. 1894–1897, 2017.

[32] U. M. Gür, B. Karaosmanoğlu, and Ö. Ergül, "Fast-multipole-method solutions of new potential integral equations," in Proc. *IV International Electromagnetic Compatibility Conference (EMC Turkiye)*, pp. 1–6, 2017.